Imperial College London
Department of Bioengineering

Network analysis of the cellular circuits of memory

Giuseppe Pietro Gava

Advisors: Prof. Simon R. Schultz and Prof. David Dupret

Submitted in part fulfilment of the requirements for the degree of
Doctor of Philosophy in Neurotechnology at Imperial College London

Copyright Declaration

Declaration of Originality

I hereby declare that the work presented in this thesis is my own, except otherwise acknowledged. Some parts have been conducted in collaboration with other researchers, and this is indicated where relevant.

Abstract

Intuitively, memory is conceived as a collection of static images that we accumulate as we experience the world. But actually, memories are constantly changing through our life, shaped by our ongoing experiences. Assimilating new knowledge without corrupting pre-existing memories is then a critical brain function. However, learning and memory interact: prior knowledge can proactively influence learning, and new information can retroactively modify memories of past events. The hippocampus is a brain region essential for learning and memory, but the network-level operations that underlie the continuous integration of new experiences into memory, segregating them as discrete traces while enabling their interaction, are unknown. Here I show a network mechanism by which two distinct memories interact. Hippocampal CA1 neuron ensembles were monitored in mice as they explored a familiar environment before and after forming a new place-reward memory in a different environment. By employing a network science representation of the co-firing relationships among principal cells, I first found that new associative learning modifies the topology of the cells' co-firing patterns representing the unrelated familiar environment. I further observed that these neuronal co-firing graphs evolved along three functional axes: the first segregated novelty; the second distinguished individual novel behavioural experiences; while the third revealed cross-memory interaction. Finally, I found that during this process, high activity principal cells rapidly formed the core representation of each memory; whereas low activity principal cells gradually joined co-activation motifs throughout individual experiences, enabling cross-memory interactions. These findings reveal an organizational principle of brain networks where high and low activity cells are differentially recruited into coactivity motifs as building blocks for the flexible integration and interaction of memories.

Finally, I employ a set of manifold learning and related approaches to explore and characterise the complex neural population dynamics within CA1 that underlie simple exploration.

Acknowledgements

Firstly, I would like to thank both my supervisors Prof Simon Schultz and Prof David Dupret. During the PhD, Simon guided me through information theoretical and other neural analytical methods that have been essential to my formation shaped my research perspective. I would like to thank David for welcoming me to his lab and providing all the support I needed to become a synergistic member of the Dupret lab and do fascinating science together.

In addition, both the Schultz lab, at Imperial College London, and the Dupret lab, at the Medical Research Council Brain Network Dynamics Unit, have been great working environments, providing many interesting discussions, but I have also found warm and fun communities to spend time with. I would then like to thank all of the members of both labs, present and past, with a particular mention to Dr Vitor Lopes Dos Santos and Dr Mohamady El-Gaby for several suggestions regarding data analysis protocols and stimulating discussions. Also thanks to Ben Micklem at the MRC BDNU for his technical help with both IT and designing issues.

My PhD studies have been funded by the Engineering Physical Research Council through the Centre for Doctoral Training in Neurotechnology at Imperial College London. I would like to particularly thank Dr Kate Hobson for all the support and her amazing work at managing the Neurotechnology CDT, but also all my cohort of colleagues for the inspiring discussion and the leisure time spent together.

On a personal level, I express profound gratitude to my parents for providing me with every possible opportunity and supporting me throughout my education. Finally, I thank my friends and family, especially Martyna, for having supported me through this journey.

‘Se vogliamo che tutto rimanga com’è, bisogna che tutto cambi.’
‘For everything to stay the same, everything has to change.’

Giuseppe Tomasi de Lampedusa

Contents

List of Figures

List of Abbreviations

CA Cornu Ammonis

dCA1 Dorsal CA1 region of the hippocampus

LTP Long Term Potentiation

LTD Long Term Depression

LFP Local Field Potential

SWR Sharp-wave Ripple

MI Mutual information

EEG Electroencephalography

MEG Magnetoencephalography

fMRI functional Magnetic Resonance Imaging

GLM Generalised Linear Model

PCA Principal Component Analysis

ICA Independent Component Analysis

MDS Multi Dimensional Scaling

UMAP Uniform Manifold Approximation and Projection

CPP Conditioned Place Preference

SPP Spontaneous Place Preference

Chapter 1

Introduction

1.1 Network analysis of the cellular circuits of memory

Memory is instinctively conceived as a collection of static photographs that we accumulate as we experience the world, storing them somewhere in our brains. On the other hand, memories are constantly changing through our life, shaped by our ongoing experiences and interactions with the world. The function of a memory system, that is assimilating new knowledge without corrupting pre-existing memories of successful behaviour, is a critical brain function to guide behaviour and secure survival in a dynamically changing environment. However, learning and memory interact: prior knowledge can proactively influence ongoing learning, and new information can retroactively modify memories of past events. (Richards and Frankland, 2017; Mau, Hasselmo, et al., 2020).

A region of the brain essential for learning and memory is the hippocampus, home to the cellular circuitry that gives rise to these functions. Its fundamental role became

clear since the 1950s with the studies on retrograde amnesia in humans and further evidence came from the discovery of place cells in rodents, which paved the way to the conception of the hippocampus as a fundamental hub in the brain for the formation and manipulation of memories and their associations. (Eichenbaum et al., 1999; Bunsey and Eichenbaum, 1996; Tse et al., 2007). The theory of cell assemblies was particularly successful in framing the hippocampal representation of mnemonic engrams, showing that the precise timing of neuronal spiking activity is critical to information processing within the hippocampal network (Kubie et al., 2020; O'Neill et al., 2008; Trouche, Perestenko, et al., 2016; Ven et al., 2016). However, the circuit-level operations that underlie the continuous integration of new experiences into memory, segregating them as discrete traces while enabling their interaction, are unknown.

While the physiology of single neurons is important to understand the functions of a circuit, the population-level interactions are key to fully uncover the mechanisms that underlie its multiplex processes. Nowadays the increasing size and scope of the neural ensembles captured by modern acquisition technologies, together with the refined behavioural paradigms of the associated experiments, demand analytical techniques that can cope with the complexity generated by the recorded neural activity. Here we use tools from graph-theory and topology to study the complex system formed by the dCA1 hippocampal circuitry, investigating the dynamic integration of new information into flexible pre-existing mnemonical structures.

1.2 Overview

In this thesis I aim to investigate the neuronal network mechanisms underpinning the integration of new information within a pre-existing mnemonic framework.

In the first part of the thesis, **chapter 2**, I review literature framing the mnemonic system as an internal dynamic model of the world to predict future events, instead of a collection of static pieces of information. I highlight the role of the hippocampus in the formation of the context within which episodic memories are formed and later recalled. In doing so I focus on methods to quantify the spatial tuning of hippocampal neurons using information theory. I conclude the chapter by highlighting the skewed distributions of the brain's structural and dynamical features, addressing the consequent effects on the neural activity and it's computations. This leads to a characterisation of the heterogeneous population of principal cells in hippocampal CA1 region, which is thought to be key to the diverse operations carried out by this circuit.

In **chapter 3** I consider the application of graph-theoretical and topological methods to the study of complex systems, such as brain networks. I set up a framework to evaluate the co-firing topology of a neuronal network that will enable us to capture the temporal fine grained co-activity relationships between neurons in different contexts. Such analysis will yield insights into the mechanisms underpinning dynamic neural representations. Moreover, the co-firing topology of the dCA1 pyramidal cells circuit is evaluated, finding a weak small-world structure.

In **chapter 4** I show a network mechanism by which two distinct memories interact, leveraging on the framework developed in chapter 3. I analyse hippocampal CA1 neuron ensembles in mice exploring a familiar environment before and after forming a new place-reward memory in a different environment during a conditioned place preference (CPP) task. By analysing the activity of principal cells with graph-theoretical techniques, I first find that new associative learning modifies the topology of the cells' co-firing patterns that represents the unrelated familiar environment,

suggesting the presence of hysterical dynamics in the network. Moreover, I observe that the co-firing networks evolved along three functional axes supported by the heterogeneous contributions of high and low activity principal cells. The first axis separated the two spatial environments (the "where") and was mostly explained by the contribution of high activity cells, the second axis distinguished individual behavioural sessions (the "what") while low activity cells spanned the third axis by gradually joining coactivation motifs throughout individual experience, revealing cross-memory interaction. These findings reveal an organizational principle of brain networks where high and low activity cells are differently recruited into coactivity motifs as building blocks for flexible integration and interaction of memories.

In **chapter 5** I use manifold learning and related approaches to explore mice hippocampal CA1 population dynamics evoked by exploration of a 1D circular linear track and 2D open field environments. I describe the representational space of the neural population by using the manifold learning approach to uncover low dimensional structure in the high dimensional neuronal activity. I argue this population dynamics analysis is complementary to the graph-theoretical one described in chapter 3: instead of describing network interaction motifs at the single-cell level resolution, manifold learning extracts "higher level" neural representations driven by the population dynamics, which are more closely related to the animal's behaviour. Within CA1 I show that 2D exploration evokes a more complex response than 1D one, displaying how the neural population dynamics are closely knit to behaviour.

Finally, in **chapter 6** I summarise the contributions of this thesis and discuss them in light of the existing literature, together with highlighting the potentials of population and network-level analyses towards our understanding of memory and related functions supported by the neuronal circuitry.

Chapter 2

The hippocampus sets the context

2.1 Dynamic memories

Memories are patterns of neural activity that guide present behaviour in familiar situations by preserving useful information from past experiences. Such a simple theoretical definition, though, becomes a complex concept in practice: the surrounding environment is dynamic and probabilistic, requiring the brain to shape its mnemonic representations according to the context at hand. In fact, dynamic, ever-changing environments imply that whatever is learned from an individual episode may not hold true in similar future experiences and should therefore be updated over time. Failing to do so, would make memory systems unable to generalize to future retrieval episodes where conditions might have changed, leading to suboptimal behaviors (Richards and Frankland, 2017).

2.1.1 Memory is shaped by persistence and transience

However, it is still fairly common, also across scientists, to believe that the optimal memory system would be one of perfect persistence. This is a system where information is stored with the highest possible accuracy, for the longest period of time. Is it possible, then, to have a system capable of storing information with perfect accuracy and to use it optimally to drive behaviour?

In the short story "Funes the Memorious" (first published in 1944), the Argentinean writer Jorge Luis Borges insightfully explored the consequences of a flawless, all-encompassing memory. The fictional story is an unknown storyteller's recollection of Ireneo Funes, a young man who, after sustaining a head injury due to a horse incident, was able to remember and perceive everything down to its finest details: "Funes remembered not only every leaf of every tree of every wood, but also every one of the times he had perceived or imagined it." Although Funes himself considered his extraordinary memory a blessing at first, the storyteller recognized serious drawbacks soon after meeting him. He noticed that Funes was unable to form even the simplest generalization. He described how "it was not only difficult for him to understand that the generic term *dog* embraced so many unlike specimens of different sizes and different forms; he was disturbed by the fact that the dog at three fourteen (seen from the side) should have the same name as the dog at three fifteen (seen from the front)." Towards the end of the story, Borges, through the mouth of his storyteller, goes insofar as to infer that Funes "was not very capable of thought", and to finally conclude that "to think is to forget differences, to generalize, to make abstractions".

What Borges so skilfully depicted in his short story and the conclusion reached by his storyteller resembles the thesis, written several decades earlier, by the philosopher William James. In his book "The Principles of Psychology" he states that "in the

practical use of our intellect, forgetting is as important a function as recollecting" (James, 1890; p.679). What James meant here, is that for our memory to be useful, we need to be selective in what we remember. He argued that if too many memories were stored in our brain, the recall of each individual memory would be so time-consuming that no time would be left for thinking.

The aforementioned thesis acquired scientific confirmation from the few examples of individuals with something approximating a memory system of perfect persistence, suggesting that remembering everything comes at a dire cost. More than 60 years ago, the Soviet clinical neuropsychologist A. R. Luria described the case of Patient S., a man with "vast memory" who could only forget something if he actively willed himself to do so (Luria, 1968). Nonetheless, according to Luria's accounts, Patient S. was hindered by his apparent super-human memory. While he was able to remember instances in exquisite detail, his memory was inflexible and he was unable to generalize across instances. This highlights, as James suggested, the importance of forgetting (transience) as a critical component of a healthy mnemonic system.

So a memory system aims not to remember individual events with the highest fidelity, instead it aims to update and refine its internal model of the world in response to external stimuli a critical tool for survival in a dynamic environment (Mau, Hasselmo, et al., 2020). A well-known approach to build a solid and versatile model is to avoid overfitting, which potentially leads to biased future predictions. In memory terms, this relates to the ability to generalise over multiple events, which can be compromised when a model is "trained" too extensively on the particular features of an individual dataset (Hawkins, 2004). The solution to overfitting usually resides in a careful model selection process, which often leads to the simplest model that can explain the events reasonably well, following Occam's razor heuristics: the simpler the explanation, the broader its application.

When memory is framed as a model, the events details that get forgotten are nec-

essary to keep the model simple rather than being caused by some imperfections in the processes underlying mnemonic persistence, as commonly thought (D. Schacter, 2001). Simple memories that store the gist of our experiences and avoid complicated details will be better for generalizing to future events (Kumaran et al., 2016; Richards, Xia, et al., 2014). One way to construct simple memories is to engage in some controlled, partial forgetting. Specifically, in order to store only the essence of an experience, statistically insignificant details must be forgotten (Sekeres et al., 2016). Partial forgetting could then be interpreted as a form of regularization of the model, which can also be viewed as a form of Bayesian learning (Mackay, 2003). Within neuronal networks, the outcome of minimizing overfitting is generalization, as previously stated. Consistent with this, a recent study showed that preventing forgetting impairs the development of generalization in a contextual fear conditioning task in rats, highlighting the importance of transience in memory systems (Migues et al., 2016).

2.1.2 Models of memory consolidation

The combination of persistence and transience lead to memory-updating routines within the brain, which can be defined as the modification of existing firing patterns within the brain to integrate new information into pre-existing memories (Mau, Hasselmo, et al., 2020). Memories are known to be liable immediately after learning, that is are subject to modification and interference. Memory consolidation refers to the process leading to the integration of a newly acquired mnemonic within the large network of pre-existing knowledge (Ribot, 1882; Glickman, 1961). A similar process, called reconsolidation, takes place every time a mnemonic trace is recalled, exposing it to potential modification and update, a process that continues indefinitely over an animal lifetime (Dudai, 2004; Nadel et al., 2012; Dudai, 2012). These two processes share similar neuronal mechanism leading to the proposal that reconsolidation is

just lingering consolidation, framing the problem as a *system consolidation* one – i.e, the reorganisations of memories among different regions of the brain (Nader et al., 2000; McKenzie and Eichenbaum, 2011; Dudai, 2012).

The consolidation hypothesis emerged from studies performed on patients with medial temporal lobe lesions who suffered from temporally graded retrograde amnesia and were unable to form new declarative (i.e, explicit, non-motor or implicit) memories (Scoville and Milner, 1957; Milner et al., 1998). Patient H. M. is perhaps the most remarkable case: he suffered a bilateral medial temporal lobe removal as an experimental procedure to treat epileptic seizures. He was unable to form new memories after the intervention and suffered from a partial retrograde amnesia, even though he developed "no impairment of personality or general intelligence" (Scoville and Milner, 1957; p.17).

The medial temporal lobe refers a large part of the brain that includes the hippocampal formation (containing the dentate gyrus and the hippocampus proper consisting of the Cornu Ammonis [CA] regions and the subiculum), the entorhinal, perirhinal and parahippocampal cortices and the amygdaloid complex (Squire and Zola-Morgan, 1991). A number of studies, including on animal models such as monkeys and rats, have since proven that the hippocampal formation is critical for the formation of new memories and have brought evidence for its decreasing involvement over time (Squire, Clark, et al., 2001). This hypothesis is regarded as the *standard consolidation model* (Squire and Alvarez, 1995, McClelland et al., 1995; with important roots in the theory of Marr 1970, 1971). This model posits that the hippocampus is only a temporary repository for memory and that the neocortex stores the memory thereafter. Importantly, it is hypothesised that memory retrieval critically depends on an intact hippocampus at first, but that over time this dependence diminishes so that memories can be recalled by the cortex on its own.

However, over time, some evidence that seems incompatible with the standard consolidation theory has accumulated. While medial temporal lobe damage results in temporally graded retrograde amnesia for semantic memories (i.e., facts, general knowledge), this seems not be the case for episodic memories (i.e., personal experiences, autobiographical events). Even though H. M. and similar patients can recall details of remote memories, they lack the ability to narrate and place themselves in spatio-temporal contexts (Squire, 2004). Therefore, stemming on observations from both lesion (Fujii et al., 2000) and imaging studies (e.g., Gilboa et al., 2004, 2006), it has been suggested that the hippocampus always remains involved in the retrieval of episodic memories (Moscovitch et al., 2006). This hypothesis has been called the *multiple trace model*, as it proposes that each time an episodic memory is recalled it is re-encoded, which leads to the formation of multiple overlapping but dissimilar memory traces for the same experience. This proposes to explain why remote memories are more widely distributed in the brain and why the cortex alone can recall semantic aspects of such memories. To truly re-experience past events, however, the hippocampus is believed to always be required in order to bind together in the right sequence all details of an episodic memory. Recently, an extension to this theory has been the trace-transformation hypothesis, which highlights that there is a qualitative difference between the self-centred, episodic memories depending on the hippocampus and the more abstract, gist-like, semantic memories supported by cortical areas (Winocur and Moscovitch, 2011). An alternative hypothesis is that memory traces themselves no longer reside in the hippocampus, but that hippocampal circuits help to sequentially coordinate the recall of mnemonic traces stored in the neocortex, therefore providing an egocentric perspective for the episodes (Buzsáki, 2019).

All these hypothesis, though, consider systems consolidation as a gradual, lengthy process. The *schema assimilation model* (Tse et al., 2007) posits that systems consolidation could be accomplished quickly if a previously established body of related knowledge, i.e., a memory schema (Barlett, 1932), is available into which the new

knowledge may be assimilated. In this way, it is proposed, the hippocampus systematically organizes multiple overlapping memories to form relational networks, which serve as a mnemonic backbone that can foster rapid learning (McKenzie, A. J. Frank, et al., 2014). This theory is very much in accord with the hypothesis framing memory as an internal model of the world that can create hierachicaly generalise across memories to improve its predictions and facilitate learning.

The two latter presented hypothesis, the multiple trace model (with its variations) and the schema assimilation model, result in a highly dynamic depiction of the memory trace, appreciating its restlessness and incessant assimilation into knowledge for an internal model of the world (Dudai and Morris, 2013).

2.2 The cellular circuitry underpinning memory

In this thesis, I will focus on the dynamic neuronal network representation of memories within the dCA1 region of the hippocampus. It is important though that I stress the fundamental circuitry and physiological constraints, together with the network functional ones, that shape the output of the hippocampal dCA1 region.

2.2.1 The hippocampal circuit

Architecture

As mentioned earlier, the hippocampus includes the dentate gyrus, the *Cornu Ammonis* (CA) and subiculum. The CA can be subdivided in three regions, CA1-3 (with CA3 at the dentate gyrus end and CA1 at subibulum's). The hippocampus is three-layered, a deep layer, comprised mostly by afferent fibres and interneurons, a (stratum oriens in the CA region), a cell layer (stratum pyramidale) above and a molecular layer (stratum moleculare) most superficially. In the CA region, though,

the stratum moleculare is composited of further sublayers. In the CA1 region these are the stratum radiatum, comprising the apical dendrites of the neurons located in the stratum pyramidale; and, most superficially, the stratum lacunosum-moleculare, comprising the apical tufts of the apical dendrites (Strien et al., 2009). Moreover, the dorsal and ventral regions of the hippocampus are also known to underpin very different functions. The dorsal hippocampus performs primarily cognitive functions, the ventral region, instead, primates) relates to stress, emotion and affect. They have different anatomical connections and gene expression, which correlates with cortical areas in the dorsal hippocampus and with region connected to emotions and stress (amygdala and hypothalamus) in the ventral region (Fanselow and Dong, 2010; Tao et al., 2021).

The CA1 region, along with subiculum, is considered the output of the hippocampus to the neocortex. The two main inputs to the dorsal CA1 region (dCA1) are directly from layer III of entorhinal cortex and via the perforant path that originate from the dentate gyrus and then through the CA3 region. Both theoretical models and experimental evidence suggest local competitive inhibition allows the dentate gyrus to decorrelate the cortical inputs (Treves and Rolls, 1994; J. K. Leutgeb et al., 2007). The highly recurrent connectivity of the CA3 region is thought to underlie its pattern completion capacity (Hasselmo et al., 1995). The CA1 may integrate the output of the CA3 with direct input from layer III of entorhinal cortex and provide a sparse representation for readout by downstream regions (Barnes et al., 1990).

Cellular diversity

In the hippocampus, like everywhere else in the cortex, there are excitatory, glutamatergic neurons (principal cells) and inhibitory, GABAergic interneurons. CA1 principal cells carry the primary output of the hippocampus to other brain regions, displaying spatio-contextual tuning (see section 2.3.4) but at least 16 types of differ-

ent types of interneurons support their activity (Somogyi and Klausberger, 2005). The connectivity between the excitatory and inhibitory neurons (feedback inhibition, including lateral inhibition) is believed to gate afferent inputs (Fernández-Ruiz et al., 2017; Milstein et al., 2015), control local synchrony (Stark, Roux, Eichler, Senzai, et al., 2014), and give rise to competitive interactions within the excitatory population (Buzsáki, 2010; Trouche, Perestenko, et al., 2016). CA1 principal cells arenot an homogeneous population either, and differences are known to exist along the dorsoventral and radial axes (see section 2.4.4).

2.2.2 Distinct oscillations underlie distinct network states within the hippocampal network

The brain activity is characterised by periodic, recurrent events that shape its functions and responses both to internal and external phenomena. First evidence of these oscillatory patterns first came from Hans Berger in 1929, but they were only formally classified in 1974, The brain rhythms were divided into bands: delta, 0.5–4 Hz; theta, 4–8 Hz; alpha, 8–12 Hz; beta, 12–30 Hz; gamma, >30 Hz. The borders of these classes were drawn arbitrarily as the function of each oscillation was largely unknown. The frequency of the oscillation within the brain actually span more than 4 orders of magnitude and Penttonen and Buzsáki, 2003 found that these bands form a geometric progression on a linear frequency scale. The power law relation has roughly constant base of $e = 2.718$ – Euler's number and base of the natural logarithm. Since e is an irrational number, the various oscillations are never able to entrain each other, perpetually fluctuating between transiently stable states. These constantly interfering network rhythms, then, give rise to a quasi-periodic or weakly chaotic pattern, characteristic of the EEG landscape (Buzsáki, 2009).

The activity within the hippocampus is mainly characterised by three brain rhythms:

theta, gamma and sharp-wave ripples (SWR); which define two distinct network states. The first one is present in the awake mouse, and during rapid eye movement sleep (REM); rhythms at theta (4-10 HZ) and gamma (30-80 Hz) are observed, with the former being largely predominant. Theta oscillations, in the awake exploring animal, are thought to support the structure of principal cells activity, by providing discrete windows where information can be processed by the network (driven by different gamma and slower oscillations; Lopes-dos-Santos et al., 2018). These oscillations play a crucial role in the temporal firing sequence (e.g. place cell activity, see section 2.3.4) and in the modification of synaptic weights (O'Keefe and Recce, 1993; Buzsáki, Adey, et al., 2002; E. I. Moser, Kropff, et al., 2008). During this state, highly processed sensory information from the entorhinal cortex drives activity throughout the hippocampal circuit (Brun et al., 2008).

The second hippocampal network state arises during consummatory behaviours - i.e. eating and drinking -, resting and non REM sleep (these two sets of behaviour are believed to evoke two separate states, see Kay and L. M. Frank, 2018), and is characterised by a pattern of slow irregular waves which is interrupted by a large, highly synchronised burst of oscillations. They last around 50-100ms and give rise to high frequency bursts of spiking neuronal activity (140-200 Hz) that originates in the hippocampus CA3 region and propagate, through CA1, to a wide area of the cortex, making it the most synchronous known event in the mammalian brain (Buzsáki, 2015). SWRs are thought of playing a critical role in memory consolidation (see section 2.1.2) by replaying of awake exploration firing patterns during sleep (Wilson and McNaughton, 1994; O'Neill et al., 2008). It has also been shown that SWR frequency increases after learning and predicts subsequent performance (Ramadan et al., 2009). Moreover, SWR disruption impairs the performance in mnemonic tasks, affecting memory consolidation (Ven et al., 2016; Girardeau et al., 2009)

2.3 Memory representation

2.3.1 The neuron doctrine

Since the times of Camillo Golgi, Santiago Ramon y Cajal and Charles Sherrington the neuron doctrine has served as the central conceptual foundation for neuroscience, considering the individual neuron as the structural and functional unit of the nervous system. The plasticity of their connection could then underlie memory and learning (Sherrington, 1892; DeFelipe, 2006). The focus on the properties of individual neurons was a natural consequence of the use of single-cell anatomical and physiological techniques, such as the Golgi stain (Golgi, 1885) or the microelectrode (Hubel, 1957). The piecemeal reconstruction of neuronal circuits into their individual neuronal components using these methods enabled researchers to obtain important insights in to the structure and design logic of many regions of the brain, including some functional elements (e.g. the neuron's receptive field; Hubel and Wiesel, 1962).

An influential result was the discovery of "grandmother cells" at the top of the hierarchy of the mammalian visual system. These selectively tuned cells were thought responsible for the selective perception of our grandmother (Barlow, 1972). Similarly, "face cell" that responded to images of specific individuals were found in the temporal cortex of monkeys and humans (Desimone et al., 1984; Kreiman et al., 2000; Quiroga et al., 2005). These successes fostered the idea that the single neuron was not only the anatomical and functional unit of the brain but also its perceptual unit. Moreover, electrical stimulation of a very small number of cortical neurons, or even of individual neurons, can produce behavioural changes in monkeys and rodents, suggesting that the perception and even the behaviour of the animal could have individual neurons as its functional units (Brecht et al., 2004; Houweling and

Brecht, 2008).

But the neuronal doctrine might have become limiting as a scientific framework. For example, the concept of receptive field might lead to an underestimation of the true complexity of neuronal function, as unreliable, "noisy" responses recorded in the primary sensory areas of awake animals (Ko et al., 2011). In fact, It may be too narrow or simplistic to equate neuronal function with its tuning to a stimulus: firing patterns, timing and coupling with other peers in the network are most likely relevant (Fairhall, 2014; Okun et al., 2015). In fact, organized spontaneous activity appears to be prevalent in many brain regions, particularly in humans, suggesting that neurons take part in intrinsic brain functions unrelated of external stimuli (e.g., Kenet et al., 2003). Even in the case of "face cells", it is more likely that the coding process is distributed across large populations of neurons. Thus, the receptive field could be reinterpreted more generally as the single-cell manifestation of distributed and composite circuit states (Yuste, 2015). Moreover, recent studies have shown that neurons, particularly in the prefrontal and parietal cortices, display "mixed selectivity" by responding to different stimuli together by taking part to different neural ensembles (Fusi et al., 2016). If this is the case, we should focus on the activity of groups of neurons together to further our understanding of brain representations, memory included. To do so methodological innovations such as large-scale multi-unit electrophysiological and imaging recordings, together with suited analytical techniques are critical (see chapter 3).

2.3.2 Cell assemblies within neuronal networks

Thanks to its complex architecture and wiring, the brain has the structure that underpins emerging properties (i.e., properties that arise from the interactions among elements but are not present in the individual elements themselves) characteristic of many physical systems, such as the oscillatory patterns described in section 2.2.2

(P. S. Churchland and Sejnowski, 1992; Anderson, 1972). That neural circuit are built for emergent function has been known for a long time (Lorente de Nò, 1933). In 1949, Donald Hebb developed these pre-existing ideas and provided an elegant and highly influential theory about how memories are stored and represented in the brain. He proposed that neural states, including memories, are represented by the combined activity of groups of neurons, which he called "cell assemblies". He proposed that neurons repeatedly firing together in response to a particular stimulus could bind together through strengthened synaptic connections, resulting in their combined firing in response to a stimulus. For this, he postulated a learning rule by which neurons can change their synaptic weights, which was later famously shortened to "neurons wire together if they fire together". The resulting strengthened connections would later enable the same neurons to also fire together in the absence of the stimulus, which Hebb believed to correspond to the memory of that stimulus (Hebb, 1949). As I'll detail in the next sections, two initially separate lines of research, both predominantly focused on the hippocampus, would provide empirical support for Hebb's theory: synaptic plasticity and the hippocampal spatio-contextual map.

Recently, György Buzsáki formulated a very compelling argument for the importance of cell assemblies in the computation within neural circuit (Buzsáki, 2010) He reasoned that, since a neuron's spiking activity is relevant only in terms of its effect on downstream "readers" (i.e., other neurons) and that many coincident inputs are typically needed to discharge a "reader", the relevant "effective unit" in the brain is the combined activity of groups of neurons. Therefore, from the point of an individual "reader" neuron, all neurons whose spiking activity contributes to its own discharge effectively compose a cell assembly. This "reader-centric" definition of cell assemblies highlights the importance of precise spike timing within neural circuits. It is supported by evidence that the activity of principal cells in the hippocampus can be best predicted from the activity of their peer neurons for time windows between

10 and 30 ms (Harris, Csicsvari, et al., 2003). This is an important physiological time window because many physiological variables share it, from gamma oscillations to the cell membrane time constant and synaptic signalling.

More evidence of memory representation by specific neuronal ensembles in the hippocampus and in other brain regions came from optogenetic experiments. A series of studies demonstrated that it is possible to genetically tag neurons that are active in a particular environment, and are then thought to represent the memory associated to it (e.g a fear conditioning; (Reijmers et al., 2007; Tayler et al., 2013). It was shown, then, that by stimulating or inhibiting the tagged neurons would induce or inhibit, respectively, recall of the memory (Liu et al., 2012; Denny et al., 2014; Tanaka, Pevzner, et al., 2014). Moreover, recent work has assessed also the dynamics of such ensembles over time, highlighting the importance of the temporally precise co-activity across them (Trouche, Perestenko, et al., 2016; Ven et al., 2016).

2.3.3 Synaptic plasticity

Because of its well defined and simply layered organisation of neurons, the hippocampus is an area that has been the research target of many studies on the synaptic organisation and dynamics of neural circuits (Bliss and Lomo, 1973; Douglas and Goddard, 1975). It was found that synaptic connections between neurons can be strengthened (long-term potentiation, LTP) or weakened (long-term depression, LTD) by repeated spiking inputs or the lack thereof, respectively. LTP has been proposed as the biological mechanism underlying Hebb's rule, and, then, the main process that responsible for memory formation at the cellular level. The hippocampus and, in particular the CA1 region, has the highest concentration of N-Methyl-D-aspartate (NMDA) receptors - whose activity underlies LTP - in the brain.

2.3.4 The hippocampal spatio-contextual representation

John O'Keefe reported spatial receptive fields in complex spiking neurons (i.e., pyramidal cells) in the hippocampus of rats (O'Keefe and Dostrovsky, 1971). These principal cells were called place cells as they were found to fire at specific rat's position in space (i.e., the cell's place field), with neurons in the CA region being the most sharply tuned. Large-scale recordings of hippocampal neurons demonstrated that the fields of place cells covered the entire explored environment, constituting an internal cognitive map, and that every location was covered by multiple fields (O'Keefe and Nadel, 1978; Wilson and McNaughton, 1993; Wilson and McNaughton, 1994). Between different environments cells were found to "remap" to yield a different map from the same population of neurons (Muller et al., 1987; Colgin et al., 2008). An important implication of remapping is that across different environments different sets of hippocampal neurons are co-active, with that being crucial to the neural circuit computations, following the "reader-centric" hypothesis presented in section 2.3.2, and effectively coding for the surrounding context (Kubie et al., 2019).

These system brings mounting evidence towards the cell assembly hypothesis underpinning memory representation: not only each group of co-active place cells signals a specific location and each spatial context has multiple of such co-active groups, but also the pharmacological blockage of LTP impaired place cells formation and place cell stability was correlated to performance in a mnemonic task (C. Kentros et al., 1998; C. G. Kentros et al., 2004). The hippocampal activity, though, does not simply represent the spatial location of the animal, but it has been proposed that it represents the broader mnemonic context by encoding sequential, time-related and episodic information (Buzsáki and Llinás, 2017; Kinsky, Mau, et al., 2020).

2.3.5 Neural sensory tuning characterisation with information theory

A useful way to charecterise the activity of neuronal population is quantifying the information content with respect to a stimulus or behaviour, such as spatial location in the case of place cells, using the information theoretic formalism developed by Claude Shannon (Shannon and Weaver, 1949). The concept of information is tightly bounded to the one of entropy, a measure of uncertainty of a random variable (Cover and Thomas, 2006). In other terms, it is a measure of the amount of information required, on average, to describe a random variable, which could be the time spent by the mouse exploring the different locations s of an environment. The entropy is defined as:

$$H(S) = -\sum_{s} p(s) \log_2 p(s) \tag{2.1}$$

where S is a discrete random variable with probability distribution function $p(s)$, representing the stimulus uncertainty. As the log is in base 2, the information is expressed in bits, which is usually the preferred unit; if the base was e, then the unit would be *nats*. $H(S) = 0$ when the stimulus is unchanged, e.g. the mouse stays still in one location, and is positive otherwise, reaching a maximum value of $H(S) = \log_2 K$ when K stimuli are observed the same number of time (i.e., the uncertainty is maximum). If the neuronal response R contains some information about the stimulus S it will reduce its uncertainty defined by equation 2.1, so that the remaining unexplained entropy $H(S|R)$ (also referred to as equivocation) is obtained:

$$H(S|R) = -\sum_{s,r} p(s)p(s|r) \log_2 p(s|r) \tag{2.2}$$

, which is equivalent to the weighted average entropy of the conditional probability $p(s|r)$ (i.e., the probability of the mouse being at location s when the response r is observed; this can also be viewed as posterior distribution from a Bayesian

perspective; Quian Quiroga and Panzeri, 2009). From this, mutual information $I(R;S)$ is defined as the reduction of uncertainty (or gained information) about the stimulus obtained by knowing the neuronal response. That is subtracting the equivocation from the stimulus entropy:

$$\begin{aligned} I(R;S) &= H(S) - H(S|R) \\ &= \sum_{s,r} p(r)p(s|r)\log_2 \frac{p(s|r)}{p(s)} \\ &= \sum_{s,r} p(s,r)\log_2 \frac{p(s,r)}{p(s)p(r)} \end{aligned} \tag{2.3}$$

, where $p(s,r)$ denotes the joint probability of observing stimulus s and response r together. Mutual information (MI), like entropy, is measured in bits. If the stimuli and the responses are independent, the mutual information equals zero. Otherwise it takes positive values. Perfect knowledge about the stimulus from the neuronal activity gives a maximum mutual information of $I(S;R) = H(S)$.

All the probability quantities mentioned so far need to be estimated empirically. For example, the range of responses of each neuron, or the spatial position of a mouse along a linear track, can be partitioned into M bins, and the frequency of observing a response in each bin is computed. This can lead to 'limited sampling biases' — that is, pronounced systematic errors caused by limited amounts of data - if all possible responses (or stimuli) are not sampled well enough (Panzeri, Senatore, et al., 2007). Such under-sampling leads to an underestimation of entropy, which leads to an overestimation of MI using the plugin (or naïve) estimator shown in equation 2.3. Various methods, using both maximum likelihood and Bayesian estimation, have been proposed to remove this bias and allow MI calculations to be feasible in neuroscientific experiments where data is scarce (see Panzeri and Treves, 1996; Strong et al., 1998; Nemenman et al., 2001 Archer et al., 2013).

In the hippocampal literature, the spatial information content of place cells has been

valuable to understand the network representation (e.g. L. M. Frank et al., 2000). This quantity has been estimated with the stimulus-dependent information rate (I_{sec}), measured in bits/s, proposed by Skaggs et al., 1993, which is an approximation of the MI definition of equation 2.3.

$$I_{sec} = \sum_{s} p(s)\lambda(s)\log_2 \frac{\lambda(s)}{\lambda} \tag{2.4}$$

, where $\lambda(s)$ is the neuron's location-dependent firing rate estimation and $\lambda = \sum_x \lambda(x)p(x)$ is the mean firing rate over the whole trial. This From I_{sec}, the information per spike, measured in bits/spike is defined

$$I_{spike} = \frac{I_{sec}}{\lambda} \tag{2.5}$$

The two measures introduced by Skaggs et al. are equivalent to the average information rate conveyed by the cell and correspond to the first time derivative of the power series expansion of MI (Panzeri, S. R. Schultz, et al., 1999; Panzeri and S. R. Schultz, 2001). From

$$\mathrm{MI}(t + \Delta t) = \sum_{k=0}^{\infty} \Delta t^k \frac{\mathrm{MI}^{(k)}}{k!} \tag{2.6}$$

where $\mathrm{MI}^{(k)}$ indicates the k-th time derivative, thus the first time derivative approximates to

$$\mathrm{MI}^{(1)} \approx \sum_{s} p(s)\lambda(s)\log_2 \frac{\lambda(s)}{\lambda} = I_{sec} \tag{2.7}$$

I_{sec} and I_{spike} were found to correlate less with the accuracy of spatial decoding than the MI plugin estimator. MI could then be considered a more suitable metric to capture hippocampal spatial correlates, and maybe others types too (Souza et al., 2018).

2.4 Log-dynamic brain

As mentioned in the previous sections, the collection of brain networks underpinning memory are composed by a plethora of different actors interacting with each other, making it a complex system. Complex systems are ubiquitous in nature and are characterised by a high degree of labor diversity. In the brain, labor diversity is based on the structural and physiological differences across the units that make up its network. Brain circuits are, in fact, not only constituted by many different types of neurons and non-neuronal cells, but each types contains, in turn, a further wide range of functional neuronal profiles (Kebschull et al., 2016; Mayer et al., 2016). So, an analogy to describe a neuronal network would be an orchestra, where the interactions of different instruments give rise to a potential limitless variety of compositions. Just like the inherently skewed distribution of instrument contributions, e.g the first, second and third violin's, is central to the realisation and delivery of the composition, the inherently skewed (log-normal) distributions of brain features is central to its function (Buzsáki and Mizuseki, 2014).

Considering the wide range of properties within neuronal populations, the analysis of larger ensembles of neurons arises as fundamental to obtain a complete picture of the brain dynamics, including memory representation, which is the focus of chapter 3 of this thesis. Let me first, though, start the discussion on skewed distributions within the brain by consider a central property of cognition: log-scaled perception.

2.4.1 Log-scaled perception

An incredibly simple and pervasive law of neuroscience is the Weber-Fechner law. This law is named after two German scientists who laid the foundation for human psychophysics, a discipline that aims to find a quantitative relationship be-

tween physical stimuli and the mental state they evoke. They noticed that stimulus strength and its perception are linked by a logarithmic relationship: when the former multiplies, the latter adds. The Weber-Fechner law generalises well and applies to all senses: hearing, vision, tactile, taste and smell (Stone and Bosley, 1965). Also distance and time perception vary logarithmically with the distance or the duration of the stimulus, respectively (Gibbon, 1977; Gibbon et al., 1984). Moreover, decision making and short term memory error accumulation (Gold and Shadlen, 2000; Deco and Rolls, 2006; Buzsáki, 2015). Interestingly, not only many non-biological phenomena, such as earthquake intensity, pH scale, sound level and entropy display logarithmic behaviour, but also many sociological phenomena, like spoken and written word frequency (Zipf's law) and wealth distribution display skewed distributions. Even though Weber-Fechner law was conceived 150 years ago, the reason behind the presence of such systematic patterns within our perception remains unknown. One possible hypothesis is that the subjective properties of our action and perception are supported by the skewed, log-normal distributions with the brain structural (e.g. wiring) and dynamical (e.g. neural activity) elements (Buzsáki, 2019). Similarly, Bayesan models of the brain attempt to find a quantitative match between real-world events and brain activity patterns (Dayan et al., 1995; Friston, Stephan, et al., 2010; Friston and Buzsáki, 2016).

2.4.2 Log-scaled architecture of neuronal networks

As mentioned in the previous sections, log-normal distributions have multiplicative relationships: they arise with the multiplication of a large number of positive variables. All brains, regardless of their size, share similar brain activity patterns, such as the various brain rhythms discussed in section 2.2.2, whose computational and syntactic rules should impose a common organisational principle - i.e., integrate a plethora of local processes into globally ordered states, coherent across brain regions.

To this aim, the neural hardware should be hacked to provide flexible solutions that can work at different scales. For example, the diameter and myelination of a neuron's axon influence its signalling speed, therefore the adjustment of these two parameters seems critical for scaling-invariant computations within neuronal networks. In fact, these properties are log-normally distributed across and within species (Fig. 2.3), ensuring an efficient consumption of energy (larger fibres demand larger supply) while enabling the same local-global processing within the brain (Wang et al., 2008). Sensory fibres that can also go across hemispheres have typically large diameters, while in the frontal cortical area, where communication speed is slower due to the more complex cognitive tasks, small diameter axons dominate.

Log-normal distributions are observed also at the level of microscopic (dendritic spines, synaptic boutons) and macroscopic (the neuronal wiring organisation) connections. Spine sizes in both the neocortex and hippocampus have been reported to span more than two orders of magnitude (Loewenstein et al., 2011). Mesoscopic connectivity in brain networks also exhibits skewed distributions: the number of connections made by individual neurons locally, as well as the connection strength across different brain regions span various orders of magnitude and give rise to peculiar connectivity patterns that diverge significantly from random-wiring generated ones (Markov et al., 2011; Ercsey-Ravasz et al., 2013; I will also discuss it in more details in chapter 3). As we mentioned at the beginning of the section, the neuronal network structural organisation shapes the activity generated by the neurons within it, and the next section will delve deeper into it.

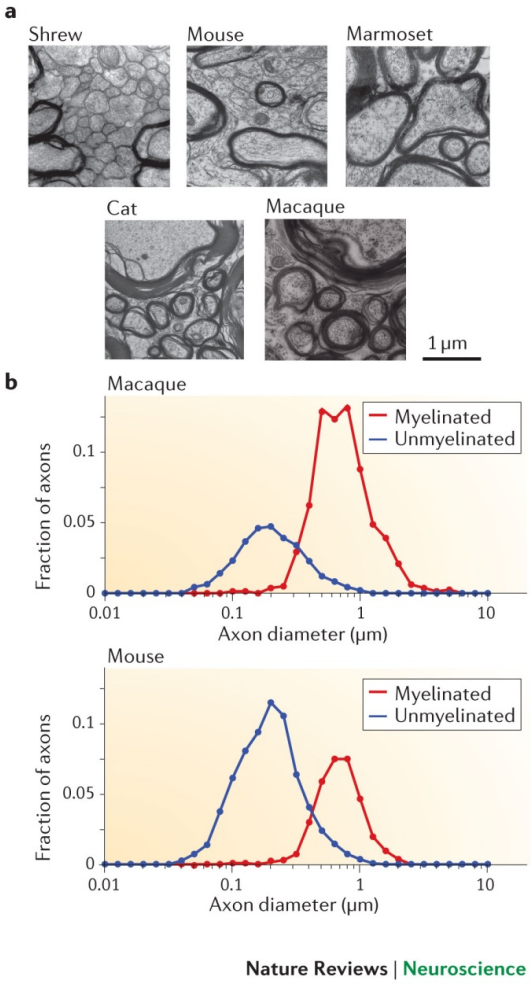

Figure 2.3: Skewed distribution of axon calibers. **a**, Representative micrographs of callosal tissue in different species. Note the various sizes of axon diameters. **b**, The distribution of diameters of unmyelinated and myelinated axons in the corpus callosum of the macaque monkey and mouse. Note the lognormal-like distribution of axon diameters. Data from. Figure reproduced with permissions from Buzsáki and Mizuseki, 2014

2.4.3 Log-scaled brain dynamics

The log-normal distributions of dendritic spine volumes suggest a large variation in synaptic weights, which regulate the functional connections among neurons. In fact, measuring the spike transmission probability between mono-synaptically connected neurons, which can be used as a proxy to assess the connection strength between them, reveals a log-normal distribution. This, in turn, means that stronger synapses not only provide a strong connection between neurons, but also a more reliable one (English et al., 2017). In fact, the neurons mean spontaneous firing rate spans around four orders of magnitude, across different brain regions and species, giving rise to very heterogeneous populations (Fig 2.4a-f). Propensity to fire burst of spikes also varies largely across neurons and displays a log-normal distribution. Thus, when considering the distribution of neuronal activity, this log-normal principle yields a large number of slow-firing neurons together with a small fraction of fast-firing, bursting cells, which can fire nearly half of the spikes recorded at any physiological time frame, such as a theta oscillations (Buzsáki, 2009; Mizuseki, Diba, et al., 2011). Interestingly, neurons scale also their firing response to stimuli (even optogenetically induced ones) to their spontaneous level of activity (Stark, Roux, Eichler, and Buzsáki, 2015). Local field potentials (LFPs), too, span many orders of magnitude in time and frequency, displaying a linear relationship between power and frequency on a log-log plane (Freeman et al., 2000; Penttonen and Buzsáki, 2003). Good evidence of such features are found in the hippocampal circuit; in fact, also synchronous neuronal events like SWR and theta oscillations show a skewed distribution in the magnitude - i.e.level of synchrony - of the event, too. In fact, larger, more synchronised events are irregularly interspersed by many smaller, less synchronised ones (Mizuseki and Buzsáki, 2013).

Such a wide range of neuronal dynamics constitutes a good framework to consider both rate and temporal codes together as different but complementary tools to

an effective and efficient information transmission in the brain. Faster neurons - i.e. following the rate code hypothesis - may provide fast, economic and highly efficient but, perhaps, less-precise communication. These neurons, by being strongly connected to all components in the network, might readily produce a "best guess" for matching behaviour to environmental situations. However, perfect and adaptive performance may require the participation of the more flexible majority of neurons, which can be fine-tuned with experience. Such "best guess" hypothesis is supported also by brain-machine interfaces applications, where only 10-20% of the recorded neurons make up approximately 60-80% of the limb kinematic or force that is being decoded (Hochberg et al., 2006).

Networks with skewed statistical properties have been shown both to provide a broad dynamic range and to offer stability, resilience and tolerance to component failures (Ikegaya et al., 2013). A 'log-dynamic' brain points toward a relatively hard-wired backbone in the neural network formed by the high activity minority of neurons, which provides readily available and routine responses. The low activity majority would then be responsible for the experience dependent, flexible and plastic component. This solution would combine the advantages of local computation and global control: synchronization, wiring economy, information storage and communication speed (Buzsáki, Geisler, et al., 2004).

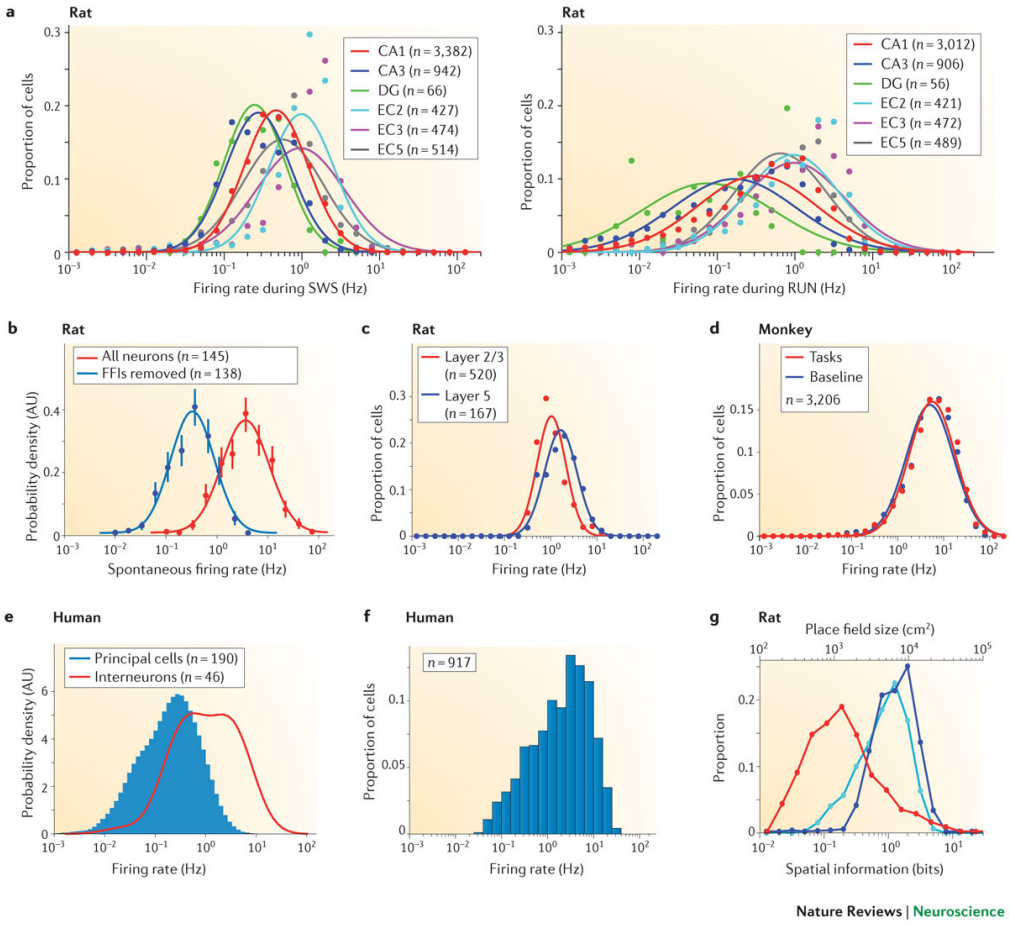

Figure 2.4: Lognormal distribution of firing rates in the cortex. **a**, Siliocon probe recordings in the rat brain showing the firing-rate distribution of principal cells in the hippocampus (CA1, CA3 and dentate gyrus (DG)) and the entorhinal cortex (EC; specifically, in layers 2, 3 and 5) during slow-wave sleep (SWS; left panel) and exploration (RUN; right panel). **b**, Whole-cell patch recordings showing the firing-rate distribution of neurons in the auditory cortex of awake rats. The two distributions show all cells and a subset, from which seven neurons with narrow spikes (that is, putative fast-firing interneurons (FFIs)) are excluded. **c**, Silicon probe recordings in the rat brain showing the firing-rate distribution of superficial (layers 2/3) and layer 5 neurons in the prefrontal cortex of an exploring rat. Neurons with a peak firing rate in the maze (¡1 Hz) were excluded from the analysis. **d**, Sharp metal electrodes data showing firing-rate distribution of all recorded neurons from lateral intraparietal and parietal reach region areas of the macaque cortex during a baseline condition and during performance of a reaching task. **e**, Utah array recordings showing firing-rate distribution of neurons in the human middle temporal gyrus during sleep. Principal cells and putative interneurons are plotted separately. **f**, Firing-rate distribution of neurons in multiple cortical areas of human patients recorded with metal electrodes during various tasks. **g**, Distribution of spatial features of dorsal hippocampal CA1 pyramidal neurons of rats exploring an open field, showing a lognormal distribution of spike information for place field. The proportion of cells plotted against the spatial information content per spike (bits per spike) are shown in dark blue; the proportion of cells plotted against the spatial information rate (bits per second) are shown in light blue; and the proportion of place fields plotted against place field size (cm^2) are shown in red. AU, arbitrary units. Figure reproduced with permissions from Buzsáki and Mizuseki, 2014.

2.4.4 Hippocampal heterogeneous population of principal cells

A potential mechanism underlying the formation of log-dynamics could be due to neurogenesis. In fact, early born neurons have a higher chance of projecting to each other and at the dendrites locations closer to the soma. Thus late born neurons innervate more prominently the more distant segments of the dendrites. Therefore, it is speculated, early-born neurons are more effective in depolarising their peers and are more likely to be within the minority of high activity cells (Buzsáki, 2019). It is the case, though, within the hippocampal circuit where a clear morphological subdivision between deep and superficial principal cells exists along the radial axis, a feature noted by early anatomists, observed in diverse species (Fig 2.5a; Lorente De Nó, 1934; Slomianka et al., 2011.In fact, together with the demonstration of transcriptional gradients along all the axis of CA1, radial included, which could manifest in cell-intrinsic differences in protein expression and functional properties (Fig. 2.5c,d; Cembrowski and Spruston, 2019), a very recent study has found that that birthdate is a strong predictor of CA1 principal cell diversity, which could support the log-normal distribution of activity and sensory tuning (Fig. 2.5b,e; Cavalieri et al., 2021).

The differences along the radial axis of CA1 were found to have differential roles in supporting behavior. Deep CA1 principal cells display higher firing rate and bursting propensity, are more likely to form place fields than superficial cells and that deep cells can shift their firing-phase preference depending on brain state (Mizuseki, Diba, et al., 2011). Importantly, studies using various in-vivo electrophysiological recording techniques report a bias in the recruitment of radially defined CA1 principal cells during hippocampal SWRs, with superficial cells firing earlier, more, and more consistently during these events (Valero et al., 2015), in agreement with the

notion that superficial and deep CA1PCs form functionally heterogeneous groups in vivo. (Soltesz and Losonczy, 2018). Moreover, the two subgroups of principal cells were found to respond differently depending on the context and task at hand: superficial cells had more stable and context-specific representations in a random foraging task, while deep cells acquired a more stable and behaviour-predicting representation during a learning task (Danielson et al., 2016).

With regard to the hippocampal spatio-contextual representation, the number of place field per cell and their size are also log-normally distributed, with a small minority having many, large place fields, regardless of the environment size (Fig. 2.4g, see also Rich et al., 2014; Alme et al., 2014). Such skewed distribution might seem detrimental from an independent coding perspective, given that the minority of neurons with multiple and larger fields could be regarded as "noise" (Marr, 1970; Marr, 1971). But considering their other physiological features, such as high firing rate and bursting propensity, higher population synchrony and stronger target excitation, such minority of high activity cells might instead play a key role also in the generalisation of hippocampal spatio-contextual representations. They might also produce the initial brain's "best guess" within novel environments: a recent study found that the c-fos-positive populations distinguish between spatial contexts display high mean firing rates (Tanaka, He, et al., 2018). The majority of low activity neurons, instead, could flexibly encode the details of individual events, as LTP and LTD can induce new place cells and make place cells disappear, an effect most strongly expressed in slow-firing place cells (Dragoi et al., 2003).

The coexistence of a highly firing minority and a low activity majority of place cells supports the theory of cell assemblies (Hebb, 1949). The latter proposes that neurons form synchronised assemblies whose activity is modulated by sensory inputs - such as the spatial position of the animal in the case of place cells. Constituting these assemblies, there are rigid and plastic principal cells: place cells encoding

spatial memories were found to be formed by a subgroup of relatively fast firing cells, with stable temporal, rigid dynamics, and by a subset of slowly firing neurons, with more adaptive, plastic dynamics (Grosmark and Buzsáki, 2016). The latter acquire highly selective spatial firing patterns and show increased recruitment during post-exploration/experience SWR events. Rigid place cells, instead, show low spatial selectivity and were shown to maintain global stability in the network, thus allowing the plastic majority to adapt its activity to the novel environment (Panas et al., 2015). It was found out that the activity of individual place cells can be better predicted by considering the activity of neighbouring synchronised neurons - which are part of the same cell assembly - together with the spatial location of the animal (Harris, Csicsvari, et al., 2003). The optimal time window for predicting one cell's spike timings from the activity of neighbouring neurons is 10-30ms, which matches the cellular membrane time constant, the gamma oscillation period and the temporal interval for synaptic plasticity to take place. Therefore, precise temporal activity and assembly dynamics at this time scale could be optimal for memory transmission and storage in cortical circuits. In such a regime, neocortical storage sites may house relatively more stable memories that hippocampal computations incrementally modify (Kumaran et al., 2016).

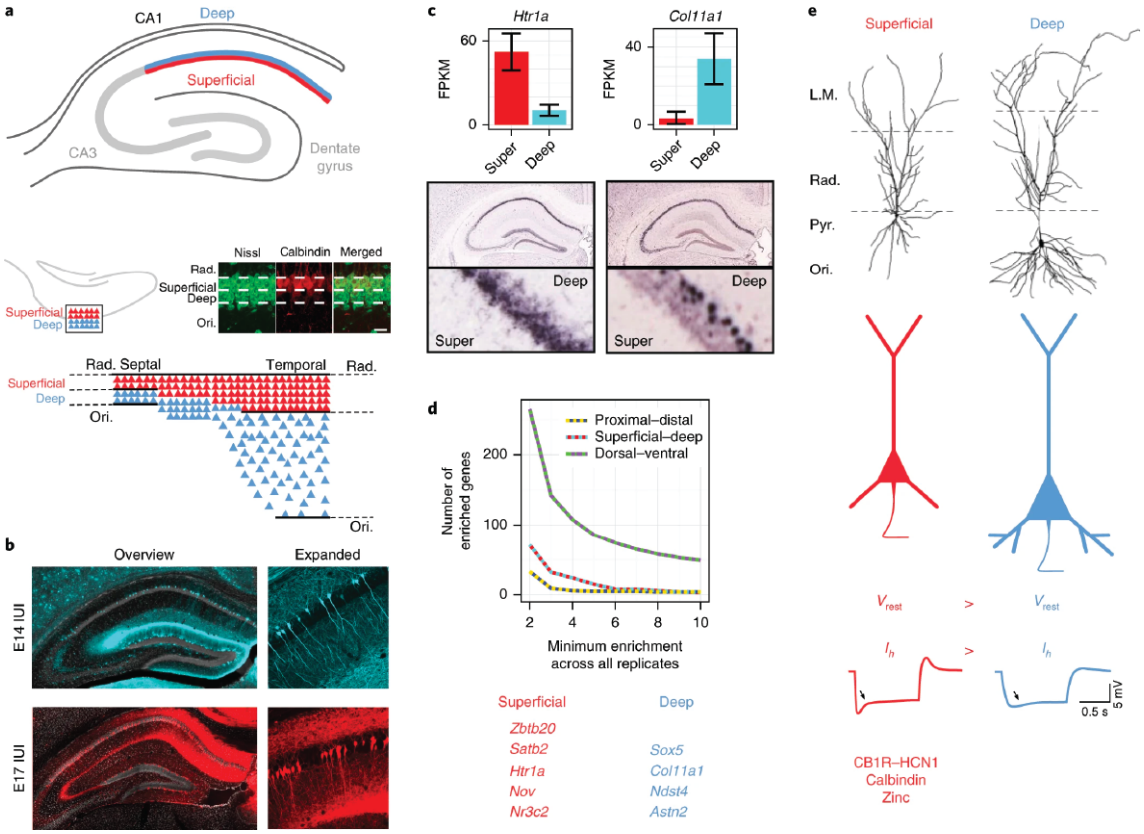
a
CA1
Deep
Superficial
CA3
Dentate gyrus
Nissl
Calbindin
Merged
Rad.
Superficial
Deep
Ori.
Rad. Septal
Temporal
Rad.
b
Overview
Expanded
E14 IUI
E17 IUI
c
Htr1a
Col11a1
FPKM
60
0
40
Super
Deep
d
Proximal–distal
Superficial–deep
Dorsal–ventral
Number of enriched genes
200
100
0
2
4
6
8
10
Minimum enrichment across all replicates
Superficial
Deep
Zbtb20
Satb2
Htr1a
Nov
Nr3c2
Sox5
Col11a1
Ndst4
Astn2
e
Superficial
Deep
L.M.
Rad.
Pyr.
Ori.
V_{rest}
>
I_h
5 mV
0.5 s
CB1R–HCN1
Calbindin
Zinc

Figure 2.5: Developmental, genetic, morphological, and intrinsic electrophysiological differences between radially defined CA1 principal cells sublayers. **a**, Top: schematic illustrating coronal section of the hippocampus with major subregions. Middle left: schematic drawing illustrates the deep (blue) and superficial (red) subdivisions of the CA1 somatic layer. Middle right: calbindin expression in the superficial sublayer in the septal CA1. Scale bar, 20μm. Rad., stratum radiatum; Ori., stratum oriens. Bottom: differences in the cellular compactness and width of the deep and superficial CA1 principal cells (CA1PCs) sublayers along dorsoventral axis of the hippocampus.**b**, Superficial and deep CA1PCs are generated in different time-windows during embryonic neurogenesis: in utero intraventricular injections (IUI) of tdTomato-expressing adeno-associated virus at embryonic day 14 (E14, cyan) and E17 (red) label deep and superficial CA1PCs, respectively. Pyramidal cells of the densely packed superficial layer in CA1 arise approximately 2–3 d after those of the deep layer, on average. **c**, Two example marker genes for superficial and deep sublayers identified with RNA sequencing (top) and cross-validated with in situ hybridization (bottom); gene-expression values (top) are expressed in fragments per kilobase of exon per million fragments mapped (FPKM). Super, superficial. **d**, Top: the number of enriched genes as a function of the minimum enrichment across all replicates using bulk RNAseq. Note that the dorsoventral axis exhibits the most robust gene-expression differences, but there are many enriched genes across both the superficial–deep and proximodistal axes as well. Bottom: examples of genes enriched in the superficial and deep sublayers. Differences in gene expression may relate to functional differences between layers. Differences in gene expression may relate to functional differences between layers: calbindin-deficient mice and mice with deletion of the gene encoding the transcription factor Zbtb20, which controls calbindin expression, demonstrate deficits in hippocampal-dependent learning and LTP. Zbtb20 expression is maintained throughout adulthood in superficial CA1PCs, and its expression is mutually exclusive with that of Sox5, a marker of deep CA1PCs **e**, Morphological and intrinsic electrophysiological differences between superficial and deep CA1PCs. Top: representative camera lucida drawings of a superficial CA1PC and a deep CA1PC. L.M., stratum lacunosum-moleculare; Rad., stratum radiatum; Pyr., stratum pyramidale; Ori., stratum oriens. Deep cells have larger soma and more complex basal dendrites. Note that calbindin-expressing CA1PCs, primarily located in the superficial sublayer, have more complex apical dendritic arborizations (not shown). Middle: superficial CA1PCs exhibit a more strongly depolarized somatic resting membrane potential (V_rest) and a larger somatic h-current that mediates a depolarizing sag (indicated by arrow) during hyperpolarizing current pulses. Bottom: examples of superficial CA1PC-biased signaling pathway, calcium-binding protein, and a divalent ion. H-current, a major regulator of dendritic excitability and synaptic input integration, is larger in superficial CA1PCs, and recent results indicate that tonic activity of postsynaptic cannabinoid type 1 receptors (CB1R) maintains the amplitude of I_h through a dedicated molecular pathway in these cells. HCN1, hyperpolarization-activated cyclic nucleotide-gated channel. Figure reproduced with permissions from Cembrowski and Spruston, 2019.

Chapter 3

A network science framework for systems neuroscience

As Camillo Golgi first observed using silver nitrate staining (Golgi, 1885) and Santiago Ramón y Cajal detailed and artistically depicted using light microscopy (Ramón y Cajal, 1888), the neural circuitry is not a single homogeneous reticulum but is instead a network composed of individual, anatomically distinct nerve cells with complex interconnections. Networks of neurons use spikes to communicate (Bialek et al., 1999), which is the substrate for all the codes and operations that give rise to perception, action and memory. Therefore understanding these phenomena requires understanding the spiking activity across populations of neurons (Pouget et al., 2013; Yuste, 2015).

The latest technological advances allow us to simultaneously capture the activity of hundreds, thousands of neurons in different brain systems. These can span from invertebrate locomotion and motor control, through higher-level mnemonical tasks in rodents to abstraction-driven decisions in primate prefrontal cortex (see section 2.3.1). Once the data is recorded, the key question becomes how do we get insights into the system: how do we describe this population-wide spiking activity? How should we visualize and represent it? And how do we discover the coding and

computations therein?

Network science and graph theory gives us powerful tools for studying complex systems, such as brain circuits (see section 2.4), by representing, analysing and modelling the dynamics of a multitude of components interacting together. Networks, or graphs, are simply a collection of nodes, representing items, and edges between them, representing the interactions between items. Such representations can be used to study a range of diverse systems: from interaction within social groups, through economic and industrial processes, to word structure in a text (Newman, 2003). By abstracting these systems to a network description, we can study their topology, compare them and decompose them in their functional elements. It is important to stress that the edges in these networks do not necessarily represent a physical connection between nodes but they can signify any interaction of interest between them (i.e. friendships in a social network).

Apart from mapping the physical structure of brain regions, graph representation has been employed in neuroscience to yield insightful descriptions of neural circuits activity: from mesoscale neural data in human subjects, to optical and electrophysiological readout of neural activity in animals (Bullmore and Sporns, 2009; Bassett and Sporns, 2017; Humphries, 2018). In these networks, the nodes are either local brain circuits (in MEG, EEG, fMRI recordings) or individual neurons (in optical and electrophysiological recordings) and the edges represent the interactions between them.

In this chapter I will focus on networks representing the co-firing interactions within neuronal populations, surveying graph-theoretical tools and concepts to characterise their topology. The data used are electrophysiological recordings of putative pyramidal cells in the hippocampal dCA1 region in mice freely exploring different arenas

(n=1,083 total principal cells; 63.7±33.2 principal cells per day; 17 days from 7 mice. For details on the recordings procedures see section 4.2.1).

3.1 Network characteristics

As mentioned before a network is comprised of nodes and edges. In our case, the nodes are individual neurons and the edges represent the interaction between them (Fig. 3.1b). The interactions can be computed from any pairwise metric between the timeseries activity of any two neurons. A critical feature of any interaction metric is whether it is directed or not, which consequently makes the resulting network symmetric or not. Frequent choices of interaction metric are the cosine similarity or the Pearson correlation coefficient (both undirected) as these measures are easy to interpret, compute and are not data-intensive. Nonlinear metrics can also be used, when sufficient data is available: these include mutual information (undirected; Singh and Lesica, 2010; Bettencourt et al., 2007), transfer entropy (directed; Schreiber, 2000; Thivierge, 2014), interaction measures tailored for binary spiketrains (their use in defining networks interaction is unclear though; Lyttle and Fellous, 2011; Rossum, 2001; Victor and Purpura, 1996), the weights of a Generalised Linear Model (GLM; directed; Pillow et al., 2008) and biophysically inspired ones (directed; Billeh et al., 2014). It is to be stressed, though, that measures of pairwise interaction alone cannot distinguish whether the correlations are caused by common inputs to both neurons or whether they are indeed physically connected (Das and Fiete, 2020).

Irrespective of the interaction metric selected, a network is represented as a graph,

defined by its adjacency matrix, A, which is an NxN square matrix (Fig. 3.1c):

$$A = \begin{pmatrix} w_{00} & \dots & w_{0N} \\ \vdots & \ddots & \vdots \\ w_{N0} & \dots & w_{NN} \end{pmatrix} \tag{3.1}$$

where N is the number of nodes in the graph; and each element, w_{ij}, is a continuous weight value that corresponds to the chosen interaction measure between two nodes i and j. In the case of a binary graph $w_{ij} = a_{ij}$, where a_{ij} is a binary variable reporting whether there is an edge between i and j. As we want to represent the co-firing associations across neurons, dense weighted graphs are formed using the Pearson correlation coefficient r to measure the coactivity interaction between any two cells. In this way we consider also the weak interactions across neurons, which are discarded by the commonly used thresholding techniques, that may contain relevant information (Humphries, 2011; Zanin et al., 2012; Khambhati et al., 2015). To build dense weighted graphs, we evaluate r using the continuous variables obtained from smoothing the two selected spike-trains, which are first binned at 0.8 ms to ensure the resulting vector is binary, with a Gaussian kernel (SD=20ms) (Fig. 3.1a). This operation yields a continuous and bounded measure of the co-firing relationship between any pair of neurons - i.e, $-1 \leq r \leq 1$ - that is easy to interpret and to compute . Moreover, A is symmetric as the metric is undirected - i.e. $w_{ij} = w_{ji}$ -; this greatly simplifies the topology of the network allowing us to exploit its Riemmanian properties, as I will describe in section 3.3. Other measures, such as the ones mentioned earlier could have been employed but the additional computational burden was found not to be justified as the simple r measure is already well capturing the neurons co-firing associations. It is important to note though that our choice of Gaussian kernel is justified by the neuron's membrane time constant of 20ms (Suszkiw, 2012). Such a "binless" approach was shown to give Pearson correlation coefficient estimates that are equivalent to the ones produces by coarser

binning procedures, without introducing the quantisation noise introduced by the bin estimate (P. B. Kruskal et al., 2007). The convolution step introduces dependencies between the individual samples, which, in this case, are assumed to reflect the transmission effect induced by the neuron membrane capacitance, but might also produce spurious effects if the kernel width is not reflecting the properties of the underlying system. With respect to hippocampal principal cells activity, another alternative approach would be using bins matching the duration of individual theta cycles, as they are believed to be a fundamental element of the syntax used by the hippocampus to encode information (see section 2.2.2).

3.1.1 Connection strength

Connectivity is an important and fundamental measure of a graph. Node i's connectivity is quantified by its strength, S_i, in the case of weighted graphs, which is the equivalent to the degree k_i in the case of binary graphs - i.e, the number of connections made by each node.

$$S_i = \sum_{j=1}^{N} w_{ij} \tag{3.2}$$

The simple sum is taken instead of the sum of the amplitude of the coefficients because it aims to capture also the sign of the correlation strength of each neuron, not just its magnitude. The example in Fig. 3.1 shows the skewed distribution of co-firing strength within a dCA1 pyramidal cells network (Fig. 3.1e), which arises from a power-law distribution of their co-firing associations (3.1d). Such skewed distributions points to the presence of a minority of highly coactive neurons, a characteristic of log-dynamic brain circuits (see section 2.4). Recurrent neuronal dynamics are known to produce by chance wide neuron pairwise neuronal correlation distributions centered The positive bias of the co-firing associations distributions suggest that a common input could be synchronising the neurons activity together (Renart

et al., 2010). Employing a GLM to predict the activity of cell i from two separate inputs, namely the activity of another cell j and the remaining population activity or a concurrent behavioural state such as the animal speed. Employing the beta coefficient of the trained GLM to quantify the pairwise neuronal interactions could then possibly discriminate between the independent co-activity between neurons i and j and the one induced by shared external inputs.

What discussed up until now is enough to define the connectivity of i in an undirected graph. In the case of a directed graph though, every node has two strength values associated with it, for inward and outward connections. The two quantities are defined by summing over either the rows or the columns of A separately.

$$S_i^{in} = \sum_{j=1}^{N} w_{ji} \qquad S_i^{out} = \sum_{j=1}^{N} w_{ij}$$

3.1.2 Geodesic path length

The geodesic path between any two nodes in a graph is the shortest possible route between them. Its length - i.e. the shortest path length - measures the ease of connection between any two nodes in a network, which captures their information transmission potential. In the case of a co-firing neuronal network, the geodesic path length captures the level of coordination between the neurons' activity. If the graph is binary, the shortest path length is just the smallest number of edges that connects any given two nodes. In weighted networks, it is useful to attach a physical quantity to the edges of the network if we were to embed it in a D-dimensional space (R^2 or R^3 typically). The co-firing distance between two nodes i and j is then defined as

$$d_{ij} = \frac{1}{w_{ij}} \tag{3.3}$$

discarding all negative edges. Possibly, to avoid discarding all negative edges, an alternative approach would be to create equivalent positive weights by adding 1

to all the entries in the co-firing matrix, mapping negative weight to the range $0 \geq x < 1$ and positive weights to $1 < x \leq 2$. This operation, though, would distort the resulting distances d as differences between negative weights would be given more relevance than distances between positive weights. As $1/x = x^{-1}$ is a non-linear function, its slope in the range $0 \leq x < 1$ its much steeper than in the range $1 < x \leq 2$. Given that most of the co-firing relationship have positive values (see section 3.1.1) discarding the negative minority was deemed more appropriate but this should be tested by comparing the two measures empirically.

Once we have defined a distance metric, we may want to find the shortest path between any two nodes in the network by minimising the total length between them, so to obtain their pairwise geodesic path length L_{ij} (Figure 3.1d; Boccaletti et al., 2006). To compute this quantity in dense networks we employ the Floyd-Warshall algorithm (Floyd, 1962; Warshall, 1962; Roy, 1959) as the frequently used Dijkstra's algorithm is only applicable to sparse graphs (Djikstra, 1959). To every neuron we can then assign an average geodesic path length L_i

$$L_i = \frac{1}{N} \sum_{j=1}^{N} L_{ij} \tag{3.4}$$

In Fig.3.1g the distribution of L among a neuronal population is shown, it is heavy-tailed suggesting a wide range of individual cells synchronisation across the network.

3.1.3 Clustering coefficient

The clustering, also known as transitivity, of a graph measures the number of closed triangles, or triplets, formed by interconnected nodes. In a social network this is intuitively represented by two friends that share a common third friend. The

transitivity T of a graph is defined as

$$T = \frac{3N_{tri}}{N} \tag{3.5}$$

, where N_{tri} is the number of triangles in the graph. An alternative measure is the clustering coefficient, introduced by Watts and Strogatz (Watts and Strogatz, 1998), which defines a node-wise measure instead of a graph-wise, such as T. The clustering coefficient C_i of node i aims to quantify how likely are two of its neighbours of being connected. In a binary graph, C_i is defined as the ratio between the number of edges e_i present in its neighborhood, i.e, within the subgraph G_I made by i and all the nodes connected to it, and the maximum possible number of edges within G_i, $k_i(k_i - 1)/2$.

$$C_i = \frac{2e_i}{k_i(k_i - 1)} \tag{3.6}$$

In this study. we want to calculate the clustering coefficient in signed weighted networks, to quantify the propensity of individual neurons to form triads of coactivity within the network. Using a modified version of the formula proposed by Onnela et al. (Onnela et al., 2005; Saramäki et al., 2007; Costantini and Perugini, 2014):. For any neuron i, we can then obtain its clustering coefficient C_i as

$$C_i = \frac{\sum_{jm}(\hat{w}_{ij}\hat{w}_{im}\hat{w}_{jm})^{1/3}}{k_i(k_i - 1)} \tag{3.7}$$

where j and m are neighbors of neuron i, all edge weights are normalized by the maximum edge weight in the network $\hat{w} = w/\max(w))$, and k_i is the degree of neuron i, which in these dense weighted graphs with no self-connection is equal to the number of neurons minus one. Note that this formula accounts naturally for negative edges: a given triad yields a negative contribution when there is an odd number of negative edges; it is positive otherwise.

In Fig. 3.1h an example of the clustering coefficient distribution among a dCA1 network is shown. The distribution is asymmetric, skewed, which suggests that a minority of pyramidal cells participate to a great number of neuronal coactivity motifs (triplets), while the majority does not. This behaviour is related to the log dynamics within brain circuits, which is discussed in depth in section 2.4.

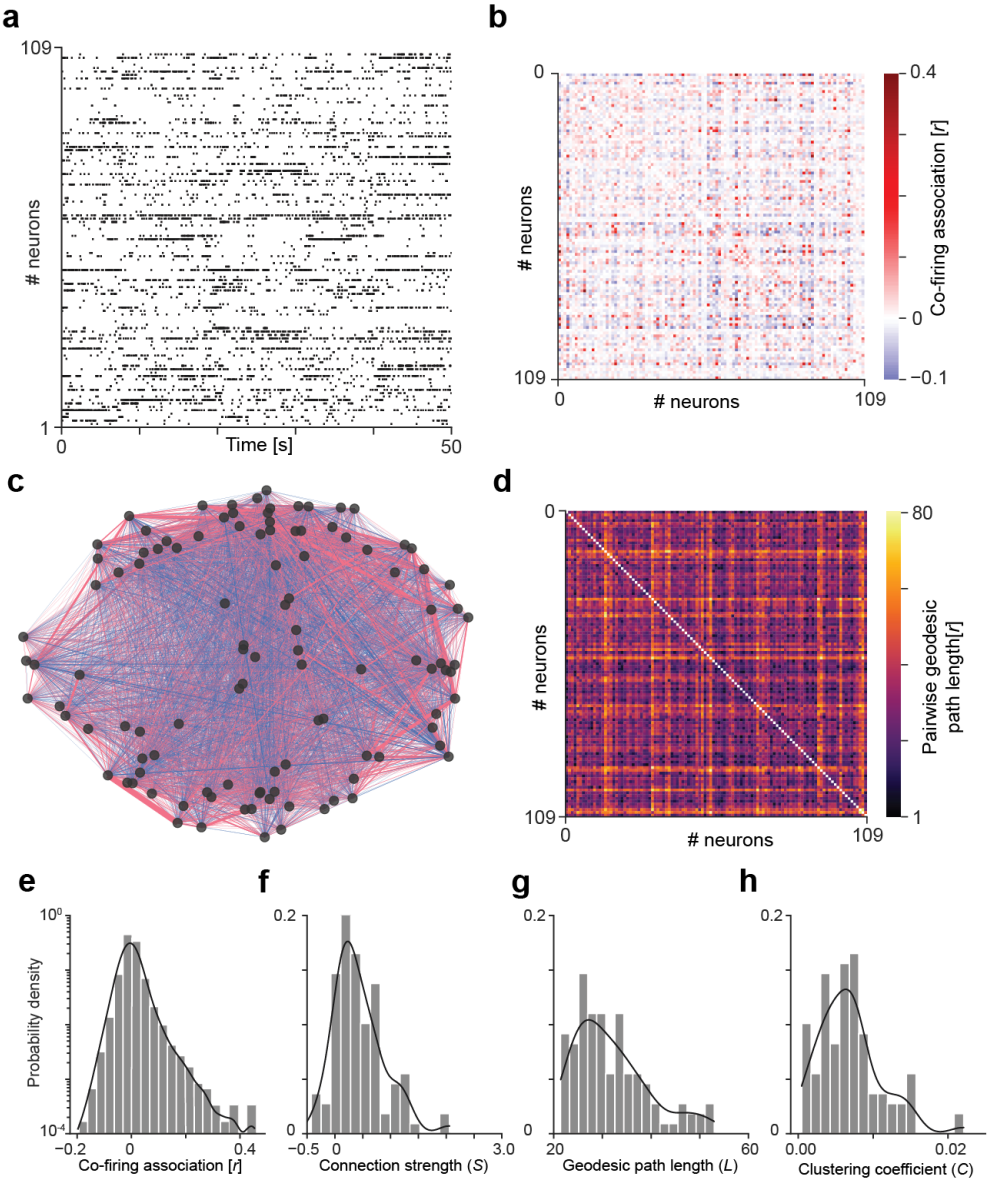

Figure 3.1: Representing the co-firing relationships among a population of neurons using dense signed weighted graph. **a** An exemplar raster plot displaying the spiking activity from 109 simultaneously recorded pyramidal cells in the mouse hippocampal dCA1 as the animal was freely exploring an arena. For clarity, a 50-s sample is shown. **b**, The adjacency matrix representing the pairwise Pearson correlation coefficient measuring the co-firing of pyramidal cells for the same recording as in **a**. **c**, The corresponding graph graph is visualised using the Fruchterman-Reingold force-directed algorithm. Each node represents one cell. Each edge represents the co-firing association of one cell pair, color-coded according to their correlation's sign and width proportional to the edge's absolute value **d**, The corresponding pairwise geodesic path length matrix. **e**, Skewed probability distributions of neuron-wise connection strength (left), geodesic path length (middle) and clustering coefficient (right) for the exemplar network shown in the previous panels.

3.2 Neuronal circuits as small-world networks

Main real-world networks share a common small world architecture, characterised by a low average geodesic path length and a high clustering coefficient, which supports many important functions such as synchronisability and information flow (Nishikawa et al., 2003; Lu et al., 2004; Oliveira et al., 2014). This topology was first described by Watts and Strogatz, who developed a simple model starting from a binary, highly-regular (lattice) network which has some of its connections randomly rewired (Watts and Strogatz, 1998). In this way, small network boast a high clustering while allowing fast navigation across it. Famous examples of small world networks include social networks, email traffic, the internet and many biological networks. Neural networks have also been described as small world: the canonical example being the neural network of the worm *Caenorhabditis elegans*, but also the anatomical tracing of the wiring within the brain of mammals, including humans, and its functional activity (EEG, MEG, fMRI) have revealed strong locking (high clustering) of dynamics across neurons and cohesive activity across the population (short path length) (Bullmore and Sporns, 2009; Bettencourt et al., 2007; Sadovsky and MacLean, 2013).
The small-world network description given by Watts and Strogatz is tailored for theoretical investigations of the model but unfortunately it is not useful to describe real-world data. The Small-world Index (σ) is the most common statistics used to quantify the small-world-ness of real-world networks (Humphries and Gurney, 2008). The idea behind this index is simply to compare the geodesic path length (L_{data}) and clustering coefficient (C_{data}) of the network of interest with the ones of a random (Erdos-Renji) network (L_{rnd}, C_{rnd}), as a small-world network has a geodesic path length larger, but comparable, to a random network while it has a much larger clustering. Then, the following quantities are defined:

$$\gamma = \frac{C_{data}}{C_{rnd}} \qquad \lambda = \frac{L_{data}}{L_{rnd}}$$

$$\sigma = \frac{\gamma}{\lambda}$$

if the network is small-world it will have $\gamma > 1$ and $\lambda \approx 1$, leading to $\sigma > 1$. Therefore if a network has $\sigma > 1$ is said to be small-world - is to be noted, though, that σ has no upper bound. The small-world index was defined for binary networks but it can be applied to weighted networks as well (Colon-Perez et al., 2016). The main drawback of σ is that, by comparing the topology of the network of interest only with random networks, lacks in sensitivity because the clustering coefficient of random networks can be very low. This is especially exacerbated when the edge density of the network increases, such as in dense weighted graphs, leading to a large γ, and therefore $\sigma > 1$, even if the network is not particularly clustered. To overcome this issue, two indexes were developed taking into consideration the topology of the equivalent lattice network as well as the random one. Telesford et al. defined a new metric ω as

$$\omega = \frac{L_{rnd}}{L_{data}} - \frac{C_{data}}{C_{latt}}$$

where the clustering coefficient of the target network is now normalised by the one of its lattice equivalent (C_{latt}) an not by the random one (Telesford et al., 2011). This leads to ω being bounded in the range [-1, 1]: if ω is close to 0 the network is considered to be small-world, if it is, instead, closer to 1 it indicates the network is most similar to a random one, while a negative ω indicates a strongly regular topology. This index is only defined for binary networks, though, limiting its use on real-world data. Nonetheless, this index has been used to identify the small-world regime accurately and it has been applied successfully to modelling and neural data but it remains density dependent and is not applicable to weighted networks (Zippo et al., 2013; Acimovic et al., 2015; Pritchard et al., 2014). To tackle weighted networks of varying density, the Small-world Propensity (ϕ) has been introduced (Muldoon et al., 2016)

$$\phi = 1 - \sqrt{\frac{\Delta C^2 + \Delta L^2}{2}}$$

where,

$$\Delta C = \frac{C_{latt} - C_{data}}{C_{latt} - C_{rnd}}$$

$$\Delta L = \frac{L_{rnd} - L_{data}}{L_{rnd} - L_{latt}}$$

The ratios ΔC and ΔL represent the fractional deviation of the metric (C_{data} and L_{data}) from its respective null model (a lattice or random network). Posing a boundary on $L_{data} \geq L_{rnd}$ and $C_{data} \leq C_{latt}$ guarantees that ϕ is within the range [0, 1]. Values of ϕ close to 1 indicate that the network displays high small-world characteristics. Networks with high small-world characteristics (low ΔC and ΔL) will have a value of ϕ close to 1, while lower values of ϕ represent larger deviations from the respective null models for clustering and path length, and display less small-world structure. Muldoon et al. empirically selected $\phi > 0.6$ as a threshold for a strong small-network topology, but as ϕ allows to distinguish across different degrees of small-world-ness, they also noted that 0.4 indicate a weak small-network topology.

To assess the small-world-ness of the hippocampal dCA1 multi-neuron data, I first construct null network models to compare the target networks topology to. The random network equivalent is built by random shuffling the edge weights in the real network (Fig. 3.1b-c) to obtain a symmetric graph with no self-connections (Fig 3.2a,c). For the lattice network equivalent, instead, I re-organise the real network weights to construct a 1D highly clustered lattice (i.e., a ring topology) that displays the strongest connections between neighbouring neurons. To do so, I consider the row/column location in the adjacency matrix a proxy of the physical location of the neurons, which is supported by the natural ordering of tetrode-recorded cells. To then construct the lattice equivalent network I assign the strongest weights in the real network first to the connections between adjacent nodes within the 1D lattice (i.e., starting from d=1 Euclidean distance along the ring), and only once all adjacent weights are assigned I start filling the d¿1 locations (Fig. 3.2b,d; Muldoon

et al., 2016). As expected, the geodesic path length and clustering coefficient of the units in the random network is smallest, while the units in the lattice network show the greatest values (Fig. 3.2e). Within a random network it is, in fact, easy to move from one node to any other but there is very little local structure; a lattice networks, on the other hand, has a very regular and clustered local structure that makes it difficult to move between faraway nodes (no shortcuts are present). Moreover, in the random and lattice equivalent networks the clustering coefficient and geodesic path length have symmetric and narrower distributions compared to the skewed ones of the neuronal network (Fig. 3.2e).

Once the correct null models are built, it is then possible to assess whether the neuronal networks display a small-world structure and quantify it. We find that the hippocampal dCA1 networks of pyramidal cells (n=102 graphs; 260,058 co firing pairs) have $\sigma = 6.09 \pm 0.41$ (mean $\pm$ SEM; Fig. 3.2f, left) and $\phi = 0.575 \pm 0.019$ (mean $\pm$ SEM; Fig. 3.2f, right). These results suggest that these cellular dCA1 networks have a weak small-world topology, therefore not displaying a strong hierarchical structure. I find that $\sigma > 1$ for 97.1% of the networks examined, but this measure is not very accurate and tends to overestimate, as previously discussed. Instead, the more specific Small-world Propensity indicates that 87.3% of the networks have $\phi > 0.4$, suggesting a weak small-world structure, while only 15.6% have $\phi > 0.6$, which is a hallmark of a stronger small-world topology.

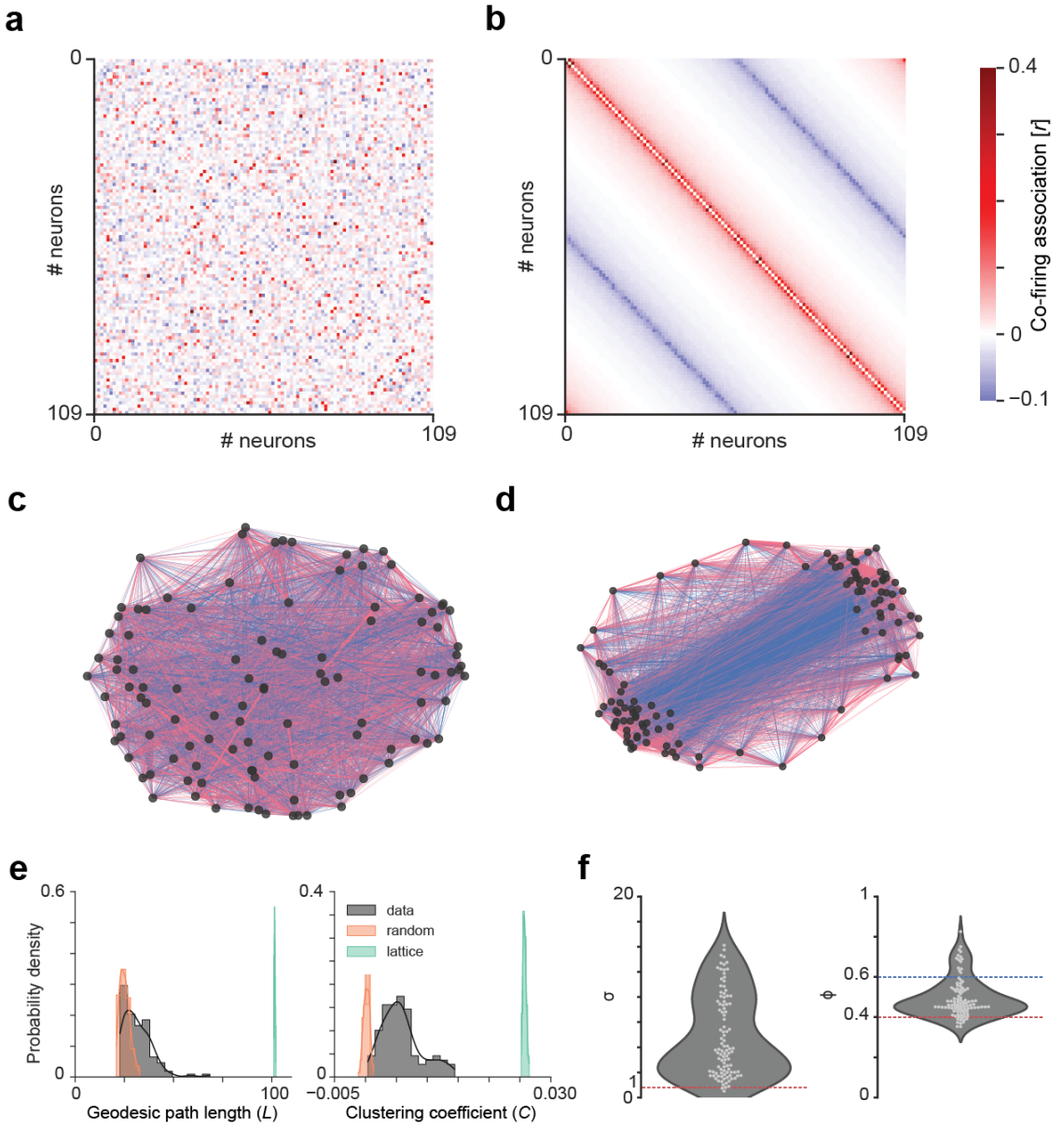

Figure 3.2: Assessing small-world structure of the hippocampal dCA1 pyramidal cells network. **a** The adjacency matrix of a random network equivalent to the target network in Fig 3.1. **b**, The adjacency matrix of a lattice network equivalent to the target network in Fig 3.1 **c**, The random network in panel **a** visualised as a graph using the Fruchterman-Reingold force-directed algorithm to position the nodes. **d**, The lattice network of panel **b** is visualised in the same way as in panel **c**. **e**, Right, the clustering coefficient distribution for the nodes in the dCA1 network (Fig 3.1), in its equivalent random network (panels **a**, **c**) and in the lattice one (panels **b**, **d**). Left, the clustering coefficient distribution for the nodes in the same three networks as in the left panel. **f**, Left, Small-world Index σ for all (n=102) the dCA1 networks examined ([5.29, 6.90], 95% confidence intervals for the mean). Right, the Small-world propensity ϕ for the same networks sample ([0.48, 0.53], 95% confidence intervals for the mean).

3.3 Distance metrics between networks: a Riemannian approach

Apart from describing the topology of neuronal networks using ad-hoc measures, one may wish to compute the overall change that emerges within a network across different conditions. To do so, a measure of similarity is needed. In this section I will describe an alternative approach to the commonly used methods, which exploits the symmetric structure of correlation matrices, like the one representing the coactivity in a neuronal network described in section 3.1.

Correlation matrices are used often in neuroimaging studies (usually fMRI) where they are referred to as functional connectivity (FC) matrices, and have demonstrated a fundamental component of many investigations (D. H. Schultz and Cole, 2016). A common approach to compute the proximity or similarity between to FC matrices is to "unroll" them into vectors and then compute the Pearson correlation between them. Indeed, the correlation approach has yielded outstanding results in the neuroimaging field, such as successfully identifying a participant out of a large group of participants based on FC matrix similarity (Finn et al., 2015; Amico and Goñi, 2018). Related approaches include computing the Euclidean distance between the matrices (Ponsoda et al., 2017), or using the Manhattan distance (Allen et al., 2014). Matrices computed by Pearson correlating time series data such as the dense weighted coactivity networks introduced in section 3.1 are positive semidefinite matrices. Therefore they lie on a non-linear surface, a Riemannian manifold, called the positive semidefinite cone: their geometry is non-Euclidean (Boyd and Vandenberghe, 2004; Moakher, 2005). Accordingly, distances between correlation matrices must be measured along the surface of the cone: the shortest curve joining two points (matrices) on the cone is called a geodesic and are the most accurate measure of the distance between two points laying on a manifold

(Fig. 3.3; Navarro-Sune et al., 2017).

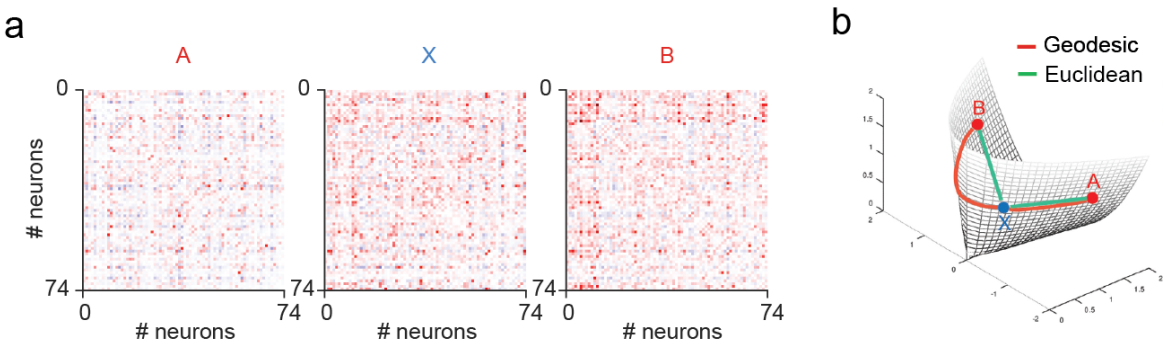

Figure 3.3: Geometry of symmetric positive semidefinite matrices representing neuronal networks. a The adjacency matrices representing the co-firing structure of the same network during three different exploration sessions and conditions. **b**, Illustration of geodesic (red) and Euclidean (green) distances on the so-called positive semidefinite cone. A, B and X, the three adjacency matrix of **a**, are represented as points on the cone and the distance among them is correctly described by the geodesic distance and not by the Euclidean one. This panel is adapted with permissions from Venkatesh et al., 2020.

Such geodesic distances are well defined and computationally tractable on Riemannian manifolds. The affine Invariant metric D_{AFF} (introduced in Pennec et al., 2006) defines the geodesic between two $N \times N$ positive semidefinite matrices A and B laying on a Riemannian manifold as

$$D_{AFF}(A,B) = \sqrt{\text{trace}(\text{Log}^2(A^{-\frac{1}{2}}BA^{-\frac{1}{2}})} \tag{3.8}$$

, where $\text{Log}(\cdot)$ is the matrix logarithm, the inverse of the matrix exponential defined as: $exp(A) = \sum_{k=0}^{\infty} A^k/k!$. Note that this notation implies that A is invertible, so we add the identity matrix I to both matrix to ensure that all eigenvalues are greater than 0. If we set $Q = A^{-\frac{1}{2}}BA^{-\frac{1}{2}}$ and λ_i, for $i = 1$ to N, are the N eigenvalues ≥ 0 of Q, the affine invariant distance is simply

$$D_{AFF}(A,B) = \sqrt{\sum_{i=1}^{n} \log(\lambda_i)^2} \tag{3.9}$$

An alternative framework to define operations on symmetric positive semidefinite matrices is the Log-Euclidean framework (Arsigny et al., 2006). By taking a logarithmic mapping of a positive semidefinite matrix, a geodesic $D(A, B)$ on a Riemannian manifold M is projected to its tangent plane at A where Euclidean geometry can be used. Then, from a Euclidean norm on symmetric matrices $\|\cdot\|$, the distance D_{LE} between two matrices is given by:

$$D_{LE}(A, B) = \|\mathrm{Log}(A_1) - \mathrm{Log}(A_2)\| \tag{3.10}$$

The formulation in eq. 3.10 is much simpler to compute than the ones in eq. 3.8 and 3.9, as matrix multiplication and matrix inverse have to be performed.

To motivate why geodesic distance are preferable over the Pearson correlation distance, consider that the Pearson correlation between two vectors is equivalent to the cosine of the angle between them after they have been individually "centered" (i.e, the mean of each vector is subtracted from it) and normalized. Indeed, this operation allows the Pearson correlation to discard the contribution of the signal mean, as can be readily seen in the following equation:

$$corr(x, y) = \frac{\sum_i (x_i - \bar{x})(y_i - \bar{y})}{\sqrt{\sum_i (x_i - \bar{x})^2}\sqrt{\sum_i (x_i - \bar{x})^2}} \tag{3.11}$$

, where x and y are vectors. For correlation matrices, such centering alters the eigenvalues and the positive semidefiniteness of the matrix, which can lead to distortions when evaluating the similarity between correlation matrices.

3.4 Outlook

In this chapter we set out an analytical framework to investigate the coactivity interactions within neuronal network using graph theory and topological concepts.

Such methods are part of the broader network science approach to neuroscience (Bassett and Sporns, 2017; Humphries, 2018), which is mainly motivated in the extraordinarily rapid advances in neural recording technologies, now capable of capturing hundreds, even thousands, of simultaneously recorded neurons (Stevenson and Kording, 2011; Stringer et al., 2019). Capturing whole nervous systems of even moderately complex animal models will require scaling the number of cells recorded together by further orders of magnitude (Lemon et al., 2015). And this is really the most evident advantage of network science: these tools have been developed to address social and technological networks of millions of nodes or more, so can easily scale to systems neuroscience problems.

On the other hand, systems neuroscience poses new challenges for network science. Most studies in network science target data that is static or slowly changing over time. Neural populations, instead, have intrinsic nonstationary dynamics, which change rapidly compared to the temporal resolution of neural recordings. Moreover, systems neuroscience analysis requires not only to quantitatively compare networks within and across brain regions and animals, but also across experimental conditions—stimuli, decisions, and other external variables. The manifold learning approach, discussed in chapter 5 of this thesis, might be helpful to tackle this problem as it focuses on extracting the dynamics of a network rather than its structure. Bringing these two approaches together to tackle the issues raised by system neuroscience has the potential to be fruitful and bear novel insights.

In the next chapter I will employ this framework to track changes in the co-firing relationship between pyramidal cells in the dCA1 network as new information is integrated in the pre-existing mnemonical network. In this way, I will uncover a mechanism of memory encoding an updating within the hippocampal network, and the potential cellular substrate that enables it.

Chapter 4

Integrating new memories in the hippocampal network activity space

The work presented in this chapter is published as:

Giuseppe P. Gava, Stephen B. McHugh, Laura Lefévre, Vitor Lopes-dos-Santos, Stephanie Trouche, Mohamady El-Gaby, Simon R. Schultz, and David Dupret (2021), *Integrating new memories into the hippocampal network activity space*, Nature Neuroscience, 24(3), 326–330.

I conceived and designed the study together with S. R. Schultz and D. Dupret. I analysed all the data, performed the analytical study and generated all figures. V. Lopes-dos-Santos developed the tetrode depth estimation algorithm. All animals recordings were performed by the members of the Dupret Lab, whom I am very thankful to.

4.1 Introduction

Assimilating new knowledge without corrupting previously acquired memories is a critical brain function. However, as reviewed in section 2.1, of this thesis, learning and memory interact: prior knowledge can proactively influence ongoing learning,

and new information can retroactively influence memories of past events (Dudai and Morris, 2013; D. L. Schacter et al., 2007). As detailed in chapter 2, the hippocampus is a brain region essential for learning and memory (Eichenbaum et al., 1999; Morris, 2006), yet the network-level operations that underlie the continuous integration of new experiences into memory, segregating them as discrete traces while enabling their interaction, are unknown. Different environments and contexts are represented by distinct combinations of neurons through a map-like representation, as seen in section (O'Keefe and Nadel, 1978; Wilson and McNaughton, 1994; E. I. Moser, M.-B. Moser, et al., 2017). While this suggests how the hippocampus disentangles the spatial contexts of different memories, these representations further involve the fine-grained temporal coordination of neuronal spiking that give rise to sets of jointly-active neurons that organize motifs of coactivity (co-firing patterns), some of which underpin spatially-selective assemblies (Buzsáki and Llinás, 2017; Kubie et al., 2020; O'Neill et al., 2008; Ven et al., 2016).

Here, by analysing the activity of principal cells with graph-theoretical techniques (Bassett and Sporns, 2017; Humphries, 2018), we first found that new associative learning modifies the topology of the cells' co firing patterns representing the unrelated familiar environment, strengthening their spatial information content. We further observed that these neuronal co firing graphs evolved along three functional axes: the first identified novelty by segregating spatial contexts, the second distinguished ongoing behavioural events, and the third revealed cross-memory interaction. Finally, we found that during this process, high activity principal cells rapidly formed the core representation of each memory; whereas low activity principal cells gradually joined co-activation motifs throughout individual experiences, enabling cross-memory interactions. These findings reveal an organizational principle of brain networks where high and low activity cells are differently recruited into coactivity motifs as building blocks for flexible integration and interaction of memories.

4.2 Methods

4.2.1 Experimental procedure

Animals. Adult male C57BL/6J mice (Charles River Laboratories, UK) or transgenic heterozygous CamKIIa-Cre mice (Jackson Laboratories; CamKIIa-Cre B6.Cg-Tg(Camk2a-cre)T29-1Stl/J, stock number 005359, RRID: IMSR_JAX:005359; maintained on a C57BL/6J background) were used for these experiments. Mice were housed with their littermates until the surgical procedure with free access to food and water in a room with a 12/12h light/dark cycle, 19–23°C ambient temperature and 40–70% humidity. All mice were held in IVC's, with wooden chew stick and nestlets. Mice were 4-7 months old at the time of testing. Experimental procedures were performed on mice in accordance with the Animals (Scientific Procedures) Act, 1986 (United Kingdom), with final ethical review by the Animals in Science Regulation Unit of the UK Home Office.

Surgical procedure. Mice were implanted with a microdrive during a surgical procedure performed under deep anaesthesia using isoflurane (0.5–2 %) and oxygen (2 l/min), with analgesia (0.1 mg/kg vetergesic) provided before and after surgery. Microdrives contained 10–12 tetrodes, targeting the stratum pyramidale of the dorsal CA1 hippocampus (Ven et al., 2016). Tetrodes were constructed by twisting together four insulated tungsten wires ($12\mu m$ diameter, California Fine Wire) and heating them to fuse them into a single bundle. Each tetrode was attached to a M1.0 screw to enable their independent movement. The drive was implanted under stereotaxic control in reference to bregma (Ven et al., 2016). Tetrodes were initially implanted above the CA1 pyramidal layer and their exposed parts were covered with paraffin wax. The drive was then secured to the skull using dental cement and stainless-steel anchor screws inserted into the skull. Two of the

anchor screws, both above the cerebellum, were attached to a 50 µm tungsten wire (California Fine Wire) and served as ground. Tetrode placement was confirmed by the electrophysiological profile of the local field potentials in the hippocampal ripple frequency band and anatomical electrode tracks (Ven et al., 2016; Csicsvari, Hirase, A. S. Czurkó, et al., 1999). In one mouse, a single-shank silicon probe (Neuronexus, model A1x32-5mm-25-177-H32_21mm) was implanted following the same surgical procedure to span the somato-dendritic axis of dCA1 principal cells and establish the laminar profile of the sharp-wave/ripples (SWRs) detected in the local field potentials. These silicon probe recordings allowed estimating the position (depth) of individual tetrode-recorded principal cell soma (Fig. 4.3.2).

Recording procedure. After at least one-week post-operative recovery, mice were handled for 3-4 days and then daily familiarized to the experimental paradigm, including connection to the electrophysiological recording system and exploration of a circular-walled open-field enclosure (42 cm diameter; the familiar enclosure). Mice were food restricted (to 90% body weight) and the various experimental conditions were randomly allocated across mice and recording days. The 1-day CPP task included four sessions lasting 15 minutes each: pre-test, place conditioning to sucrose (+Suc.), to water (+Wat.) and test [23]. The enclosure consisted of two square-walled (46 cm × 46 cm × 38 cm) compartments with distinct inside building block configurations on each day. A bridge (8 cm length, 7 cm width) connected the two compartments during pre-test and CPP test. A linear locomotion assistant (Imetronic, Pessac, France) held the recording cable while sensing its movement using infrared light beam detectors, allowing the connected animal to move freely within and across compartments. During pre-test, mice explored the entire CPP enclosure and their baseline (spontaneous) preference for one of the two compartments was determined. Next, the bridge was removed for the conditioning sessions, and mice explored their non-preferred compartment containing drops of

20% sucrose diluted in water (2x10min sessions, 10x10μl drops per session). Next, mice explored their preferred compartment containing drops of water (2x10min sessions, 10x10μl drops per session). One hour later, CPP memory was tested by allowing the mice to explore the entire apparatus again (CPP test). We calculated a place preference score for each mouse during both pre-test and test sessions as the difference between the time spent in the compartment paired with sucrose minus the time spent in that one paired with water, during conditioning, over their sum. On the morning of each recording day, the local field potential (LFP) signals obtained from each tetrode was used to guide its optimal positioning within the dCA1 pyramidal layer in search of multi-unit spiking activity (Ven et al., 2016). Tetrodes were left in position for 1.5-2h before recordings started. On each day, ensemble recordings were performed continuously while mice explored the familiar circular-walled enclosure before and after ("exposure" and "re-exposure"; 15 minutes each) the CPP task. Mice were subjected to a novel CPP enclosure on each recording day (i.e., novel spatial configurations and wall cue cards). Three other behavioural tasks had a 6-session layout similar to that of the CPP task, in order to evaluate whether the topological deviations observed during CPP reflected a general network response for integrating new information. In these three tasks, each day contained 6 sessions that matched the timeline of the CPP task. Mice explored the familiar enclosure before (exposure) and one hour after (re-exposure) either: (i) four sessions of spatial exploration in a novel enclosure without reward (the *Novel context only* task; Extended Data Fig. 2a), (ii) four sessions testing spontaneous preference for one of two novel enclosures, following a similar protocol as for the CPP task but with no reward (the *Spontaneous Place Preference* task; Fig. 4.1.3c), or (iii) four sessions of spatial exploration in a second familiar enclosure with sucrose reward and water provided in the second and third session, respectively (the *Familiar context with reward* condition; Fig. 4.1.3f), as in the CPP task (Fig. 1a). A fifth task further allowed testing whether network topological deviations

occurred during repeated exploration of a familiar enclosure (the "Familiar context only" task; four exploration sessions in the same familiar enclosure on each day; Fig. 4.1.3h). On each recording day, mice were returned to their homecage between task sessions, having access to water and food while the experimenter prepared the open-field arena for the next session. Data collection could not be performed blind to the conditions of the experiments since the experimenter had to be aware as to which condition they had to expose each mouse on a given day (which behavioural task) and on a given session (which open-field arena). At the end of each day, tetrodes were raised to avoid possible mechanical damage overnight.

Multichannel data acquisition and position tracking. The extracellular signals from the electrodes were amplified, multiplexed, and digitized using a single integrated circuit located on the head of the animal (RHD2164, Intan Technologies; gain x1000). The amplified and filtered (0.09Hz to 7.60kHz) electrophysiological signals were digitized at 20kHz and saved to disk along with the synchronization signals from the position tracking. To track the location of the animal, three LED clusters were attached to the electrode casing and were captured at 25 frames per second by an overhead camera.

4.2.2 Neural activity and events detection

Spike detection and unit isolation. For the offline spike detection process, the recorded signals were first band-pass filtered (800 Hz to 5 kHz). Spikes were then detected using the power (root-mean-square) of the filtered signal calculated in 0.2-ms sliding windows. The detected spikes from each individual electrode were combined per tetrode. To isolate spikes belonging to the same neuron, spike waveforms were first up-sampled to 40 kHz and then aligned to their maximal trough (Csicsvari, Hirase, Czurko, et al., 1998). Principal component analysis was

applied to these waveforms in a window of ±0.5 ms from the trough to extract the first three or four principal components per channel, such that each individual spike was represented by 12 waveform parameters. An automatic clustering program (KlustaKwik, http://klusta-team.github.io) was run on this principal component space and the resulting clusters were manually recombined and further isolated based on cloud shape in the principal component space, cross-channels spike waveforms, auto-correlation histograms and cross-correlation histograms (Harris, Henze, et al., 2000; Kadir et al., 2014). All sessions recorded on the same day were concatenated and clustered together. Each cluster used for further analysis showed throughout the entire recording day stable cross-channels spike waveforms, a clear refractory period in its auto-correlation histogram, well-defined cluster boundaries and an absence of refractory period in its cross-correlation histograms with the other clusters. Hippocampal principal cells were identified by the shape of their auto-correlation histogram, their firing rate and their spike waveform (Csicsvari, Hirase, Czurko, et al., 1998). We further used an automated clustering pipeline using Kilosort (https://github.com/cortex-lab/KiloSort; Pachitariu et al., 2016) via the SpikeForest sorting framework (https://github.com/flatironinstitute/spikeforest, Magland et al., 2020). To apply KiloSort to data acquired using tetrodes, the algorithm was used tetrode-wise (i.e., templates were obtained from channels within a given tetrode bundle, while masking all other recording channels). The resulting clusters were manually curated to check all clusters and remove spurious units using metrics derived from the waveforms and spike times. This procedure was cross-validated using several datasets and verified against manual curation, by computing confusion matrices to validate that clusters obtained automatically were also obtained with the previous method. In total, this study includes n=3,483 principal cells from 63 recordings days: n=1,083 principal cells in the "Conditioned Place Preference" task (63.7±33.2 principal cells per day; 17 CPP 6-session days from 7 mice; 5 CamKIIa-Cre and 2 C57BL/6J; yielding 102 graphs; 260,058 co

firing pairs), n=585 principal cells in the "Novel context only" task (45.0±13.7 principal cells per day; 13 "Novel only" 6-session days from 5 mice; 3 CamKIIa-Cre and 2 C57BL/6J; yielding 78 graphs; 28,192 co firing pairs), n=640 principal cells in the "Spontaneous Place Preference" task (49.2±17.5 principal cells per day; 13 SPP 6-session days from 6 mice; 3 CamKIIa-Cre and 3 C57BL/6J; yielding 78 graphs; 34,838 co firing pairs), n=517 principal cells in the "Familiar context with reward" task (57.4±12.2 principal cells per day; 9 "Familiar with reward" 6-session days from 3 mice; 2 CamKIIa-Cre and 1 C57BL/6J; yielding 54 graphs; 30,512 co firing pairs) and n=658 principal cells in the "Familiar context only" task (59.3±15.8 principal cells per day; 11 "Familiar only" 4-session days from 3 mice; 2 CamKIIa-Cre and 1 C57BL/6J; yielding 44 graphs; 40,744 co firing pairs).

Sharp-wave/ripples (SWRs) detection. Local field potentials (LFPs) of each pyramidal CA1 channel (for tetrode recordings) or recording site (for linear silicon probe recordings) were subtracted by the mean across all channels/sites (common average reference). These re-referenced signals were then filtered for the ripple band (110 to 250 Hz; 4th order Butterworth filter) and their envelopes (instantaneous amplitudes) were computed by means of the Hilbert transform. The peaks (local maxima) of the ripple band envelope signals above a threshold (5 times the median of the envelope values of that channel) were regarded as candidate events. Further, the onset and offset of each event were determined as the time points at which the ripple envelope decayed below half of the detection threshold. Candidate events passing the following criteria were determined as SWR events: (i) ripple band power in the event channel was at least 2 times the ripple band power in the common average reference (to eliminate common high frequency noise); (ii) an event had at least four ripple cycles (to eliminate events that were too brief); (iii) ripple band power was at least 2 times higher than the supra-ripple band defined as 200-500 Hz (to eliminate high frequency noise, not spectrally compact at the ripple band, such as

spike leakage artefacts). We classified tetrodes as being in the deep or superficial sublayer of the CA1 pyramidal layer based on the mean peak amplitude of detected SWRs (Fig. 4.3.2). Positive values indicated that the tetrode was in the deep sublayer (i.e. closest to stratum oriens) while negative values indicated tetrode was in the superficial sublayer (i.e. closest to stratum radiatum) (Mizuseki, Diba, et al., 2011; Oliva et al., 2016; Csicsvari, Hirase, A. Czurkó, et al., 1999). SWRs were also used as time bins to calculate SWR firing response of low and high activity cells (Fig. 4.3.6e,f).

4.2.3 Graph-theoretical analysis of principal cells co-firing

We constructed weighted graphs that represent the spike relationships between dCA1 principal cells recorded in a given task session, calculating for that session the set of pairwise Pearson correlation coefficients between all pairs of spike trains. These co-firing graphs were computed using time bins during active exploratory behavior (with speed $>$ 2cm/s), discarding periods of immobility and further excluding sharp-wave/ripples (SWRs) in each task session. The recorded neurons (and their co-firing associations) are therefore the nodes (and their edges) in the co-firing graph of each task event, defined by their respective adjacency matrices (see eq. 3.1). As detailed in section 3.1, to compute each co-firing association value we used a bin-less approach by convolving the spike trains of i and j with a Gaussian kernel (SD=20ms) and then calculating their correlation coefficient r (thus, $-1 < r < 1$). As a result, A is symmetric, $w_{ij} = w_{ji}$, and the graph is undirected and fully connected (with no self-connections).

Clustering coefficient. We computed a clustering coefficient to characterize the local synchronization of network activity by quantifying the number of three-node motifs, as described in section 3.1.3. In each graph, for any neuron i, we obtained its clustering coefficient C_i using eq. 3.7 (Onnela et al., 2005; Saramäki et al., 2007;

Costantini and Perugini, 2014). Note that in this way negative edges are taken into account, as an odd number of negative edges in a triad leads to a negative contribution.

Geodesic path length. We measured the geodesic (i.e., shortest) path length to estimate the coordination efficacy between the activity of any two nodes in the graph. Here, as detailed in section 3.1.2, we embedded each weighted graph in a lattice and defined the length between two nodes i and j as in eq. 3.3, discarding all negative edges. We then identified the shortest path length L_ij between any two nodes in the graph using the Floyd-Warshall algorithm (Floyd, 1962; Warshall, 1962; Roy, 1959); to finally yield one average value per neuron as in eq. 3.4.

Single-neuron cumulative co-firing strength. We defined the single-neuron cumulative co-firing strength as the total pairwise activity correlation strength of a given node in a weighted graph. As already presented in section 3.1.1, the strength S_i of a node i is the sum of all the weights w_{ij} of the edges projected from that node (eq. 3.2).

4.2.4 Spatial rate map and spiking activity analyses

We divided the horizontal plane of the recording enclosures into spatial bins of approximately 2×2 cm to generate the spike count map (number of spikes fired in each bin) for each neuron and the occupancy map (time spent by the animal in each spatial bin) in each task session. All maps were then smoothed by convolution with a two-dimensional Gaussian kernel having a standard deviation equal to two bin widths. Finally, spatial rate maps were generated by normalizing the smoothed spike count maps by the smoothed occupancy map. The single-neuron map similarity was calculated by the 2D Pearson correlation coefficient between the place maps of a given neuron across two task sessions. Here, this task session

pairwise measure compares for each neuron the spatial relationship between its place map in the exposure session and that computed for another task session. For the pre-test and test sessions, two place maps were extracted (one per arena) and the single-neuron map similarity was obtained taking the maximum similarity value between either of the two CPP sessions' maps and that of the exposure session. The population map similarity (O'Neill et al., 2008; Dupret et al., 2010; McNamara et al., 2014) compares the spatial relationships of the set of place maps computed for one task session with those from another task session. Here, this task session pairwise measure represents the extent to which sets of cells that fired in similar regions of space (that is, overlapping place fields) during the exposure session still fire together in similar regions of space later during another task session. For this measure, we used cells with a spatial coherence value (see below) above 0.2 during the exposure session. The population map similarity was calculated by first computing the place field similarity (PFS) value for each cell pair during the exposure session as the Pearson correlation coefficient from the direct binwise comparisons between the spatial rate maps of the two cells, limited to valid bins (occupancy greater than zero). This procedure yields a vector storing the PFS values for all cell pairs during the exposure session. We repeated this procedure to obtain the PFS vectors of the other task sessions. Finally, the population map similarity between two task sessions was calculated as the Pearson correlation coefficient between the PFS vector of the exposure session versus the PFS vector of the chosen comparison session.

Spatial coherence. To measure the spatial coherence (i.e. the similarity of a cell's firing rate over spatial bins), we computed a boxcar-averaged version of its unsmoothed spatial rate map, with each bin replaced by the arithmetic mean of itself and its eight adjacent neighbours. The smoothed spatial rate map was then correlated to its unsmoothed version to yield a Pearson correlation value (Zhang

et al., 2014).

Spatial information. To estimate the amount of spatial information conveyed by the spike train of a given cell, we used the mutual information measure $I(R;S)$, defined in equation 2.3 and discussed in section 2.3.5 (Butts, 2003; Cover and Thomas, 2006; Shannon and Weaver, 1949). This was corrected for the estimation bias by subtracting an analytical estimate of the bias itself (Panzeri and Treves, 1996).

Bursting index. For the spike train of each neuron, we defined spike bursts as transient packets of spikes with inter-spike intervals less than 6ms (Harris, Hirase, et al., 2001; Ranck, 1973). We used the inter-spike interval t versus inter-spike interval $t+1$ plot to identify the first, mid and last spikes of each burst candidate. The bursting index was then defined by the ratio of bursting spikes out of all the spikes fired by the neuron.

4.2.5 Across-graph topological distance analyses

Co-firing graphs have symmetric and positive semi-definite adjacency matrices since their elements are computed using the Pearson correlation coefficient between pairs of spike-trains. Thus, their topologies lie on a Riemannian manifold, as discussed in chapter 3, section 3.3, and the geodesic distance between them is the most accurate measure of their dissimilarity (Pennec et al., 2006; Moakher, 2005; Venkatesh et al., 2020). Accordingly, we employed the log-Euclidean metric (Arsigny et al., 2006), detailed in eq. 3.10, to compute the topological distance between constellations of co-firing patterns for pairs of task session graphs. This way, we obtained for each task session s (from exposure to re-exposure) a vector of six topological distances D^s separating the co firing graph of that session to the co firing graph of each of the other five task sessions, as well as to itself (by adding one SD of white noise

to avoid exact 0 results). We normalized each of these vectors by their maximum distance value, to compare them across days. We thus obtained a 6 x 6 matrix of the topological distances between the co firing graphs of the six task sessions for each recording day. Dimensionality reduction, primarily PCA but also MDS and ICA, was used to visualize the topological distances separating all co-firing graphs in the activity space of the hippocampal network. To do so, we stacked all topological distances vectors in a 6 x N matrix, where N is the total number of co-firing graphs ($N = n_d \times n_s$, one graph per task session, n_s, per recording day, n_d). We next used PCA on the recordings with more than 40 principal cells to obtain the set of principal components that indicate trajectories in the network activity space along which co-firing graphs evolved from exposure to re-exposure task sessions. We then projected the first principal components that explained 80% of the variance in co-firing patterns onto the topological distances separating the co-firing graphs of all recordings from a given task.

High and low activity cells contribution to network co-firing patterns. For each task session s, we quantified the contributions C_G^s of the high and low activity sub networks G to network-level co-firing patterns by computing the Euclidean distance R_G^s between the six-dimensional topological distance vector representing the entire network D^s and those representing the two sub-networks D_G^s (see section above):

$$R_G^s = Euclidean(D^s, D_G^s); \qquad C_G^s = 1 - R_G^s$$

4.2.6 Data and statistical analyses

Data were analysed in Python 3.6 and using the packages DABEST v0.3.048, scikit-learn v0.23.249 (Pedregosa et al., 2011), NetworkX v2.450 (Hagberg et al., 2008), pyentropy v0.5.051 (Ince et al., 2009), Numpy v1.18.1, Scipy v1.4.1, Matplotlib v3.1.2, Pandas v0.25.3 and Seaborn v0.11.0. All statistical tests related to a symmetric distribution were performed two-sided using Gardner-Altman plots (to compare 2 groups) and Cumming plots (for more groups) from the Data Analysis with Bootstrap-coupled ESTimation (DABEST) framework (Ho et al., 2019). These DABEST estimation plots (Cumming's or Gardner-Altman's) allow visualizing the effect size by plotting the data together with the mean or median difference between one of the groups (the left-most group of each plot/dataset, used as group-reference) and the other groups (to the right, along the x-axis of each plot). For each estimation plot: (i) the upper panel shows the distribution of raw data points for the entire dataset together with the mean (gap) and ± STD of each group (vertical ends) as gapped lines; and (ii) the lower panel displays the difference between a given group and the (left-most) group-reference, computed from 5,000 bootstrapped resamples and with difference-axis origin aligned to the mean or the median of the group-reference distribution. For each estimation plot: black-dot, mean (for normal distributions) or median (for skewed distributions) as indicated; black-ticks, 95% or 99% confidence interval as indicated; filled-curve: bootstrapped sampling-error distribution. Such visualisation of difference statistics is considered sufficient and therefore no p-values are reported in the main text (Ho et al., 2019). Data distributions were assumed to be normal but this was not formally tested. We also used the t-test to compare two conditions; the Wald test for assessing the significance of regression lines; and the Kolmogorov–Smirnov test for comparing probability distributions. No statistical methods were used to pre-determine sample sizes but our sample sizes are similar to those reported in

previous publications (e.g., O'Neill et al., 2008, Danielson et al., 2016, Oliva et al., 2016, McKenzie, A. J. Frank, et al., 2014). Neural and behavioural data analyses were conducted in an identical way regardless of the identity of the experimental condition from which the data were collected, with the investigator blind to group allocation during data collection and/or analysis.

4.3 Results

We monitored dorsal CA1 (dCA1) ensembles from mice exploring a familiar environment before and after associating a novel environment with reward (sucrose), using a 1-day conditioned place preference (CPP) task (Fig. 4.1.1a and Fig. 4.1.2a). On each day of this paradigm, mice first explored the familiar enclosure (exposure). Next, we identified the preference of each mouse for one of the two novel compartments connected by a bridge to form the CPP enclosure that day (pre-test). We subsequently removed that bridge in conditioning sessions where each mouse explored its non-preferred compartment baited with drops of a sucrose solution (+Suc.); and then the preferred compartment with drops of water (+Wat.). One hour after the last conditioning session, we re-inserted the bridge and tested the place preference memory (CPP test; Extended Data Fig. 1b). To assess the effect of new CPP memory on prior representations, we finished each recording day by re-exposing mice to the familiar enclosure (re-exposure). See the Methods section for a more in depth description of the experimental protocols.

4.3.1 The topology of hippocampal co-firing is modified by the encoding of novel memories

On each day we recorded neuronal spiking throughout the six CPP task sessions (Fig. 1a; n=1,083 total principal cells; 63.7±33.2 principal cells per day; 17 days from 7

mice; Trouche, Koren, et al., 2019). Using the spike trains recorded during active exploration (i.e. excluding immobility epochs and sharp-wave/ripples), we computed weighted graphs (Bassett and Sporns, 2017; Humphries, 2018) to represent the firing relationships between sets of coactive neurons in each task session (Fig. 4.1.1b-e; n=102 graphs; 260,058 co firing pairs). In these co firing graphs, each node represents one neuron; the edge linking any two nodes represents the coactivity of that cell pair, with a weight computed as the Pearson correlation coefficient between their spike trains. For each graph, this procedure yielded an adjacency matrix of pairwise co-firing coefficients, with dimensions equal to the number of neurons (Fig. 4.1.1c and Fig. 4.1.2c).

We observed that the co-firing graphs featured more triads of coactive neurons during CPP learning (Fig. 4.1.1f; Clustering coefficient), showing that associating a novel place with reward changes the coactivation structure of the network. Concomitantly, the average geodesic path length, calculated as the mean shortest path between any two nodes, decreases (Fig. 4.1.1f; Geodesic path length), indicating greater functional connectivity between sets of coactive neurons. By calculating for each node, the summed weight of all its edges in the adjacency matrix, we also found that the average single-neuron cumulative co-firing increases (Fig. 4.1.1f; Co-firing strength), reporting heightened firing associations among neurons during CPP learning. Similar topological deviations are observed in the co-firing network under related conditions: exploration of a novel context without reward ("*Novel context only*" task), spontaneous preference for a novel place ("*Spontaneous Place Preference*" task, also referred to as *SPP*) and reward experience in an otherwise familiar context ("*Familiar context with reward experience*" task) (4.1.3a-g). To ensure that such topological deviations are not due only to the passing of time, we let the animals explore over multiple sessions the same familiar environment ("*Familiar context only*" task) and no change in the co-firing was observed (4.1.3h). These findings suggest a potential general mechanism for the integration of new information.

Importantly however, these topological deviations did not reset during re-exposure one hour after CPP (Fig. 4.1.1f) while they did in the other tasks (4.1.3). These sustained changes following CPP neither reflected differences in exploration and behavioural patterns (Fig. 4.1.4a-f) nor mere fluctuations in the co-firing (4.1.4g). Thus, the mnemonic operation of updating a recently-encountered place with reward caused an enduring topological reorganisation ("hysteresis") in the coactivity structure of the network.

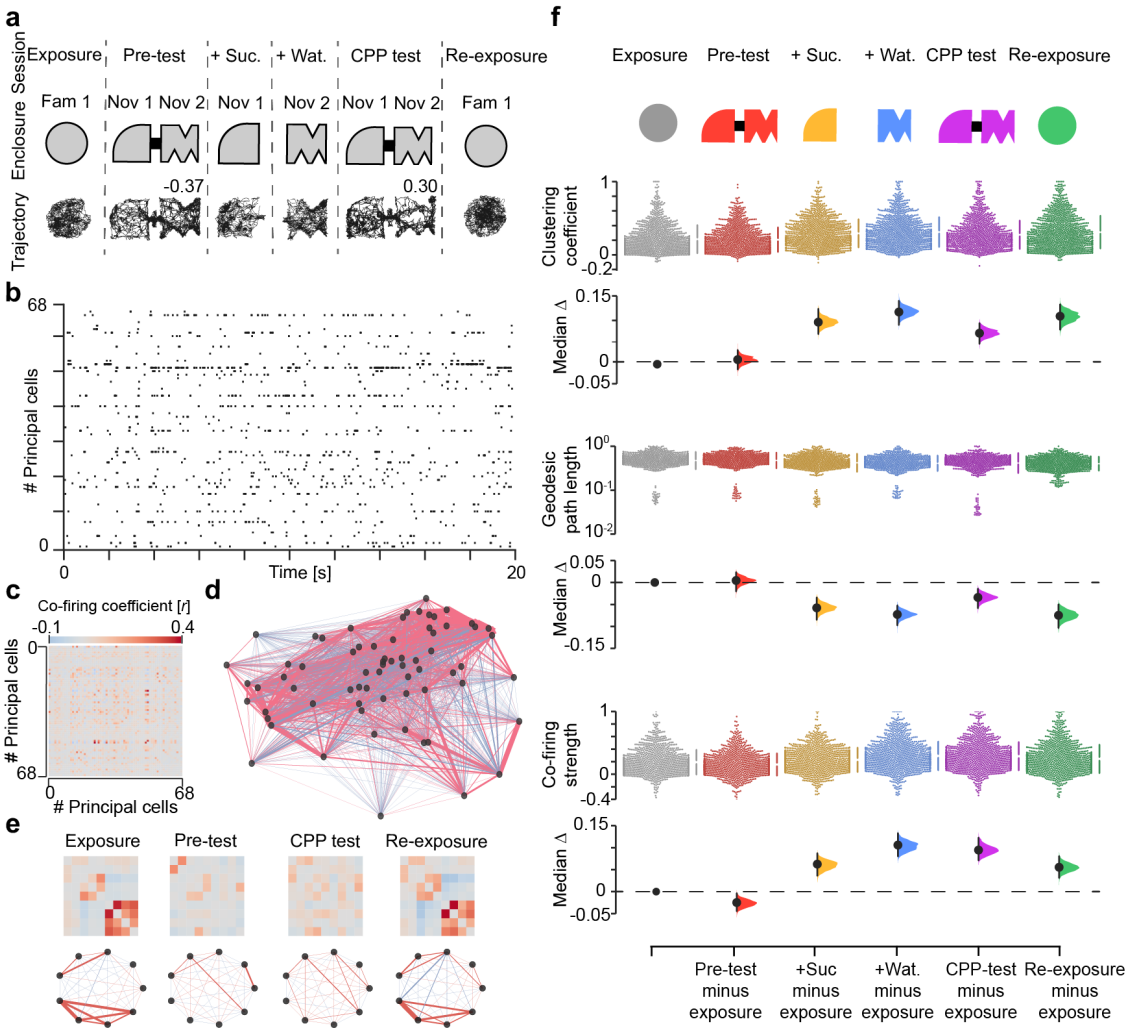

Figure 4.1.1: New CPP memory reorganizes pre-existing hippocampal co-firing topology. **a**, CPP task layout. Each day, mice explored the same familiar enclosure before and after a four-session CPP task. Mouse trajectory in each session from 1 d is shown below the schematic of in-use enclosures. Numbers indicate place preference scores for pre-test and test, as the time in sucrose-paired compartment (+Suc.) minus that in water-paired compartment (+Wat.) over the sum. During the CPP test, the mouse successfully changed its initial preference for the sucrose-paired compartment, as indicated by the positive score. **b**, Example raster plot showing the spike trains of 68 simultaneously recorded dCA1 principal cells (one cell per row) for the day shown in **a**. For clarity, a 20-s sample is shown. **c**, The corresponding adjacency matrix of the pairwise correlation coefficients measuring the co-firing of principal cells. **d**, The corresponding co-firing graph. Each node represents one cell. Each edge represents the co-firing association of one cell pair, color-coded according to their correlation's sign and width proportional to the edge's absolute value. **e**, Example adjacency matrices (top row) and corresponding neuronal motifs (bottom row) extracted from the graph shown in **d** to visualize some co-firing changes across sessions. **f**, Changes in topological clustering (top), geodesic path length (middle) and single-neuron cumulative co-firing strength (bottom) of co-firing graphs. For each measure, the entire dataset is presented using a Cumming estimation plot to visualize the effect size; bottom panels: black dot, median; black ticks, 99% confidence interval; filled curve: sampling error

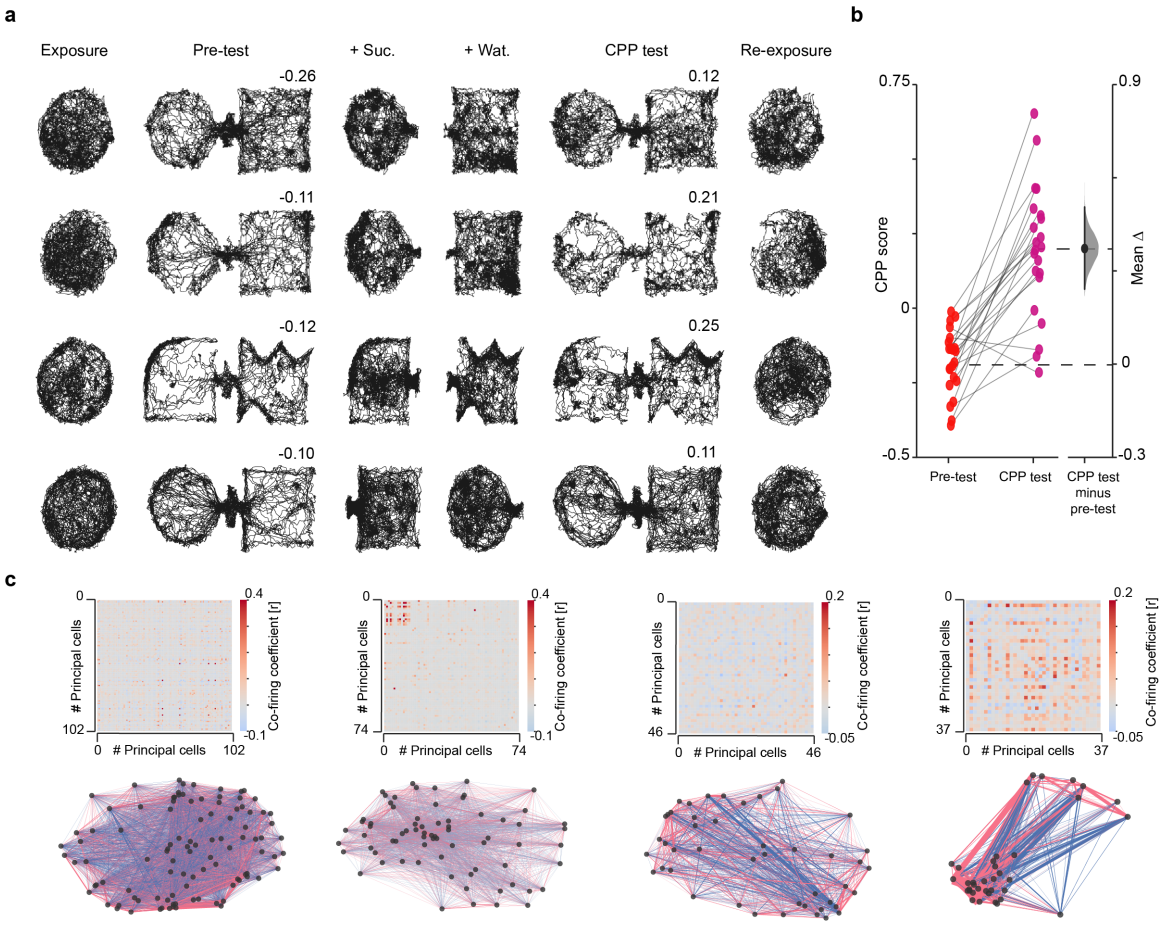

Figure 4.1.2: Behavioural performance and hippocampal co-firing graphs in the CPP task. **a**, Additional example trajectories for four mice. Each day (one day per row), mice explored the same (circular-walled) familiar enclosure before (exposure) and after (re-exposure) a 1-day 4-session CPP task (Fig. 4.1.1a). The CPP apparatus was formed by two novel compartments on each day. Numbers indicate place preference scores for pre-test and CPP test sessions, as the time in sucrose-paired compartment (+Suc.) minus that in water-paired compartment (+Wat.) divided by the sum. **b**, Place preference scores. A negative score indicates that mice spent less time in the compartment paired with sucrose during conditioning. Note that during CPP test, mice successfully changed their preference for the compartment recently paired with sucrose, as indicated by the positive score. Scores are presented using a Gardner-Altman estimation plot to visualise the effect size. The left panel shows the distribution of raw data points for the pre-test and test sessions. The right panel displays the difference between CPP test and pre-test, computed from 5,000 bootstrapped resamples and with difference-axis origin aligned to the mean of the pre-test session distribution. Black-dot, mean difference; black-ticks, 99% confidence interval; gray-filled-curve: sampling-error distribution. **c**, The adjacency matrices (top row) of the pairwise correlation coefficients measuring principal cells' co-firing for days shown in (**a**), with the corresponding co-firing graphs (bottom row). Each node represents one principal cell. Each edge represents the co-firing association of one cell pair, color-coded according to their correlation's sign and width proportional to the edge's absolute value.

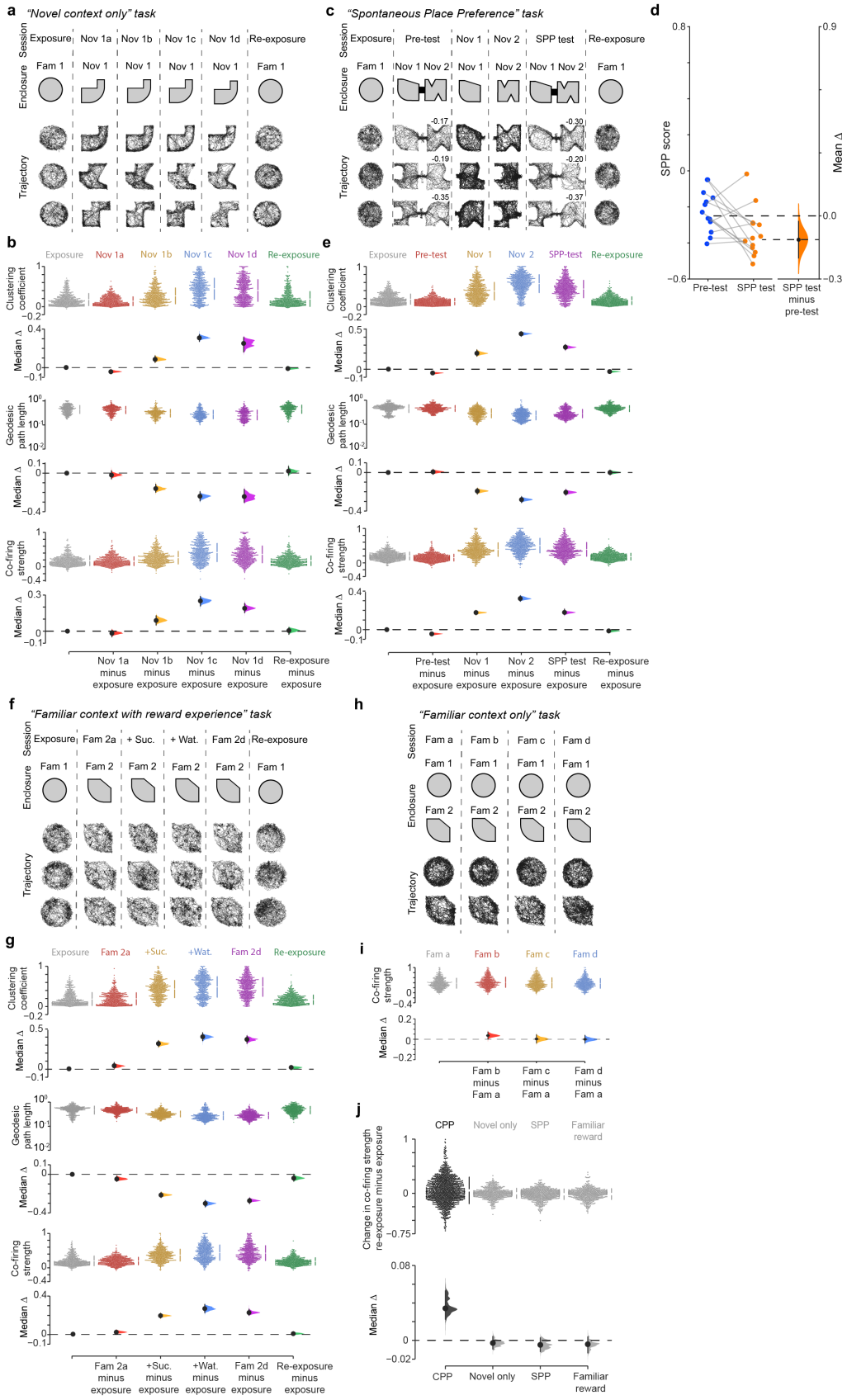
a
"Novel context only" task
Session
Exposure
Nov 1a
Nov 1b
Nov 1c
Nov 1d
Re-exposure
Enclosure
Fam 1
Nov 1
Trajectory
b
Clustering coefficient
Median Δ
Geodesic path length
Co-firing strength
Nov 1a minus exposure
Nov 1b minus exposure
Nov 1c minus exposure
Nov 1d minus exposure
Re-exposure minus exposure
c
"Spontaneous Place Preference" task
Pre-test
Nov 1
Nov 2
SPP test
Nov 1 Nov 2
-0.17
-0.19
-0.35
-0.30
-0.20
-0.37
e
Pre-test minus exposure
Nov 1 minus exposure
Nov 2 minus exposure
SPP test minus exposure
Re-exposure minus exposure
d
SPP score
Mean Δ
Pre-test
SPP test
SPP test minus pre-test
f
"Familiar context with reward experience" task
Fam 2a
+ Suc.
+ Wat.
Fam 2d
Fam 2
g
+Suc.
+Wat.
Fam 2a minus exposure
+Suc. minus exposure
+Wat. minus exposure
Fam 2d minus exposure
Re-exposure minus exposure
h
"Familiar context only" task
Fam a
Fam b
Fam c
Fam d
i
Fam b minus Fam a
Fam c minus Fam a
Fam d minus Fam a
j
CPP
Novel only
SPP
Familiar reward
Change in co-firing strength re-exposure minus exposure

Figure 4.1.3: Graph topology during exploration of a novel enclosure, spontaneous novel place preference and exploration of a familiar enclosure with or without reward. **a,b**, "Novel context only" task. Behavioural protocol (**a**) and topology of hippocampal co-firing graphs (**b**) for unrewarded exploration of a novel enclosure (n = 585 total principal cells; 45.0±13.7 principal cells per day; 13 days from 5 mice yielding n=78 graphs; 28,192 co-firing pairs). Each day, mice explored the familiar enclosure before (exposure) and after (re-exposure) exploring a novel enclosure over four sessions, without sucrose reward. The session timeline matches that of the CPP task. (**a**) An example mouse trajectory for each session is shown for one day below the schematic of in-use enclosures. Additional examples shown below for two other days (one day per row). (**b**) The topological changes in clustering (top), geodesic path length (middle) and single-neuron cumulative co-firing strength (bottom) of co-firing graphs. For each measure, the entire "Novel context only" dataset is presented using a Cumming estimation plot to visualize the effect size. Note that exploring a novel context causes topological deviations from the co-firing graph that had featured exposure, indicating that the hippocampal network "learns" about the novel spatial layout. These deviations no longer occurred during re-exposure. **c-e**, "Spontaneous Place Preference" (SPP) task. Behavioural protocol (**c**) and performance (**d**) along with the graph topology (**e**). Each day, mice explored the familiar arena before (exposure) and after (re-exposure) exploring a CPP-like apparatus formed by two novel compartments (Nov 1 and Nov 2) connected by a bridge (pre-test). After having identified the preference of each mouse for one of the two novel compartments, the bridge was removed and each mouse first explored its non-preferred compartment (Nov 1), and then its preferred compartment (Nov 2), as in the CPP task but with no rewards. One hour after, the bridge was inserted back to test the animal's place preference (SPP test). The session timeline matches that of the CPP task. **c**, Example mouse trajectories as in (**a**). Numbers indicate place preference scores for pre-test and SPP test, as the time in the non-preferred compartment minus that in the preferred compartment over the sum. Note that mice did not changed their preference, as indicated by the negative scores. **d**, The scores are presented using a Gardner-Altman estimation plot (as in Fig. 4.1.2b). Note that co-firing topology also deviates during SPP sessions from that featuring exposure returns to baseline in the re-exposure. **f,g**, "Familiar context with reward" task. Behavioural protocol (**f**) and graph topology (**g**). Each day, mice explored the first familiar arena before (exposure) and after (re-exposure) exploring a second familiar enclosure during four sessions. The timeline matches that of the CPP task. Drops of sucrose (+Suc.) and water (+Wat.) were provided during Fam 2b and Fam 2c sessions, respectively. Example mouse trajectories from three days (**f**) shown as in (**a**). **g**, Similar to the unrewarded exploration of novel enclosures and the SPP task (**b,e**), co-firing topology deviated during exploration of the second familiar arena when paired with reward but returned to baseline in the re-exposure. **h,i**, "Familiar context only" task. Behavioural protocol (**h**) and network topology measured by co-firing strength (**i**) during exploration of a familiar enclosure without reward. Each day, mice explored a familiar enclosure (Fam 1 or Fam 2) over four sessions, to match the four sessions used between exposure and re-exposure in the other tasks (Fig. 4.1.1a and Fig. 4.1.1a–g). **h**, Example mouse trajectories shown as in (**a**). **i**, Co-firing strength did not deviate during repeated familiar explorations. **j**, Topological changes between exposure and re-exposure are compared across tasks. Note the sustained deviations (topological "hysteresis") following CPP. For each Cumming estimation plot, bottom panels: black dot, median; black ticks, 99% confidence interval; filled curve: sampling error

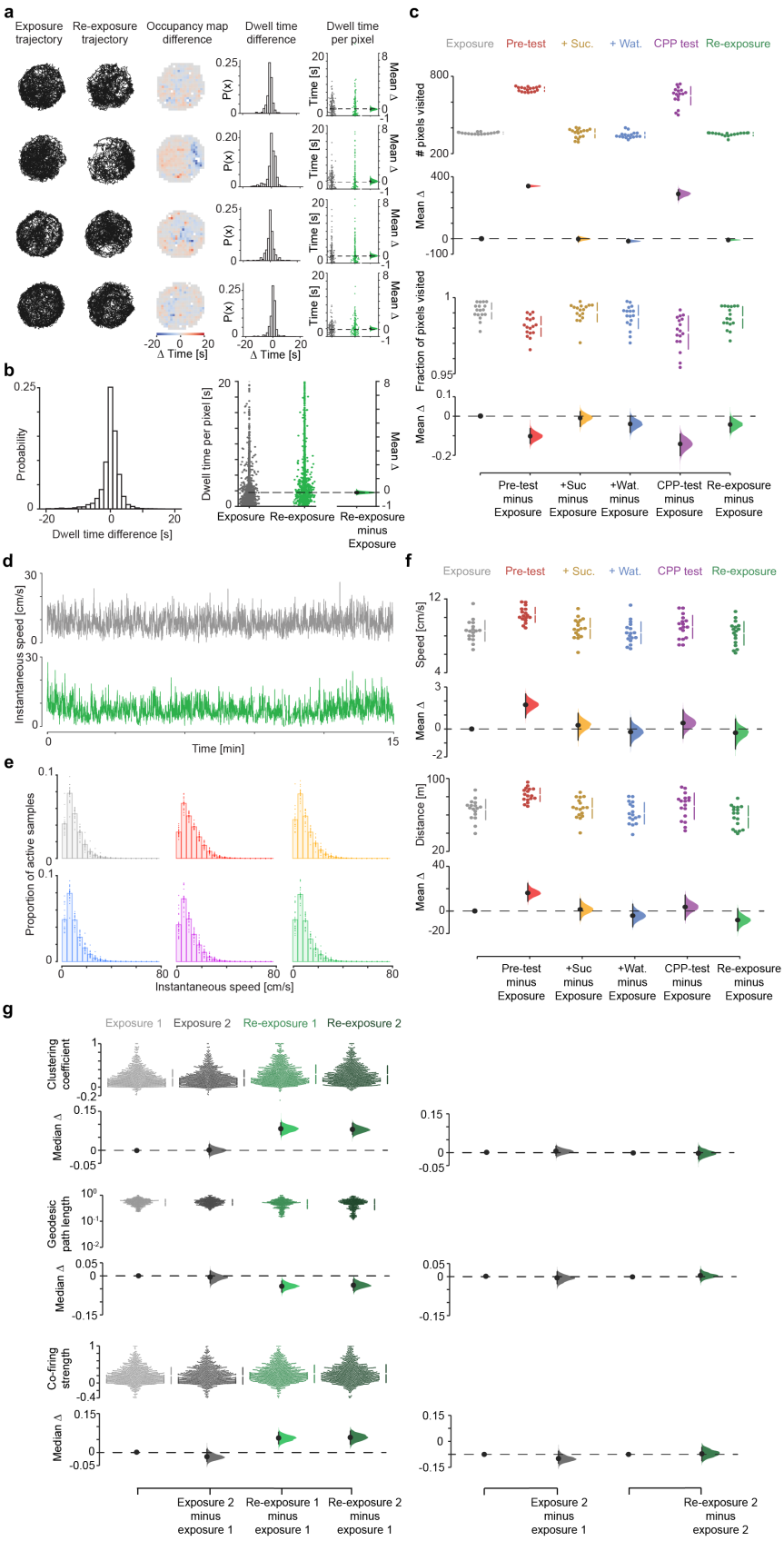
a
Exposure trajectory
Re-exposure trajectory
Occupancy map difference
Dwell time difference
Dwell time per pixel
P(x)
Time [s]
Mean Δ
Δ Time [s]
b
Probability
Dwell time difference [s]
Dwell time per pixel [s]
Exposure
Re-exposure
Re-exposure minus Exposure
c
Exposure
Pre-test
+ Suc.
+ Wat.
CPP test
Re-exposure
pixels visited
Mean Δ
Fraction of pixels visited
Pre-test minus Exposure
+Suc minus Exposure
+Wat. minus Exposure
CPP-test minus Exposure
Re-exposure minus Exposure
d
Instantaneous speed [cm/s]
Time [min]
e
Proportion of active samples
Instantaneous speed [cm/s]
f
Speed [cm/s]
Distance [m]
g
Exposure 1
Exposure 2
Re-exposure 1
Re-exposure 2
Clustering coefficient
Geodesic path length
Co-firing strength
Median Δ
Exposure 2 minus exposure 1
Re-exposure 1 minus exposure 1
Re-exposure 2 minus exposure 1
Re-exposure 2 minus exposure 2

Figure 4.1.4: Topological changes between exposure and re-exposure in the cPP task do not relate to differences in spatial exploration or mere fluctuations in co-firing. **a**, Spatial occupancy during exposure and re-exposure for example CPP days from four mice (one mouse day per row; using examples shown in Fig 4.1.1 1). Shown for each day, from left to right: (i) animal's trajectory for each familiar session, (ii) map of pixel-wise dwell time difference across the two sessions (for each pixel, the time spent in that pixel during exposure minus re-exposure), (iii) distribution of pixel-wise dwell time differences for all pixels covering the familiar enclosure, showing no significant difference of the mean from 0 (all Ps>0.05), and (iv) corresponding Gardner-Altman estimation plot to visualize the effect size of the pixel-wise dwell time difference across the two sessions. For each Gardner-Altman plot: left panels show the raw data points for exposure (grey) and re-exposure (green), with each point representing the dwell time in a given pixel; right panel: mean (black-dot), 95% confidence interval (black-ticks) and sampling-error distribution (filled-curve) of the difference between re-exposure and exposure, computed from 5,000 bootstrapped resamples and with the difference-axis (dashed-line) origin aligned to the mean of the exposure distribution. **b**, Pixel-wise dwell time difference in spatial occupancy across the two sessions for all CPP days, as in (**a**). Average time difference distribution (left) not significantly different from 0 (1-sample t-test, p=0.53, t=0.62, df=1461; in sec per spatial bin: mean difference=0.05±0.08; 95% confidence interval=[0.106, -0.205]; interquartile range=[1.306, -0.870]), as also shown in the corresponding Gardner-Altman plot (right). **c**, Cumming estimation plots showing the absolute number of pixels visited in each CPP task session (top; each dot representing one mouse CPP day) and the fraction of visited pixels in each enclosure (bottom). Note that the animal's coverage was not significantly different between exposure and re-exposure. The higher number of pixels visited during pre-test and CPP test merely reflects the higher dimension of the whole-CPP apparatus. **d**, Example time course of a mouse instantaneous speed during exposure (top) and re-exposure (bottom) in one CPP day. **e**, Instantaneous speed across the six sessions for all CPP days (bar charts: mean±SEM; with each superimposed dot representing one mouse CPP day). No significant differences across sessions with respect to exposure (P values: pre-text=0.25; +Suc.=0.38; +Wat.=0.76; CPP test=0.82; Re-exposure=0.98; all 2-sample Kolmogorov-Smirnov tests). **f**, Average speed across the six CPP task sessions (top) along with the total distance travelled (bottom; calculated for the first 15 min of each session). Note that the significant increased speed and distance travelled during pre-test (when the mouse is exposed for the first time to the novel CPP apparatus) do not translate in topological differences (Fig. 4.1.1f). These analyses (**a-f**) show that the topological hysteresis during re-exposure compared to exposure (Fig. 4.1.1f) does not reflect non-specific changes in spatial exploration. **g**, Topology alterations of hippocampal graphs in re-exposure (Fig. 4.1.1f) do not reflect mere fluctuations in co-firing. To control for natural variations in co-firing graphs, we split both exposure and re-exposure in two sections (1 and 2) with equal duration of active exploration (speed¿2 cm/sec; exposure: 6.89±0.13 versus 6.97±0.10 min; re-exposure: 6.99±0.30 versus 6.85±0.31 min, all Ps>0.05; Wilcoxon signed-rank test) and quantified topological changes across. As for all topological analyses, sharp-wave/ripples were excluded (though their occurrence did not differ between exposure and re-exposure; t=-1.55, p=0.14, paired t-test). For each Cumming estimation plot: black-dot, median; black-ticks, 95% confidence interval; filled-curve: bootstrapped sampling-error distribution.

4.3.2 Mnemonic information is encoded along multiple axes in the network co-firing space

We next asked whether the topological hysteresis caused by associative learning on the co-firing motifs expressed in the familiar enclosure (Fig. 4.1.1f) affected its spatial representation. By computing the firing maps of individual neurons in each task session (Fig.4.2.1a), we found that both single-neuron and population-level maps featuring exposure reorganized in the CPP enclosure, as expected from the remapping hypothesis of the hippocampus spatial code (e.g., Muller et al., 1987; Wilson and McNaughton, 1993; S. Leutgeb et al., 2004; Colgin et al., 2008; Wills et al., 2005), to then largely re-emerge during re-exposure (Fig. 4.2.2a,b). Yet, despite their reinstatement during re-exposure after CPP, familiar maps seemed edited beyond mere fluctuations in neuronal activity (Fig. 4.2.2c-e). Likewise, in the other tasks (Fig. 4.1.3) a complete reinstatement of the familiar map was not observed, suggesting a potential time-related fluctuation, but the amplitude of the mismatch was significantly smaller than the one reported in the CPP task (Fig. 4.2.2h).

These results indicate that new CPP memory re-structured the prior representation of the familiar environment. To further investigate the nature of this cross-talk, we quantified the variation of co-firing graphs within the "network activity space". We computed the topological distances separating graphs across the six CPP task-sessions (Fig. 4.1.1a), using the Riemannian Log-Euclidean metric (Arsigny et al., 2006; Pennec et al., 2006). For the co-firing adjacency matrix of each session, this procedure yielded a vector of distances to the adjacency matrices of the other sessions recorded that day (n=6 task-session pairwise distance vectors, together forming one 6x6 matrix each day; Fig. 4.2.1b and Fig. 4.2.3a). Principal component analysis of the distance matrices revealed three axes explaining 80% of the variance between

co-firing graphs across CPP task-sessions (Fig. 4.2.1c-e; see also Fig. 4.2.3b-e). Along the first principal component, the co-firing patterns of a given session overlapped with those of the other sessions in the same environment but not across (Fig. 4.2.1c-e), thus discriminating the familiar enclosure from the novel CPP apparatus and reporting the hippocampal remapping between these contexts (Fig. 4.2.2a-d). Coactivity along the second component disentangled the four distinct behavioural experiences within the CPP apparatus: the sessions in the two individual arenas (+Suc. and +Wat.) were projected on the opposite ends of the axis, encoding the difference between the two enclosures. The third component instead separated the sessions before from those after reward conditioning, notably separating the exposure and re-exposure sessions and thus reporting the topological hysteresis following CPP (Fig. 4.1.1f). These results held when considering separately the two CPP compartments during pre-test and CPP test, supporting the discrimination along the second component (Fig. 4.2.3f, g). We also used multidimensional scaling (MDS) and independent component analysis (ICA) to visualise the distance matrices and the same sessions layout was found (Fig. 4.2.3b, c). Moreover, using the Pearson correlation coefficient as a simpler, although potentially less accurate (see section 3.3), measure to gauge the similarity across co-firing graphs, revealed the same structure found with the Riemannian metric (Fig. 4.2.3d). Across CPP task-sessions, co-firing motifs therefore spanned different directions of the network activity space, segregating spatial contexts while discretizing events within them. Likewise, multiple axes explained the variance in hippocampal co-firing in the other tasks, by highlighting novelty and discerning individual mnemonic events, suggesting it could be a general framework to organise information in the network (Fig. 4.2.3h-j).

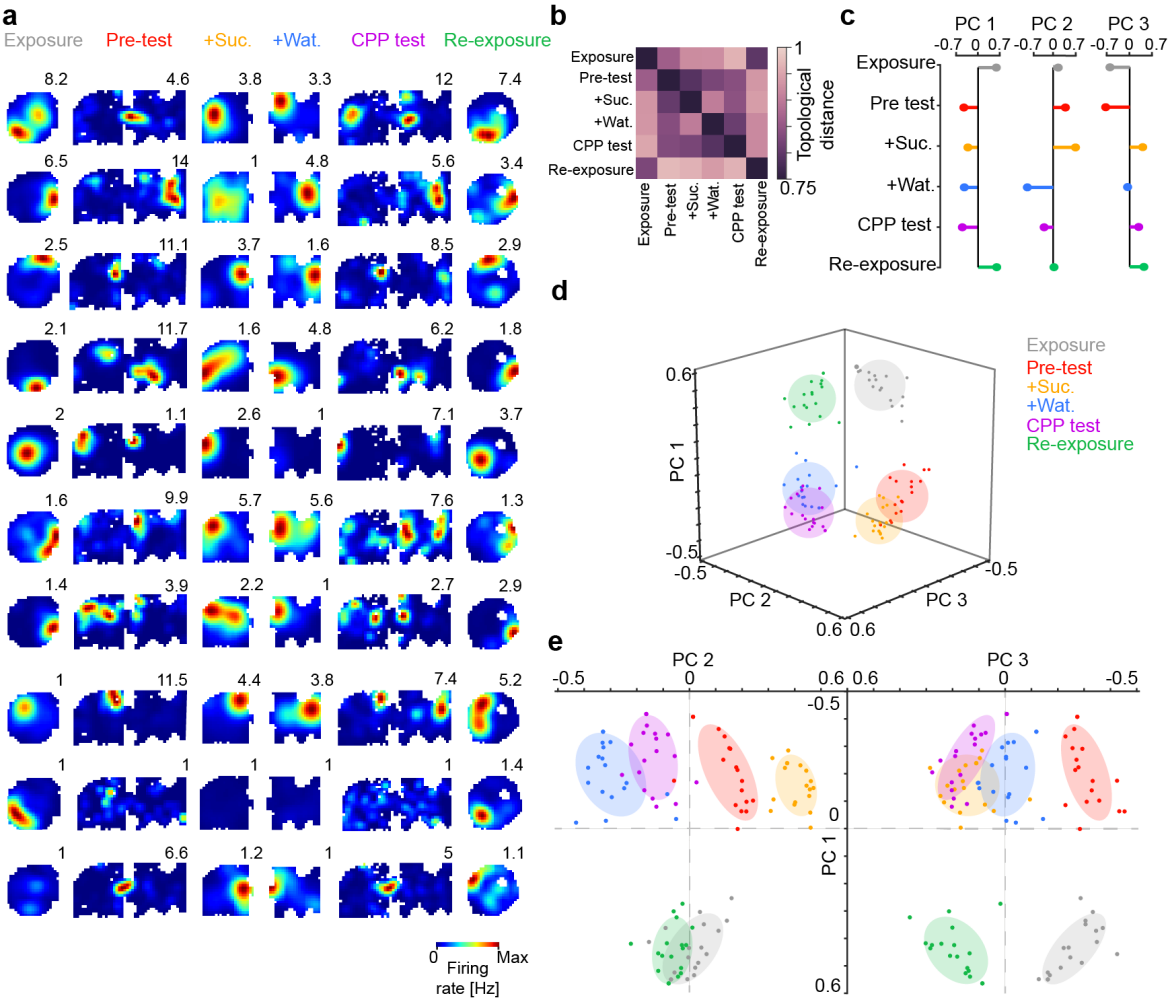

Figure 4.2.1: Mnemonic information spans multiple network co-firing axes. **a**, Example firing maps across CPP task sessions (one cell per row; numbers indicate peak rate). **b**, Average matrix of the topological distances separating the co-firing graphs across the six CPP task sessions. **c**–**e**, PC analysis applied to matrices of topological distances unfolded multiple axes explaining across-session variance in co-firing. **c**, Weight vectors representing the contribution of individual sessions to the variance in topological distances along the first three PCs. **d**, Projection of the topological distances between co-firing motifs onto the first three PCs. Each data point represents one (color-coded) session of a given mouse day. **e**, Same topological distances projected on the PC1 versus PC2 (left) and PC3 (right) planes. Note the segregation of co-firing motifs along PC1 for sessions in familiar versus CPP enclosures, for the four CPP sessions along PC2 and for exposure/re-exposure sessions along PC3.

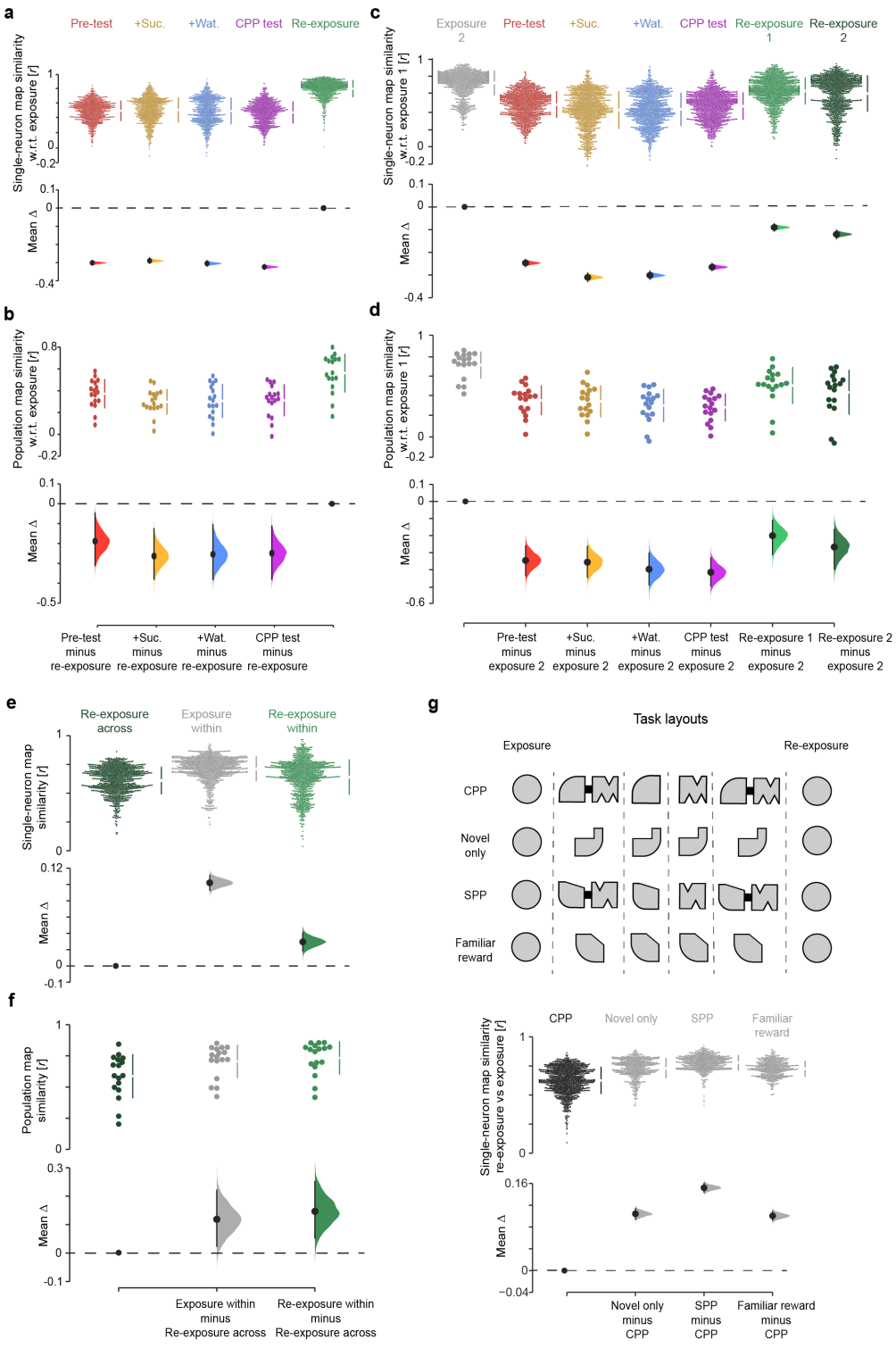
a
Pre-test
+Suc.
+Wat.
CPP test
Re-exposure
Single-neuron map similarity w.r.t. exposure [r]
Mean Δ
b
Population map similarity w.r.t. exposure [r]
Mean Δ
Pre-test minus re-exposure
+Suc. minus re-exposure
+Wat. minus re-exposure
CPP test minus re-exposure
c
Exposure 2
Pre-test
+Suc.
+Wat.
CPP test
Re-exposure 1
Re-exposure 2
Single-neuron map similarity w.r.t. exposure 1 [r]
Mean Δ
d
Population map similarity w.r.t. exposure 1 [r]
Mean Δ
Pre-test minus exposure 2
+Suc. minus exposure 2
+Wat. minus exposure 2
CPP test minus exposure 2
Re-exposure 1 minus exposure 2
Re-exposure 2 minus exposure 2
e
Re-exposure across
Exposure within
Re-exposure within
Single-neuron map similarity [r]
Mean Δ
f
Population map similarity [r]
Mean Δ
Exposure within minus Re-exposure across
Re-exposure within minus Re-exposure across
g
Task layouts
Exposure
Re-exposure
CPP
Novel only
SPP
Familiar reward
CPP
Novel only
SPP
Familiar reward
Single-neuron map similarity re-exposure vs exposure [r]
Mean Δ
Novel only minus CPP
SPP minus CPP
Familiar reward minus CPP

Figure 4.2.2: Familiar map-representations are largely reinstated during re-exposure after CPP but include edits not explained by mere fluctuations. **a,b**, Cumming estimation plots showing the effect size for changes in the similarity of both single-neuron (**a**) and population (**b**) spatial maps across CPP task sessions, with respect to (w.r.t.) exposure. For the single-neuron map similarity analysis (**a**), each data point represents the Pearson correlation using the firing rate of an individual neuron between the spatial bins of its map during exposure matched to those in a subsequent session. Note that single-neuron familiar maps are well reinstated during re-exposure following their reorganization during CPP sessions. For the population-level map similarity analysis (**b**), each data point represents the extent to which on a given CPP day pairs of cells that jointly represented a location during exposure continued to show spatially overlapping firing fields in subsequent sessions. This indicates that the combination of cell pairs sharing place fields during exposure largely re-emerges during re-exposure after their reorganization in the CPP enclosure, consistent with the remapping of hippocampal maps across spatial contexts. **c-g**, The strength of familiar map reinstatement from exposure to re-exposure was compared to non-specific fluctuations in firing activity over time. (**c**) With respect to the first section (half) of exposure, shown is the effect size for changes in single-neuron map similarity during the second section of the exposure, the 4 CPP sessions and the two (first and second) sections of re-exposure. **d**, Same as (**c**) but for the population map similarity. **e,f**, To contrast the effect of CPP on familiar map reinstatement against within-session variations in single-neuron (**c**) and population (**d**) map similarity, we compared the spatial correlation of hippocampal maps between exposure and re-exposure (Re-exposure across) with that between the two sections of the exposure (Exposure within) and of the re-exposure (Re-exposure within). The across-session fluctuations were quantified by comparing maps of each of the two re-exposure half sections (computed as in (**c,d**)) with those of the two exposure half sections, taking the mean of the four resulting similarity scores. The within-session fluctuations were obtained by comparing maps of the two sections of exposure or re-exposure, as indicated. Note that both single-neuron (**e**) and population-level (**f**) map fluctuations are significantly smaller within an exploration session of the familiar enclosure than across, even though single-neuron map variations (**e**) within re-exposure are markedly larger than those within exposure before CPP. **g**, In addition, the effect of CPP on familiar map reinstatement was compared to familiar map reinstatement between exposure and re-exposure in the other tasks: unrewarded exploration of a novel enclosure ("*Novel context only*" task), spontaneous place preference for a novel place (*SPP*) and reward experience in another familiar enclosure (Familiar with reward). Altogether, these analyses show that while spatial maps expressed during re-exposure following CPP are strongly correlated with those initially seen during exposure before CPP (**a,b**), these reinstated maps nevertheless differ across these two sessions in the familiar enclosure of the CPP task more than changes expected from non-specific fluctuations occurring within a given exploration of the familiar enclosure or those due to the temporal gap between exposure and re-exposure (**c-g**). These results indicate a crosstalk between the new CPP memory and the prior hippocampal representation of the familiar enclosure. Subsequent analyses in this study relate such a crosstalk to changes in firing activity of low rate principal cells (see Figs. 4.3.3-4.3.6). For each Cumming estimation plot: black-dot, median or mean as indicated; black-ticks, 95% confidence interval; filled-curve: bootstrapped sampling-error distribution.

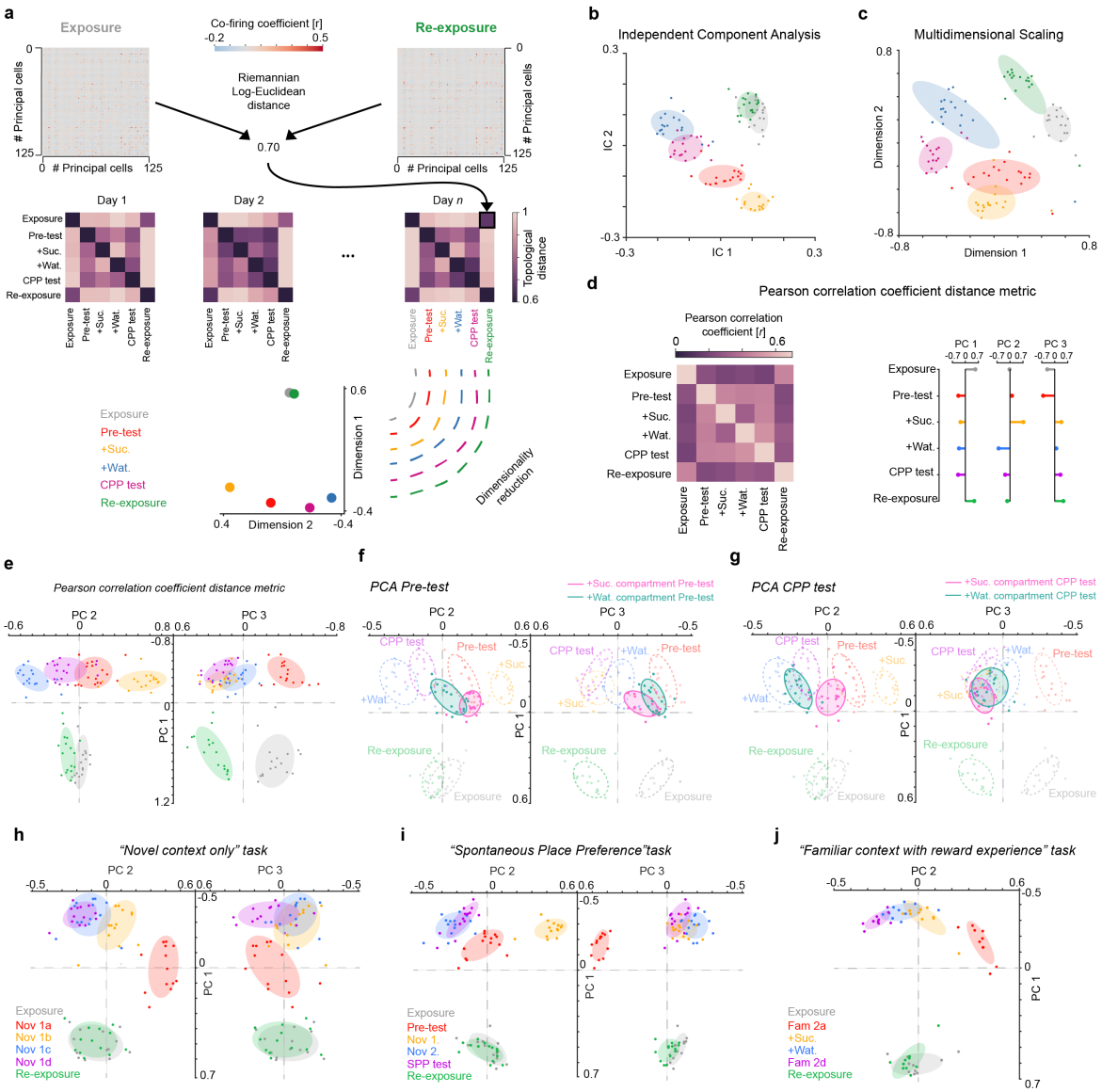
a
Exposure
Co-firing coefficient [r]
-0.2
0.5
Re-exposure
Principal cells
Riemannian
Log-Euclidean
distance
0.70
Day 1
Day 2
Day n
Topological distance
Exposure
Pre-test
+Suc.
+Wat.
CPP test
Re-exposure
Dimension 1
Dimension 2
Dimensionality reduction
b
Independent Component Analysis
IC 1
IC 2
c
Multidimensional Scaling
Dimension 1
Dimension 2
d
Pearson correlation coefficient distance metric
Pearson correlation coefficient [r]
PC 1
PC 2
PC 3
e
Pearson correlation coefficient distance metric
f
PCA Pre-test
+Suc. compartment Pre-test
+Wat. compartment Pre-test
g
PCA CPP test
+Suc. compartment CPP test
+Wat. compartment CPP test
h
"Novel context only" task
Nov 1a
Nov 1b
Nov 1c
Nov 1d
i
"Spontaneous Place Preference"task
Nov 1.
Nov 2.
SPP test
j
"Familiar context with reward experience" task
Fam 2a
Fam 2d

Figure 4.2.3: Visualizing transformations in the hippocampal network co-firing space. **a**, Computing the topological distances that separate co-firing graphs across the six task sessions. The co-firing graph of each task session was used to define a 6-dimensional vector of topological Riemannian Log-Euclidean distances to the other co-firing graphs obtained that day (for example here illustrated re-exposure versus exposure), including itself (see Methods). For each 6-session task day, this procedure thus gives a 6 x 6 matrix of topological distances between co-firing graphs. All distance matrices were then stacked together to form a 6 x N matrix (with N the number of total graphs, that is N = 17 days x 6 sessions = 102) onto which we apply a dimensionality reduction technique (PCA, ICA or MDS). **b,c**, Segregation of co-firing graphs using Independent Components Analysis (ICA; **b**) or Multidimensional Scaling (MDS; **c**). The shaded areas mark the best elliptical fit to the raw data projected on 2D. **b**, ICA applied to the same matrices of topological distances used with PCA in the CPP dataset (Fig. 4.2.1b) as another dimensionality reduction method to visualize axes explaining across-session variance in co-firing motifs. Note that co-firing graphs computed for the exposure and the re-exposure overlap on the first two independent components (IC) as they do along the first principal component (Fig. 4.2.1c–e); co-firing graphs are separated across the 4 CPP task events, as they are along the second principal component (Fig. 4.2.1c–e). **c**, MDS also applied to the same matrices of topological distances used with PCA in the CPP dataset (Fig. 4.2.1); this method preserves the six-dimensional distances between co-firing graphs and maps them onto a 2D plane. **d,e**, Here the Pearson correlation coefficient is used instead of the Riemannian Log-Euclidean distance to compute the topological distance between co-firing graphs across the six CPP task sessions. In (**d**) the average topological distance matrix (left) and its first three PCs (right) are shown. In (**e**) the segregation of the six CPP task sessions is shown using the PCs shown in (**d**). Note that for both the Riemannian Log-Euclidean distance (Fig. 4.2.1c–e) and the Pearson correlation coefficient (**d,e**) approaches, the PCA of the CPP dataset reveals that the variance in hippocampal co-firing segregated the familiar enclosure from the whole CPP test apparatus along PC1. Surprisingly, PC1 did not segregate the two compartments (Nov1 and Nov2) that formed the CPP apparatus. This suggests that these compartments were treated together as one spatial continuum along PC1 because when their novelty feature were equally novel and physically connected by the bridge during the pre-test. Therefore, a refined interpretation why along PC1 the two CPP compartments are clustered together (and different from the familiar enclosure) is that neuronal co-firing along this axis also accounts for spatial familiarity versus novelty. **f,g**, PCA with the two compartments of the CPP apparatus considered separately during both pre-test (**f**) and CPP test (**g**) sessions. Here, we computed a co-firing graph using the spike trains associated with the visits of each CPP compartment during both test sessions, thus obtaining one co-firing graph per individual compartment (Nov1 versus Nov2) during each test session. Projecting the resulting four co-firing graphs (two for pre-test and two for CPP test) onto the PCA axes obtained when considering the CPP apparatus as a whole entity (Fig. 4.2.1e) shows that PC2 segregates co-firing patterns related to each CPP compartment during CPP test compared to pre-test. **h-j**, The topological distance projections of the co-firing graphs from the other 6-session tasks. Note, however, that co-firing variance relates to the specifics of each task, and so is each set of PCs and their interpretation. For each task, we used the PCs explaining at least 80% of the total variance to project the co-firing graphs topological distance. The variance explained by these PCs is: "Novel context only" PC1=57%, PC2=19% and PC3=8%; "Spontaneous Place Preference" PC1=52%, PC2=18% and PC3=16%; "Familiar context with reward experience" PC1=69%, PC2=15%; and "CPP" PC1=48%, PC2=19% and PC3=14% (Fig. 2e).

4.3.3 The heterogeneous population of principal cells differently supports the network co-firing axes

Recent findings suggest that the heterogeneity of the principal cell population, marked by the skewed (log-normal) distribution of firing rates, is central to the network operations underlying hippocampal function (Mizuseki, Diba, et al., 2011; Buzsáki and Mizuseki, 2014; Rich et al., 2014; Soltesz and Losonczy, 2018; Grosmark and Buzsáki, 2016; Cembrowski and Spruston, 2019; Navas-Olive et al., 2020). We thus identified principal cells in the top and bottom quartiles of the firing rate distribution during the exposure session (Fig. 4.3.1a) to examine the contribution of these two subpopulations to the topology of the co-firing networks. High and low-rate principal cells were biased towards deep and superficial pyramidal sublayers, respectively. To estimate the position of the neurons recorded with tetrodes, we leveraged on silicon probe recordings with known spacing between the recording sites along a linear shank, to obtain template profiles of the SWR events along the radial axis of dCA1 (Fig. 4.3.2a-b). Then, we were able to estimate the depth of the implanted tetrodes for CPP days finishing with a sleep session, by matching the profile of the SWR events with the template obtained using the silicone probe (Fig. 4.3.2c-d). The estimated tetrode depths [+83.8μm, -166.2μm] are outside the thickness of the pyramidal layer (100μm), which leads to the estimation of the cell position outside of the layer. This is because the electrodes on each tetrode can pick up signals within a radius of 100μm (Buzsáki, 2004) and therefore induce some uncertainty in the depth estimation itself. Even though the depth estimation just described is not very precise and its results taken with caution, in line with previous findings, we found that pyramidal cells within the deep sublayer exhibited higher firing rate values and bursting propensity than cells within the superficial sublayer (Fig. 4.3.2e-f; Mizuseki, Diba, et al., 2011, Danielson et al., 2016, Oliva et al., 2016). Because of the intrinsic

limitation of depth estimation using tetrodes, we decided to continue to use the low-high activity criteria to separate cells, but further work should be done using either silicon probes or genetic birth date tagging to obtain a more precise labelling of putative deep and superficial pyramidal cells (Cavalieri et al., 2021).

We observed that low, but not high, activity cells discharged more bursts of spikes (spike packets with inter-spike intervals within 6ms) during re-exposure compared to exposure (Fig. 4.3.1b and Fig. 4.3.3a,b), sustaining increased firing rate one hour after CPP (Fig. 4.3.3c). These lasting activity changes were not observed in the other three tasks (Fig. 4.3.3d-i). Moreover, in the CPP task, low activity cells with higher bursting during re-exposure showed increased spatial coherence and information content, in line with their heightened firing (Fig. 4.3.3b-c), which was not the case for the other tasks (Fig. 4.3.4). Remarkably, these cells that initially had the lowest place-field coherence during exposure increased both their spatial information content and burst spiking propensity following CPP learning. In addition, low activity cells with the most spatially tuned activity during exposure also showed increased spatial information during re-exposure, without altered burst spiking (Fig. 4.3.5). On the other hand, high activity cells maintained a high spatial information content and spatial coherence throughout the entire task (Fig. 4.3.5). These results suggested that the cross-talk between the new CPP memory and the prior familiar representation involved the heightened network contribution of low activity cells following their recruitment during CPP learning. Indeed, the low – but not high – activity subpopulation exhibited sustained topological changes throughout CPP sessions (Fig. 4.3.5a), explaining whole-network hysteresis during re-exposure (Fig. 4.1.1f). Moreover, reward-related firing modulation of low activity cells from pre-test to sucrose conditioning in the CPP enclosure predicted changes in co-firing from exposure to re-exposure in the familiar enclosure (Fig. 4.3.6b,c), constituting another instance of the impact of reward on hippocampal

activity (Danielson et al., 2016; Gauthier and Tank, 2018; Dupret et al., 2010).

We finally evaluated the contribution of high and low activity pyramidal cell subpopulations to the network co-firing motifs, leveraging the Riemannian Log-Euclidean framework (Fig. 4.2.1b-e and Fig 4.2.3a). Co-firing within high activity cells segregated the two task enclosures at the onset of pre-test (Fig. 4.3.1c and Fig. 4.3.6d). Coactivity motifs including low activity cells, instead, did not distinguish familiar exposure and novel CPP pre-test (Fig. 4.3.1c and Fig. 4.3.6d). Rather, this subpopulation gradually participated in the network co-firing patterns as mice experienced each task event, remaining engaged thereafter during re-exposure where their contribution to the network motifs reached that of high activity cells. Accordingly, in the CPP task, patterns within high and low activity cells supported more the first and third co-firing network axis, respectively; while their combination explained more the second axis (Fig. 4.3.1d). Moreover, low - but not high - activity cells exhibited increased firing at the reward wells during the sucrose conditioning session (+Suc.), in line with the changes in their co-firing topology (Fig. 4.3.6b-c). The topological changes affecting the co-firing structure of the network throughout the CPP task were associated with changes in sharp-wave/ripple firing and of low activity cells during awake rest (Fig. 4.3.6e,f), in line with recent work showing that these two subpopulations exhibit distinct sharp-wave/ripple responses (Grosmark and Buzsáki, 2016; Valero et al., 2015).

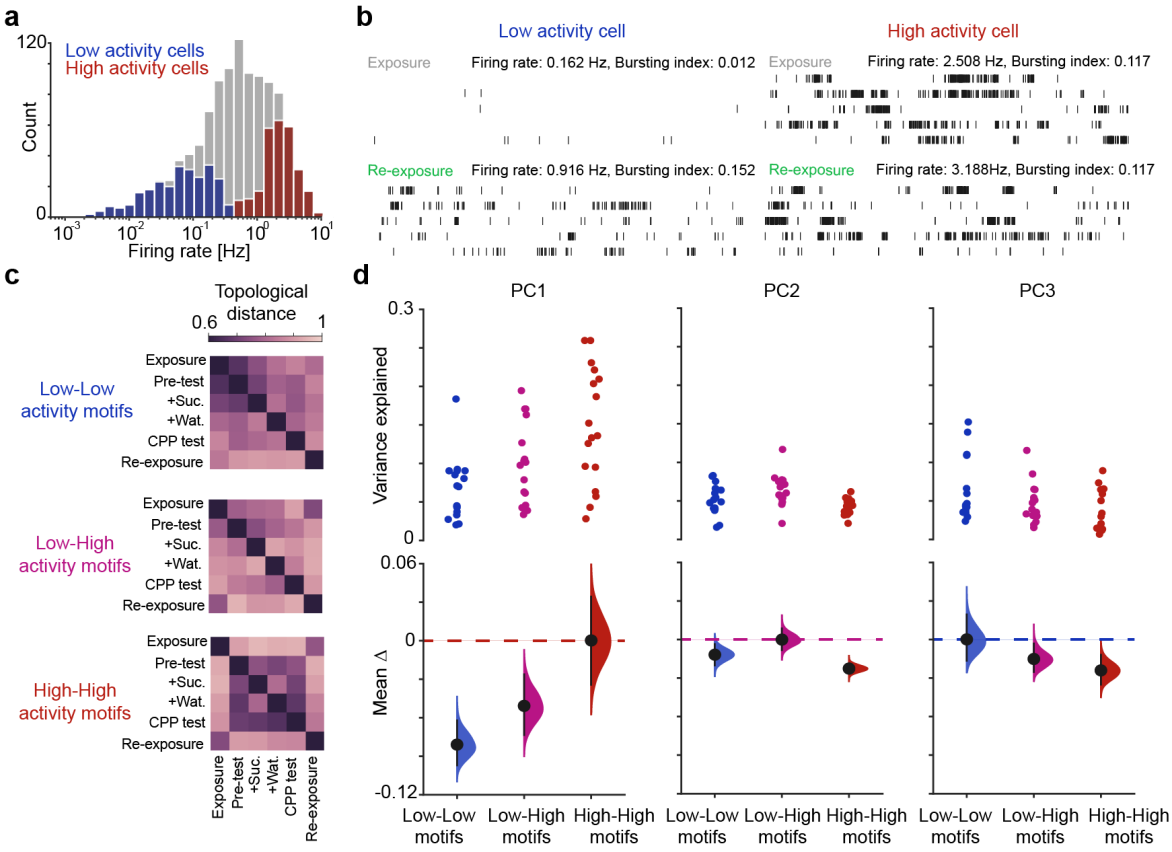

Figure 4.3.1: High and low activity cells contribute differentially to network co-firing axes. **a**, Firing rate (log-normal) distribution of principal cells during exposure. The highest and lowest quartiles formed the high- and low-activity subpopulations, respectively. **b**, Example spike trains of a low-activity cell and a high-activity cell during exposure and re-exposure. Two raster plots shown for each cell (60-s rows, vertical ticks representing spike times) during exposure (top) and re-exposure (bottom). For clarity, the first 5 min of each session is represented. **c**, Matrices of topological distances separating co-firing graphs across sessions, for low–low-, low–high- and high–high-activity cell pairs. **d**, Cumming estimation plots showing the contribution of low–low-, low–high- and high–high-activity cell pairs to co-firing variance along the first three axes of the CPP network. Top: each data point represents the variance explained by a given co-firing motif along one axis for 1 d. Bottom: for each axis, the co-firing motif with the strongest contribution (color-coded dashed line) is compared with the other two motifs' contribution. Black dot, mean difference; black ticks, 95% confidence interval; filled curve: sampling error distribution.

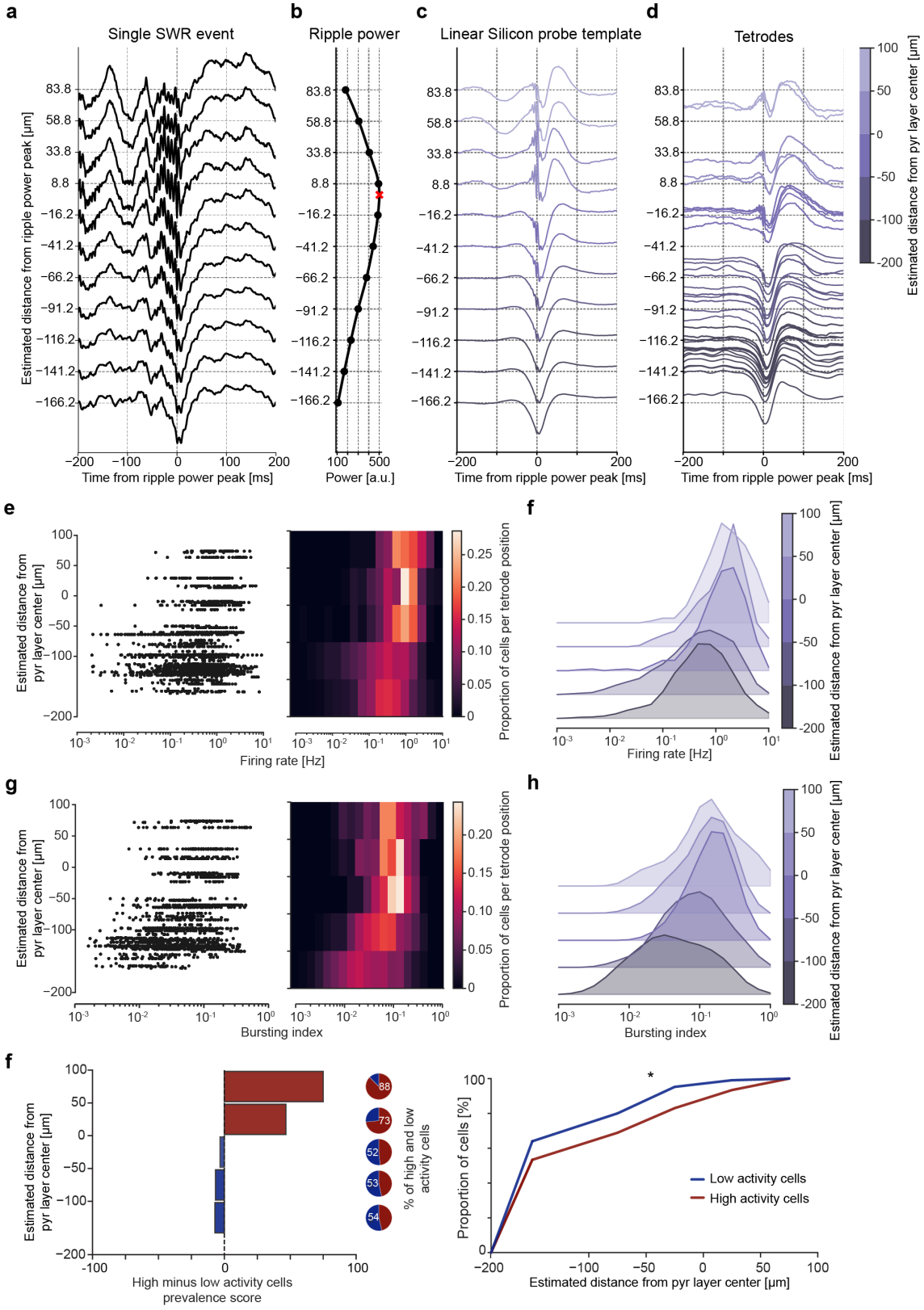
a
Single SWR event
Estimated distance from ripple power peak [µm]
Time from ripple power peak [ms]
b
Ripple power
Power [a.u.]
c
Linear Silicon probe template
Time from ripple power peak [ms]
d
Tetrodes
Time from ripple power peak [ms]
Estimated distance from pyr layer center [µm]
e
Estimated distance from pyr layer center [µm]
Firing rate [Hz]
Proportion of cells per tetrode position
f
Firing rate [Hz]
Estimated distance from pyr layer center [µm]
g
Bursting index
h
Bursting index
f
High minus low activity cells prevalence score
% of high and low activity cells
Proportion of cells [%]
Low activity cells
High activity cells
Estimated distance from pyr layer center [µm]

Figure 4.3.2: High and low rate ca1 principal cells are skewed towards deep and superficial pyramidal sublayers, respectively. **a-d**, For each CPP task day, we estimated the position (depth) of individual tetrode-recorded principal cell soma by leveraging silicon probe recordings with known spacing between the recording sites along a linear shank (25-μm steps). From these silicon probe recordings, we first computed the laminar profile of sharp-wave/ripples (SWRs) detected in the local field potentials (LFPs) along the radial axis of the dCA1 hippocampus (**a**). We used the peak of the corresponding depth profile of the ripple-band (110-250Hz) power to estimate the centre (middle) of the pyramidal (pyr.) layer (**b**; red cross). Using the average LFP waveform of the SWR events detected in these silicone probe recordings, we then established a SWR template where we reported the distance relative to the estimated centre of the pyramidal layer, knowing the precise distance between the recording sites on the linear shank (**c**). Next, we computed the individual SWR profile of each tetrode for CPP recording days finishing with a sleep session, this way estimating the depth of each individual tetrode (and thus that of the somas of its recorded neurons) by positioning its SWR profile within the silicone probe SWR template (the ground-truth vertical depth; **c**). Shown in (**d**) are examples of single-tetrode SWR profiles and their estimated depth. **e**, Left: the estimated depth of principal cells as a function of the average firing rate measured in the CPP task. Each data point represents one principal cell. Right: the same data plotted as a firing rate probability distribution per estimated depth. **f**, Same data as in (**e**) but plotted as a ridge plot to better visualise the relation between firing rate of principal cells and depth of their recording tetrodes. Note that principal cells in the deep sublayer of the dCA1 pyramidal layer (closer to stratum oriens) show higher firing rates than those in the superficial sublayer (closer to stratum radiatum) (line of best fit: $y = 23.34\log(x) - 74.7$; p = 10^{-30}; two-sided Wald Test). **g,h**, The same analyses shown in (**e,f**) but performed for the bursting index. Note that principal cells of the deep dCA1 sublayer show higher spike bursting compared to those of the superficial sublayer (line of best fit: $y = 47.43\log(x) - 15.0$; p = 10^{-64}; two-sided Wald Test). **i**, Relative prevalence (left) and cumulative distribution (right) of low (blue) and high (red) rate principal cells along the dCA1 radial axis. Low and high activity cells are skewed towards superficial and deep dCA1 pyramidal sublayers, respectively (p=0.016, Kolmogorov-Smirnov 2-sample test).

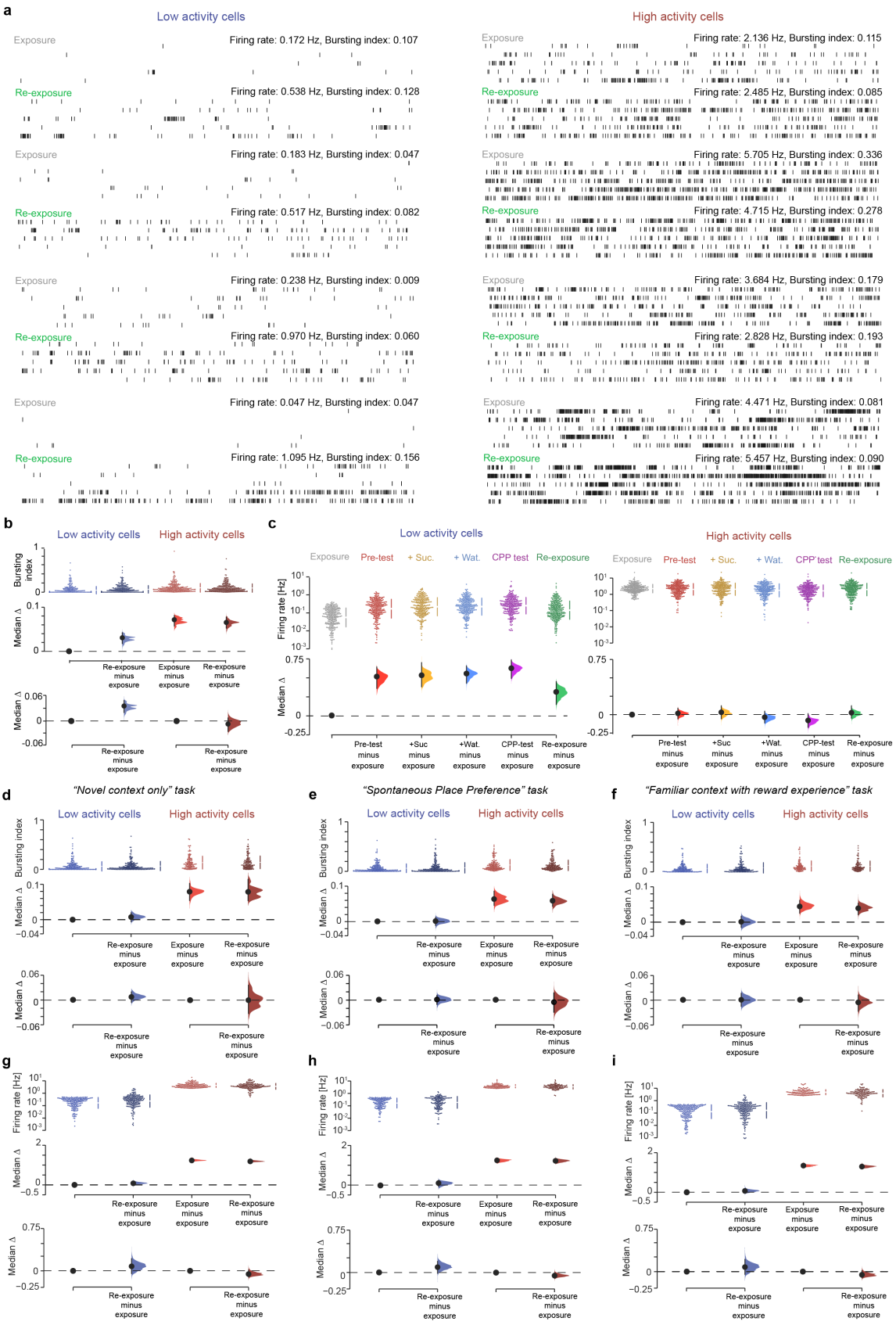
a
Low activity cells
High activity cells
Exposure
Re-exposure
Firing rate: 0.172 Hz, Bursting index: 0.107
Firing rate: 0.538 Hz, Bursting index: 0.128
Firing rate: 0.183 Hz, Bursting index: 0.047
Firing rate: 0.517 Hz, Bursting index: 0.082
Firing rate: 0.238 Hz, Bursting index: 0.009
Firing rate: 0.970 Hz, Bursting index: 0.060
Firing rate: 0.047 Hz, Bursting index: 0.047
Firing rate: 1.095 Hz, Bursting index: 0.156
Firing rate: 2.136 Hz, Bursting index: 0.115
Firing rate: 2.485 Hz, Bursting index: 0.085
Firing rate: 5.705 Hz, Bursting index: 0.336
Firing rate: 4.715 Hz, Bursting index: 0.278
Firing rate: 3.684 Hz, Bursting index: 0.179
Firing rate: 2.828 Hz, Bursting index: 0.193
Firing rate: 4.471 Hz, Bursting index: 0.081
Firing rate: 5.457 Hz, Bursting index: 0.090
b
Low activity cells
High activity cells
Bursting index
Median Δ
Re-exposure minus exposure
Exposure minus exposure
c
Low activity cells
High activity cells
Exposure
Pre-test
+ Suc.
+ Wat.
CPP test
CPP' test
Re-exposure
Firing rate [Hz]
Median Δ
Pre-test minus exposure
+Suc minus exposure
+Wat. minus exposure
CPP-test minus exposure
d
"Novel context only" task
e
"Spontaneous Place Preference" task
f
"Familiar context with reward experience" task
g
h
i

Figure 4.3.3: Low activity principal cells show increased firing activity during re-exposure to the familiar enclosure following CPP learning. **a**, Example spike trains of low and high activity cells during exposure and re-exposure to the familiar environment. For each of the eight example cells, shown are two raster plots (60-s rows; vertical ticks representing spike times) for exposure (upper plot) and re-exposure (lower plot). For clarity, only the first 5 min of each session are presented. Note the increased spike burst discharge by low activity cells during re-exposure compared to exposure. **b**, Cumming estimation plot used to visualize for low (blue colours) and high (red colours) activity cells the effect size for changes in spike bursting between re-exposure and exposure. Upper panel: distributions of raw data points (each color-coded point represents one cell from the CPP task: n=272 low activity cells and 272 high activity cells) during exposure and re-exposure in light and dark colours, respectively; with the gapped lines on the right as mean (gap) ± SD (vertical ends) for a given subpopulation in a given session. Middle panel: the median (black-dot), 95% confidence interval (black-ticks) and sampling-error distribution (filled-curve) of the difference between (low or high activity) cells in a given session and the low activity cells in exposure, computed from 5,000 bias-corrected bootstrapped resamples and with the difference-axis (dashed-line) origin aligned to the median of low activity cells in exposure. Lower panel: similarly, compares the distribution in re-exposure to that in exposure within each sub-population. Note that low, but not high, activity cells significantly discharge more bursts of spikes during re-exposure following CPP compared to exposure. The lack of increased bursting of the high activity cells during re-exposure compared to exposure does not reflect a ceiling effect given that the burst spiking distribution of this sub-population had an inter-quartile range=0.07–0.18, a median=0.12 and a mean=0.15 throughout the CPP task sessions (see also the corresponding raw data points in Fig. 4.3.5d and the coherence-percentiles' mean in Fig. 4.3.5h), showing that this sub-population could have discharged more bursts during re-exposure. **c**, Cumming estimation plots to visualize the change in firing rate across CPP task sessions for the low (left panel) and the high (right panel) activity cell sub-populations. Note that firing rate of low activity cells increased during CPP sessions and stayed at higher values during re-exposure, not resetting to the values seen in exposure. **d-i**, Bursting index (**d-f**) and firing rate (**g-i**) of high and low activity principal cells in the exposure and re-exposure to the familiar enclosure during the other tasks: exploration of a novel enclosure only (**d,g**), spontaneous place preference for a novel place (**e,h**) and exploration of another familiar enclosure with reward (**f,i**). Each (color-coded) data point represents one cell ("Novel context only" task: n=214 low activity cells and 128 high activity cells; "Spontaneous Place Preference" task: n=188 low activity cells and 152 high activity cells; "Familiar context with reward experience" task: n=148 low activity cells and 96 high activity cells). All differences presented using Cumming estimation plots as in (**b**). Note that in these three other tasks, low activity cells did not show significant changes in burst spiking and firing rate during re-exposure compared to exposure.

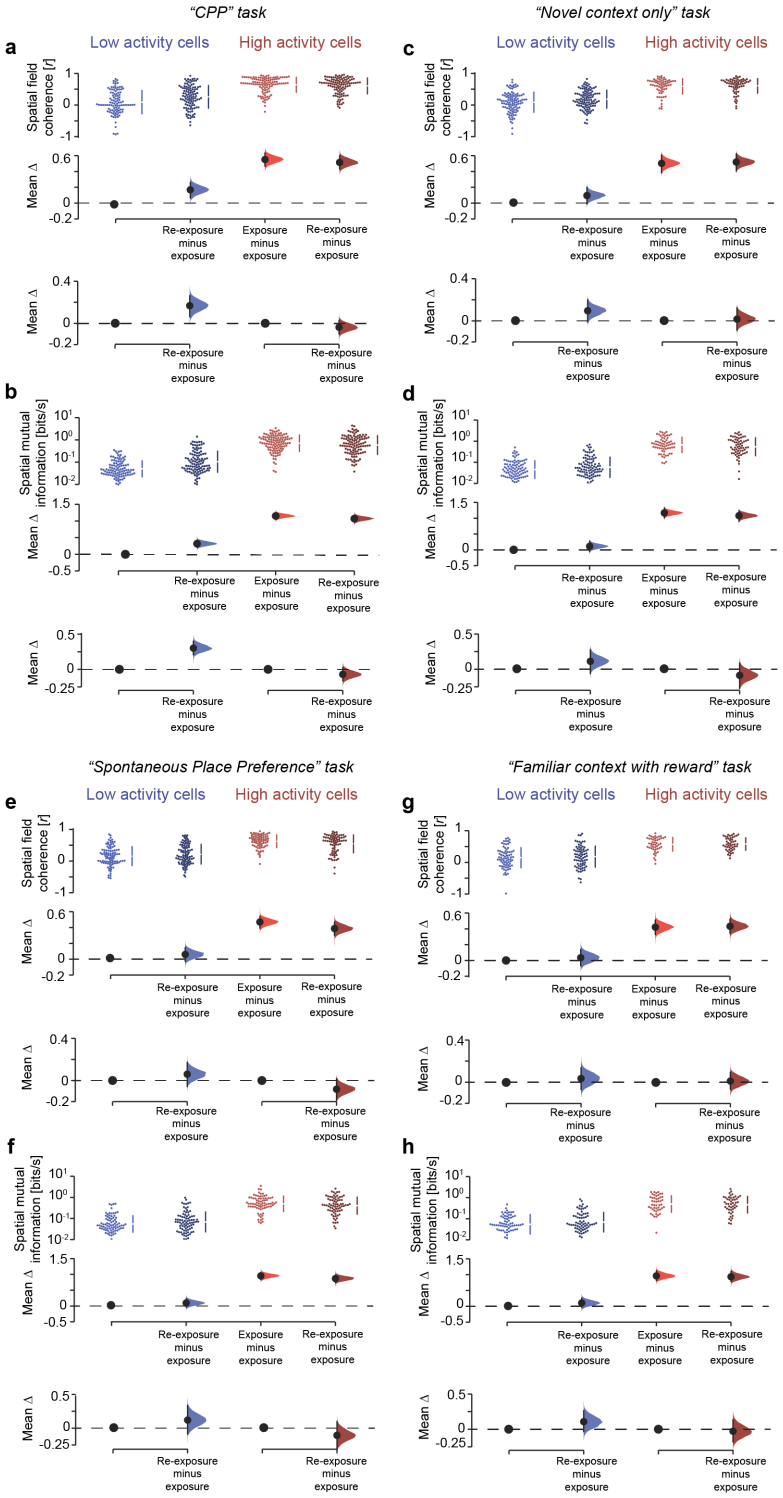
"CPP" task
"Novel context only" task
"Spontaneous Place Preference" task
"Familiar context with reward" task
Low activity cells
High activity cells
a
b
c
d
e
f
g
h
Spatial field coherence [r]
Spatial mutual information [bits/s]
Mean Δ
Re-exposure minus exposure
Exposure minus exposure
Re-exposure minus exposure

Figure 4.3.4: Low activity cells with increased burst spiking following CPP exhibited stronger place field coherence and spatial information content. **a,b**, Cumming estimation plots showing for low (blue colours) and high (red colours) activity cells the effect size in changes of place field coherence (**a**) and spatial mutual information (**b**) between exposure and re-exposure in the CPP task. The most burst spiking cells of both subpopulation (top 40% of bursting index distribution) in the re-exposure session are considered. Note that low, but not high, activity cells have significantly higher spatial coherence (**a**) and mutual information (**b**) during re-exposure after CPP. **c-h**, Similarly, the place field coherence (**c,e,g**) and the spatial mutual information (**d,f,h**) of low and high activity principal cells is shown for the other tasks including exposure and re-exposure sessions. Low and high activity cells selected in the same way as in the CPP task dataset (**a,b**) to allow for comparison. For each Cumming estimation plot: black-dot, median (for skewed distributions) or mean (for normal distributions) as indicated; black-ticks, 95% confidence interval; filled-curve: bootstrapped sampling-error distribution.

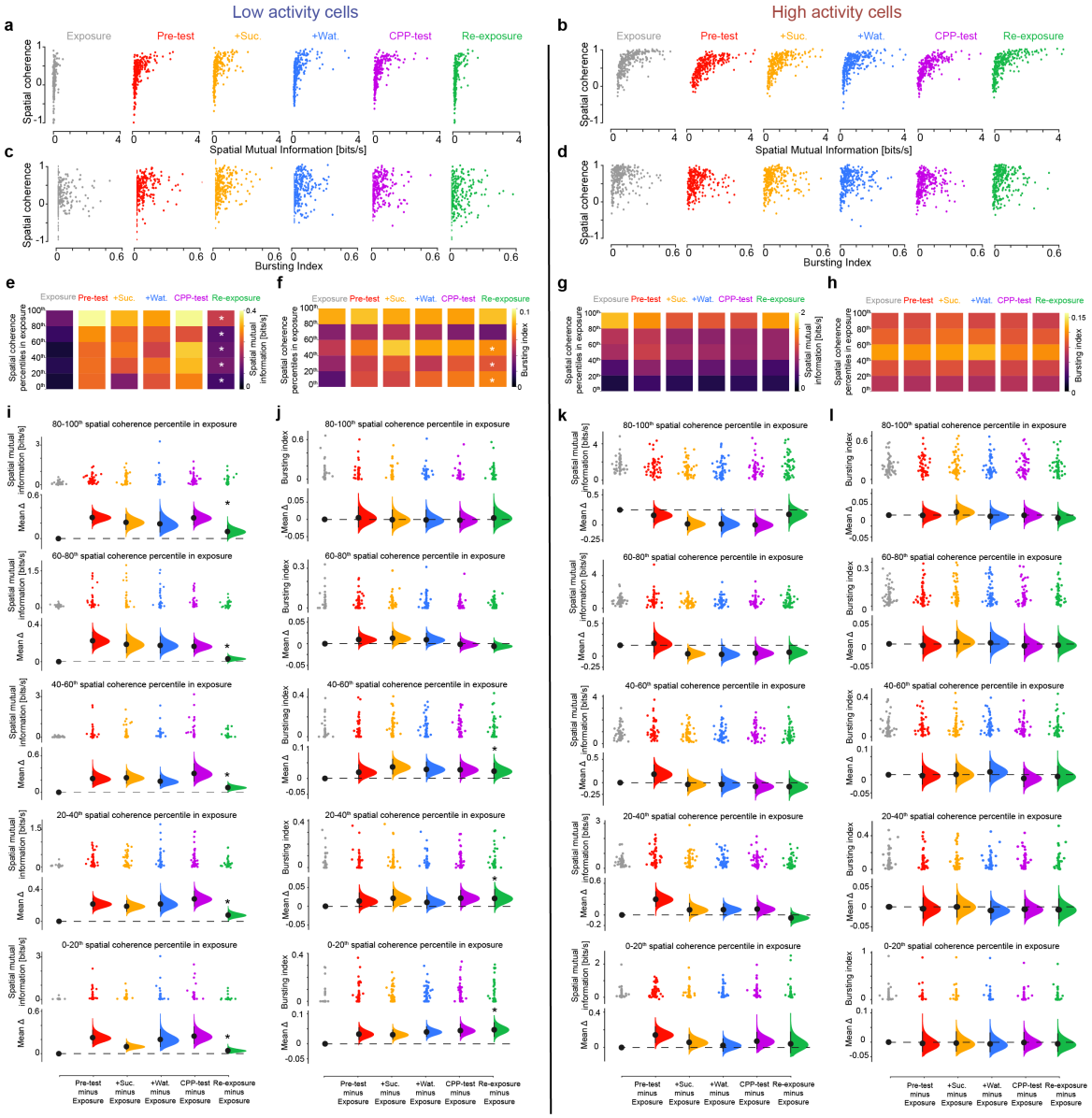
Low activity cells
High activity cells
a
b
c
d
e
f
g
h
i
j
k
l
Exposure
Pre-test
+Suc.
+Wat.
CPP-test
Re-exposure
Spatial coherence
Spatial Mutual Information [bits/s]
Bursting Index
Spatial coherence percentiles in exposure
Spatial mutual information [bits/s]
Bursting index
80-100th spatial coherence percentile in exposure
60-80th spatial coherence percentile in exposure
40-60th spatial coherence percentile in exposure
20-40th spatial coherence percentile in exposure
0-20th spatial coherence percentile in exposure
Mean Δ
Pre-test minus Exposure
+Suc. minus Exposure
+Wat. minus Exposure
CPP-test minus Exposure
Re-exposure minus Exposure

Figure 4.3.5: Relation between spatial field coherence during exposure and subsequent changes in both burstiness and spatial information for low and high activity cells in the CPP task. **a,b**, The spatial mutual information of low and high activity cells is plotted against their respective spatial coherence for each of the six CPP task sessions. Each data point represents one cell. Comparing with exposure, note the right-shift towards higher spatial information for a set of low activity cells during the CPP sessions, which then remained at higher values during re-exposure (**a**). **c,d**, Similarly, the bursting index of low and high activity cells is plotted against their spatial coherence for each CPP task session. Also comparing with exposure, note the right-shift towards higher spike bursting in the distributions of low activity cells during CPP sessions, remaining higher during re-exposure (**c**). **e-h**, For each of the six CPP task sessions, both low (**e,f**) and high (**g,h**) activity cell sub-populations were binned in 20th-percentiles according to the spatial coherence of each cell's place field during the exposure session. Then, the average spatial mutual information (**e,g**) and bursting index (**f,h**) were computed for each 20th-percentile bins across all task sessions. For clarity, the bins of the re-exposure session marked with a white star (*) have significant changes in either measure (spatial information or bursting index) compared to the corresponding bins in the exposure session. Note that during re-exposure, low activity cells show significant increase in spatial information following CPP compared to exposure (**e**). This was not the case for high activity cells (**g**). Moreover, low activity cells with the least (0th–60th percentiles) spatial coherence during exposure increased their spike bursting during the CPP sessions and thereafter during re-exposure (**f**; with statistically different percentile bins marked with a white star compared to their corresponding bins in exposure). This was not seen for high activity cells (**h**). **i-l**, Cumming estimation plots showing the effect size for changes in spatial information (**i,k**) and bursting index (**j,l**) for the low (**i,j**) and the high (**k,l**) activity cell sub-populations, binned as 20th-percentiles according to the spatial coherence of each cell's place field during exposure. For further clarity, the black stars above the green filled-curves in re-exposure indicate significant changes compared to exposure. Note that across all percentile bins, low activity cells show significant increase in spatial information in re-exposure compared to exposure (**i**). This was not seen for high activity cells (**k**). Moreover, low activity cells with the least (0th–60th percentiles) spatial coherence during exposure thereafter discharged more spike bursts during the CPP sessions and continued to exhibit significant higher burstiness during re-exposure compared to exposure (**f,j**; see stars). High activity cells maintained the same burstiness throughout all task sessions (**h,l**). For each Cumming estimation plot: black-dot, mean; black-ticks, 95% confidence interval; filled-curve: bootstrapped sampling-error distribution.

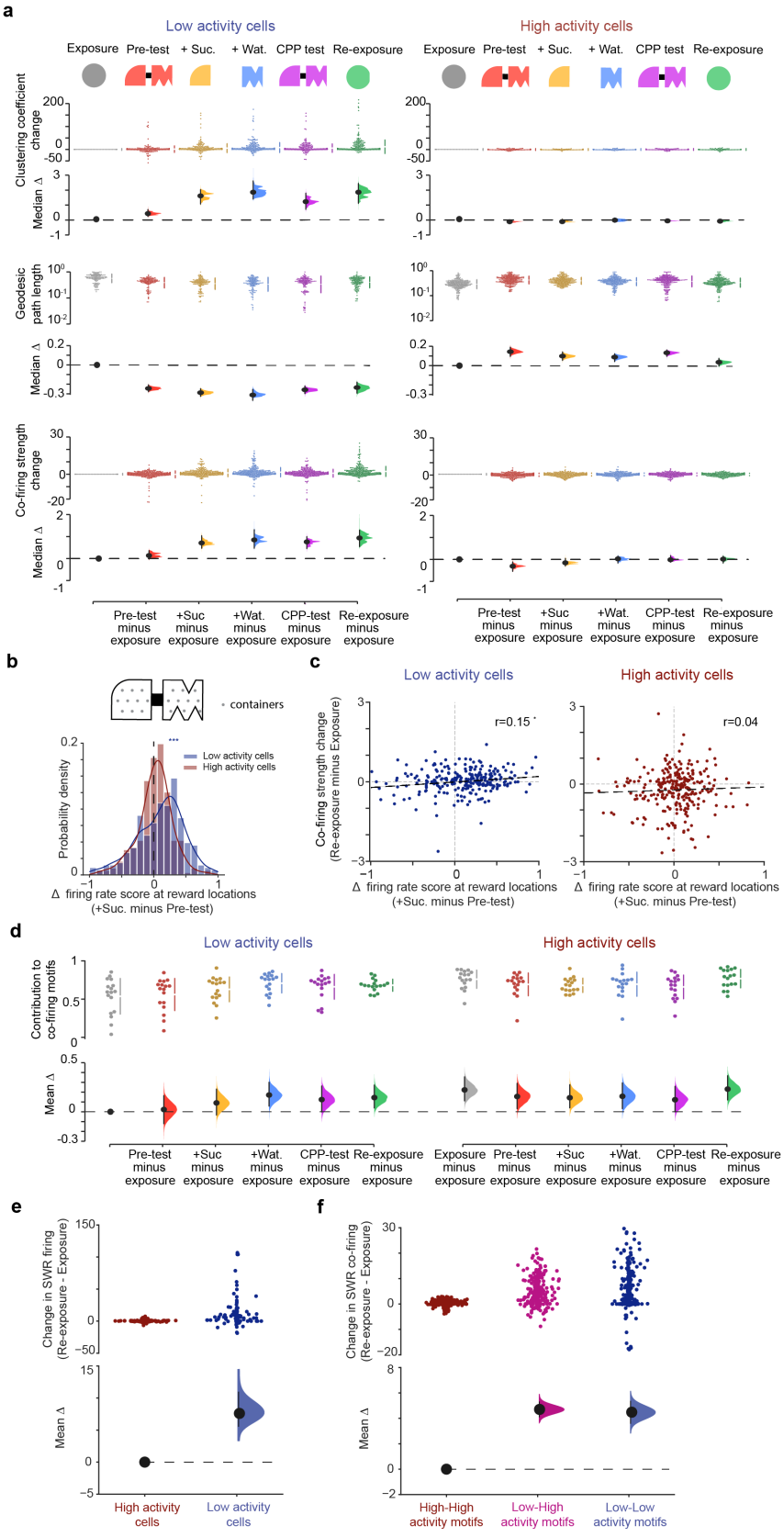
a
Low activity cells
High activity cells
Exposure
Pre-test
+ Suc.
+ Wat.
CPP test
Re-exposure
Clustering coefficient change
Median Δ
Geodesic path length
Co-firing strength change
Pre-test minus exposure
+Suc minus exposure
+Wat. minus exposure
CPP-test minus exposure
Re-exposure minus exposure
b
containers
Low activity cells
High activity cells
Probability density
Δ firing rate score at reward locations (+Suc. minus Pre-test)
c
Low activity cells
High activity cells
r=0.15
r=0.04
Co-firing strength change (Re-exposure minus Exposure)
Δ firing rate score at reward locations (+Suc. minus Pre-test)
d
Low activity cells
High activity cells
Contribution to co-firing motifs
Mean Δ
Exposure minus exposure
e
Change in SWR firing (Re-exposure - Exposure)
Mean Δ
High activity cells
Low activity cells
f
Change in SWR co-firing (Re-exposure - Exposure)
Mean Δ
High-High activity motifs
Low-High activity motifs
Low-Low activity motifs

Figure 4.3.6: High and low activity principal cells make distinct contributions to network co-firing motifs. **a**, Cumming estimation plots showing CPP task-related changes in topological clustering (top), geodesic path length (middle) and single-neuron cumulative co-firing strength (bottom) of co-firing graphs (with respect to exposure) for low and high activity cells. Black-dots, median; black-ticks, 95% confidence interval; filled-curve: sampling-error distribution. **b**, Top, schematic showing the location of the containers for the sucrose and water drops in an example CPP enclosure. Bottom, distribution of firing rate changes (scores) between the +Suc and pre-test sessions for low and high activity cells (low activity cells: p=2.68×10^{-5}, t=4.279, df=251; high activity cells: p=0.25, t=1.160, df=271; 1-sample t-tests against 0 mean). For every cell that fired at least 100 spikes in either session, a score is obtained by taking the difference between its mean firing rate at the containers during +Suc and pre-test sessions, dividing by the sum. **c**, The change in firing rate at the containers from pre-test to +Suc. session correlated with the change in co-firing strength from exposure to re-exposure for the low (regression line $y = 0.21x - 0.11$; p=0.018, Wald test) but not the high (regression line $y = 0.12x - 0.23$; p=0.51, Wald test) activity cells. Together with the topological deviations that feature the low activity cell co-firing graphs (**a**), this result supports the idea that during the mnemonic update of a newly encountered place with reward experience, a change in the firing activity of low activity cells allows a cross-talk between the new CPP memory and the prior representation of the familiar enclosure, as reported along PC3 (Fig. 4.3.1d). **d**, Contribution of low and high activity cells to network co-firing motifs, as measured by the proximity between the high (right) and low (left) activity sub-networks to the whole network (that is, containing the full distribution of all recorded neurons) in the topological distance space across the six CPP task events (w.r.t. low activity cells in exposure). Black-dot, median or mean as indicated; black-ticks, 99% confidence interval; filled-curve: sampling-error distribution. **e**, For low and high activity cells, firing rate changes during sharp-wave/ripples (SWRs) detected in periods of immobility (speed¡2cm/sec) of exposure and re-exposure sessions. For every cell, the change in SWR firing is measured as the difference between its mean firing rate during SWRs in the exposure and re-exposure sessions divided by the sub-population's average firing rate during SWRs of exposure. **f**, Change in co-firing during SWRs between exposure and re-exposure for low-low, low-high and high-high activity cell pairs. SWR co-firing computed during SWRs detected in periods of immobility (speed<2cm/sec) of a given exploration session in the familiar enclosure. The change in co-firing between re-exposure and exposure was then divided by the average sub-population's co-firing. Note the increased SWR co-firing between low-low and low-high activity cells during the re-exposure session following CPP learning.

4.4 Discussion

In this chapter, by exploring the dCA1 hippocampal network activity space from a graph-theoretical perspective, we show that new place-reward associative memories restructure the neural patterns representing prior memory for an unrelated environment. During this transformation of the hippocampal co-firing structure, high activity cells organize motifs that rapidly discriminate spatial contexts, robust to perturbation by subsequent experience. This contribution might instantiate a spatio-contextual backbone for memory schemas, which would enable subsequent related memories to be rapidly encoded (McKenzie, A. J. Frank, et al., 2014; Tse et al., 2007). Low activity cells, instead, integrate coactivity motifs on-demand, throughout behavioural events. Their heightened engagement, fostered by the new place-reward learning, persists across contexts, affecting the network representation of an otherwise familiar environment. This effect could involve low-rate principal cell plasticity (Grosmark and Buzsáki, 2016) leveraged by high computational load or neuro-modulatory processes when novel contextual information and reward experience are related in memory.

Even though only associative learning induced a restructuring of the co-firing patterns representing a previous memory, we find that novelty alone generates a common mechanism enhancing neuronal co-activity within the dCA1 network, as shown by the co-firing topological deviations observed during both the CPP task (Fig. 4.1.1f), but also the SPP, "novel context only" and "familiar context with reward" tasks (Fig. 4.1.3). This suggests that correlated activity might aid the encoding of consistent information within the neural circuitry, as relevant literature proposes (Diesmann et al., 1999; Salinas and Sejnowski, 2001; Zandvakili and Kohn, 2015; Zylberberg et al., 2017; Valente et al., 2021). Another point to highlight is that the increase in the network co-activity might be caused by a global

increase in the firing rate of the individual neurons, although the rate dynamics do not seem to follow the co-firing ones (see Figs. 4.3.3c) but this should be tested more rigorously. Moreover, further work should be done to investigate whether the increased network co-firing is due to the independent increase of pairwise interactions within neurons in the network or is it driven by an external common input to the network that is increasing as the memory encoding progresses. A possible solution could be employing a GLM, or another similar technique, to separate shared inputs driven correlations, such as behavioural or network states, from individual pairwise correlations.

The newly-acquired topology of the hippocampal firing output, shaped by past inputs, may not be permanent, perhaps slowly returning to a baseline configuration as memories consolidate within other cortical circuits. The observed hysteresis could represent a network response protecting existing memories from catastrophic interference by adjusting the co-firing structure of learnt associations or forming redundant ones. This could also reflect retroactive encoding of recent experience, juxtaposing the current spatial reference frame with those encountered before. Further work should investigate the relationship between the encoded novel representation (e.g. CPP) and the consequent potential modification of a pre-existing memory more closely: how are individual novelty-induced neuronal motifs retroactively modifying the network co-firing structure, which represents past memories? Moreover, considering the SWR re-activations might be key to reveal how novel neuronal trajectories modify pre-existing neuronal associations, as low activity cells are more strongly engaged (see Fig. 4.3.6e-f; Grosmark and Buzsáki, 2016). Therefore investigating the role of resting and sleep seem crucial to obtain a deeper understanding of the integration of novel information within a pre-existing mnemonical structure (Dudai and Morris, 2013).

Together, these findings support the view of a division in computational labour within the log-normally distributed principal cell population for the discretization of memories of space and events within the hippocampus, allowing adaptive insertion and interaction of new information within a larger network of prior knowledge.

Chapter 5

Population and manifold analysis of large-scale hippocampal network activity

5.1 Introduction

In the recent years technological developments have allowed to perform recording of large-scale neuronal populations in multiple brain sites. Examples of such technology are silicon probes, which allow electrophysiological recording hundreds of neurons simultaneously and can be implanted in multiple regions, or brain imaging techniques of fluorescent proteins coupled with genetically-encoded neural activity indicators, such as calcium or voltage. Such volumes of data require analytical techniques that target the population dynamics and the interactions within the neuronal network interactions. To target the latter, in chapter 3 I presented a network science framework which allows capturing the structure of the interactions within the neuronal population. Another analytical frameworks that provide useful insights into the activity of large neural populations is dimensionality reduction, which refers to a variety of methods used to visualise and describe high dimensional data with low dimensional dynamics (see section 2.3.1; Cunningham and Yu, 2014). Such methods have been adopted by the manifold learning paradigm to represent and model neural dynamical systems. A manifold is a lower dimensional topological

space embedded within a higher-dimensional one, which has the property of being a linear subspace locally but it can otherwise have a non-linear geometry Such low-dimensional structures have been reported in the neural population dynamics of a variety of brain circuits and different behavioural tasks (Chaudhuri et al., 2019; Rubin, Sheintuch, et al., 2019). Manifold learning techniques have been used in many neuroscientific studies, such as in understanding neural mechanisms underpinning decision-making in prefrontal cortex (Mante et al., 2013; Harvey et al., 2012), movement preparation in premotor cortex (M. M. Churchland et al., 2012; Gallego et al., 2020; Feulner and Clopath, 2021), and more (Vyas et al., 2020). Manifold learning techniques and network science offer different but complementary approaches to the analysis of neural population activity data, with the former extracting dynamical trajectories of the neural population activity, while the latter preserves the individual neuron representation to characterise the structure of their interaction.

In this chapter I employ manifold learning techniques to analyse a two-photon calcium imaging datasets of hippocampal neurons as mice explore a circular environment. I aim to describe the representational space of the neural population by using the manifold learning approach to uncover low dimensional structure in the high dimensional neuronal activity.

5.2 Methods

5.2.1 Manifold learning methods

Manifold learning methods aim to uncover lower dimensional structure, referred to as *neural manifold*, within the high dimensional neural activity using dimensionality reduction techniques. That is, from the activity X of N neurons during the time interval T, a lower-dimensional representation Y is obtained, whose extracted

dimensions k are called *latent variables* (see Fig 5.1; Cunningham and Yu, 2014).

There are several types of manifold learning methods that can be divided into linear and nonlinear methods. Although they are similar in some ways, they may differ in the type of statistical structures or properties they capture and preserve. It is important to select which type of method is most suitable for different types of neural data, as this may have significant impact on the resulting scientific interpretations.

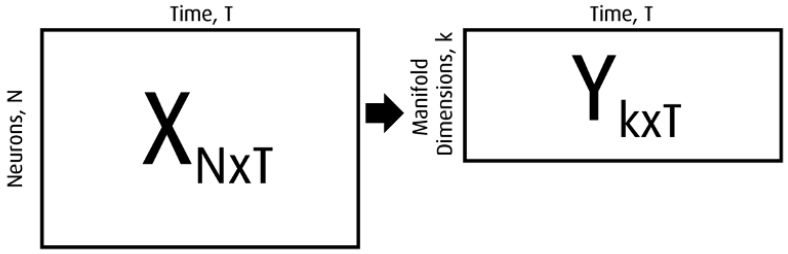

Figure 5.1: Dimensionality reduction schematic illustrating how the manifold learning paradigm transforms a high dimensional neural population activity matrix, X, with N neurons and T time points, into a lower dimensional representation within a manifold space of k dimensions.

Principal Component Analysis

One of the most common linear manifold learning methods is Principal Component Analysis (PCA). It is a linear dimensionality reduction technique that aims to reduce the number of variables of large data sets by transforming them into a smaller set of k latent variables, called the principal components (PCs). Geometrically speaking, PCs represent the directions of the data that explain a maximal amount of variance and they are constructed as linear combinations of the original variables. To obtain them, first the covariance matrix Q of the neural activity matrix X is computed as

$$\mathbf{Q} = \mathbf{X}\mathbf{X}^{\mathbf{T}}$$

and then eigendecomposition is applied

$$\mathbf{Q} = \mathbf{W}\mathbf{\Lambda}\mathbf{W}$$

The columns of $\mathbf{W}$ are then the resulting eigenvectors ($\mathbf{w_1}, ..\mathbf{w_N}$) are the directions of the axes that capture the most variance (i.e., PCs), and the corresponding eigenvalues (i.e, $\lambda_1, ...\lambda_N$ the diagonal elements of $\mathbf{\Lambda}$) yield the amount of variance carried by each PC. Then, by sorting the PCs with respect to their respective eigenvalues, the first k PCs are retained so that a set amount of variance in the original data is explained.

Multidimensional Scaling

Classical multidimensional scaling (MDS) is also a linear dimensionality reduction technique that aims to find a low-dimensional map of a number of objects (e.g. neural states) starting from the pairwise distances between them in the high dimensional space (J. B. Kruskal and Wish, 1978). In the case of neural data, given an $N \times T$ activity matrix, X, a $T \times T$ distance matrix, D, is first obtained using the Euclidean or a similar metric (in the analysis shown the cosine dissimilarity is used). A lower-dimensional mapping, $Y \in \mathbb{R}^{k \times T}$, where $k << N$, is then found by minimising a loss function, called strain, so that the mapped inter-point distances are as close as possible to the original distances in D. From the eigendecomposition of B, the double-centred distance matrix D, the components (i.e, dimensions) of classical MDS are revealed as the eigenvectors of B, while their respective eigenvalues report the amount of variance they explain.

Isomap

One of the most commonly used nonlinear dimensionality reduction algorithms is Isomap (Tenenbaum et al., 2000). Non-linear techniques aim to uncover the broader

non-linear structure of the neural manifold embedding of the neural population activity, X, by approximating the true topology of the neural manifold, Y. To do so, it first embeds X onto a weighted graph G, whose nodes represent the activity of the neuronal population at a given time x_t, and the edges between them represent links to network states $x_m, x_n, ...$ that are the most similar to x_t, i.e., its neighbours. The k-nearest neighbours algorithm is usually used to estimate the neighbours for all network states $x_1, ..., x_T$. These neighbouring relations are then encoded in a weighted graph with edges $d_X(i, j)$ between neighbouring states i, j that depends on the distance metric d_X used. G can then be used to approximate the true geodesic distances on the manifold $d_M(i, j)$ between any two points i, j (i.e. network states x_i, x_j) by measuring their shortest path length $d_G(i, j)$ in the weighted graph G using an algorithm such as Dijkstra's (Djikstra, 1959). Classical MDS is then applied to the matrix of distances within the graph $D_G = \{d_G(i, j)\}$ to yield an embedding of the data in a k-dimensional Euclidean space Y that best preserves the manifold's estimated geometry. The quality of the reconstructed manifold Y depends greatly on the size of the neighbourhood search and the distance metric used to build G.

Other nonlinear dimensionality reduction techniques include Locally Linear Embedding (LLE; Roweis and Saul, 2000) and Laplacian Eigenmaps (Belkin and Niyogi, 2003), which share a similar graphical approach as Isomap but aim to preserve only the local geometry of the data (i.e, only the distance between nearby points / neural states). These approaches can be more stable than Isomap but they may also distort the representation of the data. This can be crucial when the manifold embedding is to be used to make qualitative, but also quantitative, inferences about neural activity. In fact, preserving global distances within neural data is equivalent to considering all connections in a weighted graph, which, as discussed in chapter 3, ensures all the information is conserved but might include noise. Further

developments in local-geometry preserving methods have lead to the development of the t-distributed Stochastic Neighbour Embedding (t-SNE; Van Der Maaten and Hinton, 2008, which is considered the state-of-the-art algorithm for dimension reduction for visualization and clustering.

Uniform Manifold Approximation and Projection (UMAP)

Uniform Manifold Approximation and Projection (UMAP) is a nonlinear dimensionality reduction technique that is constructed from a theoretical framework based on topological data analysis, Riemannian geometry and algebraic topology. (Mcinnes et al., 2018). UMAP builds upon the mathematical foundations of LEM, Isomap and other nonlinear dimensionality techniques in that it uses a k-nearest neighbours weighted graphs representation of the data. By then using manifold approximation and patching together local fuzzy simplicial set representations, a topological representation of the high dimensional data is constructed. This layout of the data is then optimised in a low dimensional space to minimize the cross-entropy between the two topological representations. Compared to t-SNE, UMAP is competitive with it in terms of visualization quality and arguably preserves more of the global dataset structure with superior run time performance. Furthermore the algorithm is able to scale to significantly larger data set sizes than are feasible for t-SNE.

UMAP and t-SNE have recently also being employed for visualising high dimensional genomics data and some distortion issues have been raised (Chari et al., 2021). Although this problem is particularly apparent with t-SNE embedding, which tend to completely disregard the global structure of the data, any dimensionality reduction to few dimensions will inherently distort the topology of the high-dimensional data, as shown by the Johnson-Lindenstrauss Lemma (Johnson and Lindenstrauss, 1984). Genomics dataset, though, are intrinsically higher dimensional than the neural population activity on which manifold learning has been applied (Rubin, Sheintuch,

et al., 2019; Nieh et al., 2021), therefore reduction to just a few dimension is bound to produce distortions; but it is not the case where a few latent dimensions have shown to drive a neural population activity and explain its variability (Chaudhuri et al., 2019; M. M. Churchland et al., 2012; Gallego et al., 2020).

5.2.2 Manifold characterisation methods

In this section are listed the measures employed to describe and characterise the neural manifold embedding obtained from the neural population data.

Linear dimensionality

The linear dimensionality of the neural population activity can be estimated by counting the number of PCs needed to achieve a certain amount (90% here) of variance in the original data. A similar reasoning can be used with the dimensions found by MDS, even if the variance accounted for is not the raw activity matrix's but the one contained in the pairwise distance matrix (see 5.2.1).

Intrinsic dimensionality

To estimate the intrinsic dimensionality of the neural activity, for any given point in the high dimensional space (i.e, neural state), we calculated the number of neighbouring neural states within a sphere surrounding it as a function of the sphere's radius. The slope of the number of neighboring data points within a given radius on a log–log scale equals the exponent in k in the power law $N(r) = cr^k$, where N is the number of neighbours and r is the sphere radius. The slope k is then an estimate of the intrinsic dimensionality of the neural activity (Grassberger and Procaccia, 1983; Rubin, Sheintuch, et al., 2019; Nieh et al., 2021). In Fig 5.2 the intrinsic dimensionality estimator is applied to two simulated datasets.

This measure could also be applied to the low-dimensional manifold coordinates to

inspect the nonlinear geometry possibly uncovered by the manifold embedding (i.e, used with nonlinear manifold learning techniques).

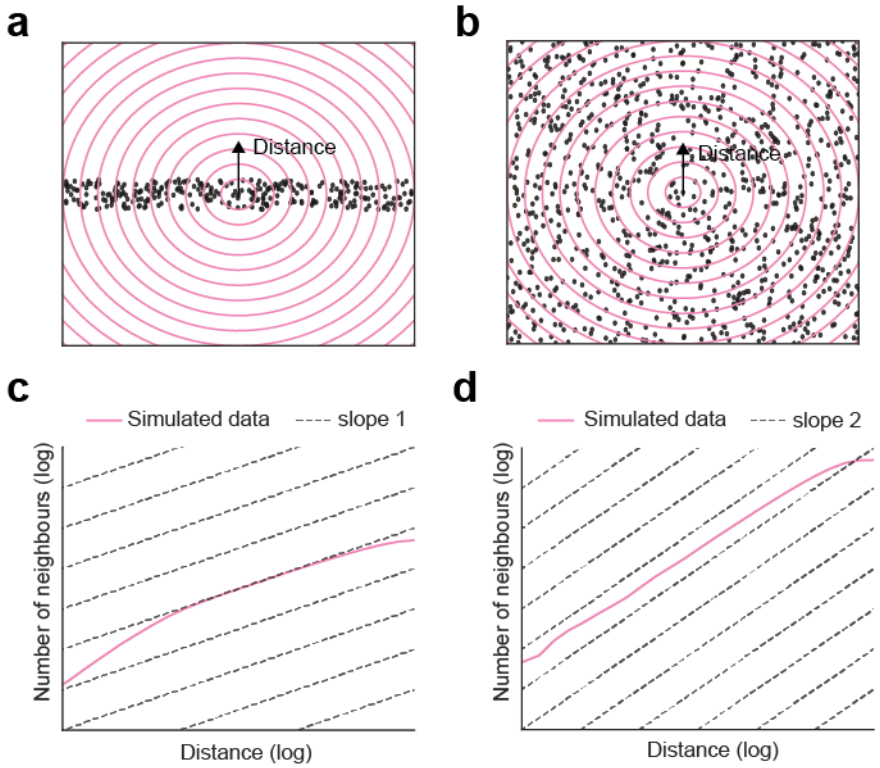

Figure 5.2: Intrinsic dimensionality estimation of a point cloud. **a-b**, Simulated data points, for 1-dimensional data **a** and for 2-dimensional data **b**. The red circles indicate different distances from a given data point. **c-d**, The average number of neighboring data points increases with the distance following a power law. The power is indicative of the internal dimension of the data. The number of neighboring data points increases linearly **c** or quadratically **d** with the radius for 1-dimensional and 2-dimensional data, respectively.

Optimal Linear Estimator (OLE) for behavioural decoding

To test the information content of the estimated hippocampal manifolds with any of the algorithm described above, I compute the decoding accuracy of the animal's angular position as a function of the number of manifold dimension using an Optimal Linear Estimator (OLE; Warland et al., 1997). This allows to assess the information content of the manifold's embedding and the number of dimensions necessary to encode the animal's position. I use a 10-fold cross-validation approach, training the decoder on 90% of the data and testing it on the remaining 10%. Given the testing data low dimensional manifold embedding $\hat{\mathbf{Y}}$ of the neural population activity and the mouse angular position $\hat{\boldsymbol{\phi}}$, the OLE reconstruction is given by The decoding performance is assessed by computing the Pearson correlation coefficient between the actual and reconstructed angular position for the test data.

Reconstruction of neural activity from low dimensional embedding

Another measure to evaluate the degree of fidelity of the manifold embedding to the recorded neural data is to quantify the reconstruction of the high dimensional neural data from the low dimensional embedding. To obtain such a mapping we employ the non-parametric regression method originally introduced for LLE (Roweis and Saul, 2000). So, given the manifold coordinates $\boldsymbol{Y} = \boldsymbol{y_1}, ..., \boldsymbol{y_T} \subset \mathbb{R}^{\boldsymbol{k}}$ representing the neural activity $\boldsymbol{X} = \boldsymbol{x_1}, ..., \boldsymbol{x_T} \subset \mathbb{R}^{\boldsymbol{N}}$, learn a mapping $\boldsymbol{g} : \mathbb{R}^{\boldsymbol{k}} \rightarrow \mathbb{R}^{\boldsymbol{N}}$ such that $\boldsymbol{g}(\boldsymbol{y_i})$ approximates $\boldsymbol{x_i}$ for all $\boldsymbol{i}$. To map a new point $\boldsymbol{y}$ from the manifold to the neural activity space, its $\boldsymbol{k}$ nearest neighbors $\boldsymbol{\eta_1}(\boldsymbol{y}), ..., \boldsymbol{\eta_k}(\boldsymbol{y}) \subset \boldsymbol{Y}$ are found, as measured by Euclidean distance in manifold space. $\boldsymbol{y}$ is then expressed as a weighted sum of its neighbors. Weights $\boldsymbol{w}(\boldsymbol{y})$ are found that minimize the squared reconstruction error plus an $\boldsymbol{l_2}$ regularization term that encourages small weights. Weights are constrained to sum to one, which makes them invariant to translation

of x and its neighbors (they are also invariant to rotation and scaling).

$$\boldsymbol{w(y) = \underset{w}{\operatorname{argmin}} \left\| y - \sum_{i=1}^{n} w_i \eta_i(y) \right\|^2 - \lambda \|w\|^2} \tag{5.1}$$

$$\text{s.t.} \qquad \boldsymbol{\sum_{j=1}^{k} w_i = 1}$$

A closed form solution to this optimization problem is described in.11. Let $\boldsymbol{G}$ denote the local Gram matrix:

$$\boldsymbol{G_{i,j} = (y - \eta_i(y)) \cdot (y - \eta_j(y))} \tag{5.2}$$

Let $\boldsymbol{I}$ denote the identity matrix and $\vec{\mathbf{1}}$ denote a vector of ones. The optimal weights can be found by solving the following equation and then rescaling the weights so that they sum to one.

$$\boldsymbol{(G + \lambda I)w = \vec{1}} \tag{5.3}$$

$\boldsymbol{y}$ is then mapped onto the neural activity space by applying the same weights to the known images of its neighbors in the original high dimensional space $\boldsymbol{\eta'_1(y), ..., \eta'_k(y) \subset X}$.

$$\boldsymbol{g = \sum_{i=1}^{n} w_i(y) \eta'_i(y)} \tag{5.4}$$

The number of neighbors $\boldsymbol{k}$ and the regularization parameter $\boldsymbol{l_2}$ are fixed and set to 10 and 1, respectively. This approach was inspired by Low et al., 2018.

I then obtain the reconstruction score by computing the Pearson correlation coefficient between the reconstructed and the original neural activity, to assess their similarity. To perform an element-wise comparison, the $\boldsymbol{N \times T}$ neural activity matrices are concatenated column-wise into a single vector and the correlation coefficient is calculated. Using 90% of the data from each session to train the reverse mapping $\boldsymbol{g}$, the reconstruction was then evaluated on the remaining 10% test data.

By then averaging across the 10 cross-validation folds, the reconstruction score is obtained.

5.3 Manifold analysis of hippocampal population activity in head-fixed mice navigating a floating real-world environment

5.3.1 Data and behavioural protocol

Head-fixed mice were trained to navigate the floating track system (Fig 5.3a) in the dark either along a 1D circular track or in a 2D circular open field and were tracked using an infrared system (see Go et al., 2021 for more details on the experimental setup). Mice were trained in the floating track system after viral injection and hippocampal window implantation. The similarity of their behavior to that observed in tethered and freely-moving mice is validation that the surgical procedures do not adversely affect behavior, consistent with previous reports (Fig 5.3b; Dombeck et al., 2010; Pilz et al., 2016). Greater numbers of animals were available at earlier than later stages of the experimental pipeline simply because of the requirement to pass successive criteria relating to behavioral performance, quality of preparation, GCaMP6s expression located in area of interest, and registration of ROIs over multiple sessions. For the analyses presented in this chapter, n=4 mice and n=6 trials are used for the 1D circular track and n=3 mice and n=3 trials for the 2D open field exploration.

To optically record the activity of CA1 neurons, mice were injected with an adeno-associated virus to express both the calcium indicator GCaMP6s and the static marker mRuby into the hippocampus. The animals then had the cortex overlying the hippocampus removed and were implanted with an imaging window.

Two-photon imaging (at 940 nm) through the hippocampal window 3 weeks later showed robust expression of both GCaMP6s and mRuby in a large population of CA1 neurons (Fig 5.3c). We primarily used the mRuby image to repeatedly identify the same cells across time.

Two-photon time-series videos of GCaMP6s fluorescence in the hippocampi of behaving mice were acquired. An automated algorithm (Giovannucci et al., 2019) was used to identify cells and extracts their activity from the GCaMP6s fluorescence changes ($\boldsymbol{\Delta}$F/F). 53–225 (median: 101) active neurons per FOV (330 $\times$ 330 $\boldsymbol{\mu}$m, 6 FOVs in 3 mice) were imaged for 12–28 min (see Fig. 5.3d showing 225 ROIs for the representative image shown in Fig. 5.3c). $\boldsymbol{\Delta}$F/F traces were extracted from the ROIs and displayed significant calcium transients (Fig 5.3e), which can be represented in the form of an $\boldsymbol{N} \times \boldsymbol{T}$ activity matrix, with $\boldsymbol{N}$ being the number of units and $\boldsymbol{T}$ the number of time samples (Fig 5.3f).

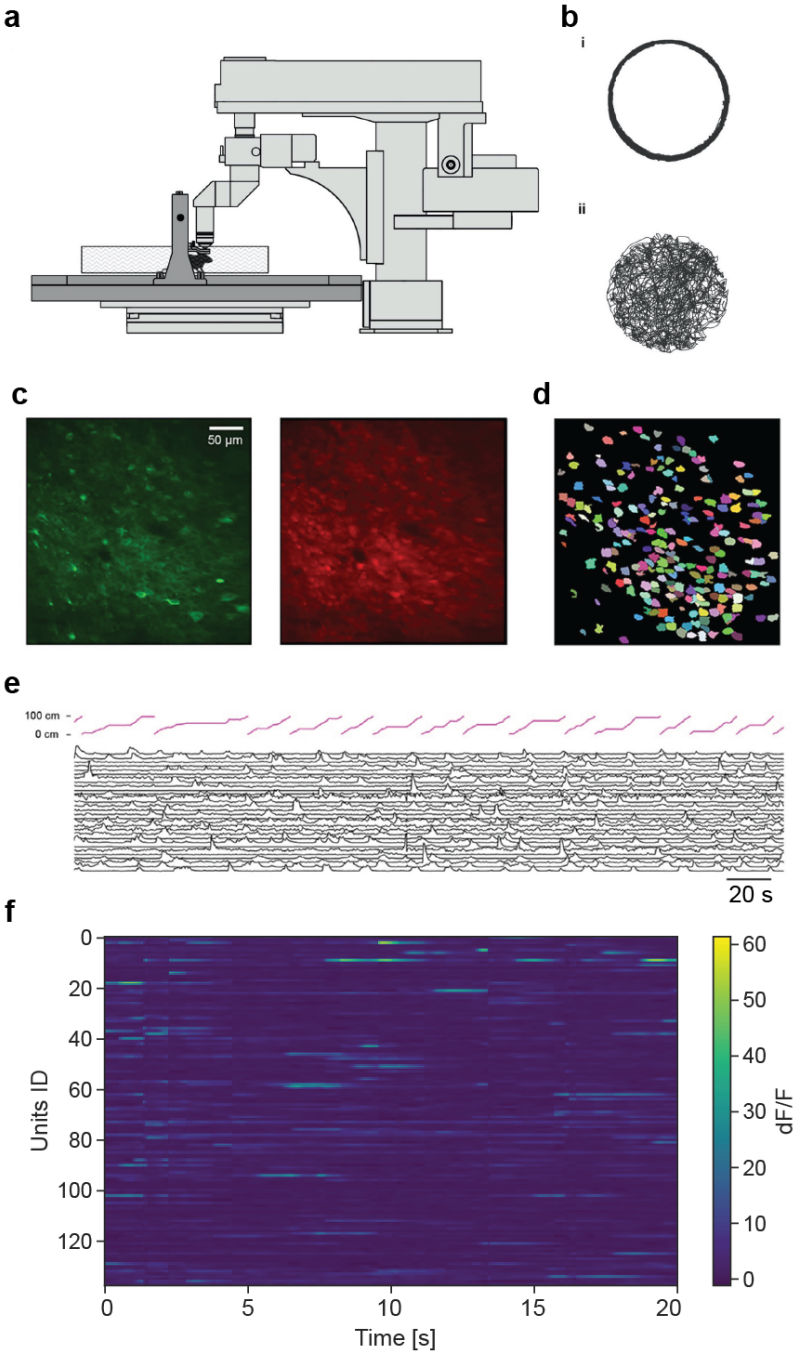

Figure 5.3: Floating real-world environment experimental set-up and data description. **a**, Schematic of experimental setup. Mouse is head fixed while navigating a floating track under a two-photon microscope (in light gray). **b**, Twenty minutes of spatial trajectories of head-fixed mice navigating (i) a circular track (1D) and (ii) a circular open field (2D). **c**, Two-photon images from a typical CA1 imaging session. Green: GCaMP6s, red: mRuby. **d** 225 segmented ROIs from image in **c**. **e**, Ca2+ transients for 30 (of 225) randomly selected cells from the region shown in **c**. Trace height is normalized to the 99th percentile of the $\mathbf{\Delta}$F/F for each cell. Magenta trace at top shows position of the mouse along the circular track **f**, An exemplar $\boldsymbol{N} \times \boldsymbol{T}$ activity matrix showing 20 seconds of neural activity from the recorded population. Panel **a** - **e** are taken with permissions from Go et al., 2021

5.3.2 Low dimensional embedding encode the animal spatial position

To study how spatial behavior on the air-lifted platform is reflected in neural population dynamics, I performed a neural manifold analysis using different algorithms described in section 5.2.1. Applying this to data recorded from mice running on the 1D circular track revealed the distinct laps of the animal's spatial trajectory in the low-order components of the neural manifold (typical session example shown in Fig. 5.4). Such circular topology was revealed using all the algorithms tested (intrinsic dimensionality: PCA, ; MDS, ; Isomap, ; UMAP,), but it was perhaps captured best by the UMAP embedding (Fig. 5.4d), which clearly displays the separate circular laps of the neural population activity and had the lowest intrinsic dimensionality. The open field exploration, being less constrained, unsurprisingly revealed more complex dynamics on the manifold (Fig. 5.5). Color-coding the neural population activity (i.e., the points on the visualisations in Figs. 5.4 and 5.5) by the animal's angular position in the 2D circular open field arena revealed some clustering of points on the manifold, without however an homogeneous mapping but instead rather spread throughout the manifold (Fig. 5.5a). Color-coding instead for the animal's radial position revealed additional structure at larger scales (Fig. 5.5b), as well as for the passage of time within the session, perhaps highlighting the neural drifting dynamics (Fig. 5.5c; see Mau, Hasselmo, et al., 2020). By quantifying the variance in the neural population dynamics accounted for by the manifold dimensions of the linear MDS embedding, it revealed that fewer components (dimensions) are needed to account for a fixed amount of variance for mice exploring the 1D circular track compared to the 2D open-field (Fig. 5.6a). Similarly, considering the number of components required to account for a fixed percentage (90%) of the variance as the linear dimensionality of the manifold (see section 5.2.2; Stringer et al., 2019), it grew with the number of

neurons incorporated within an ensemble. This grew at a faster rate with ensemble size for the 1D circular track than for the 2D open-field environments (Fig. 5.6b). A similar result was obtained by computing the intrinsic dimensionality of the two neural datasets as the gradient of the cumulative neighbouring neural states as a function of the distance between them in the high-dimensional neural space (see section 5.2.2; Nieh et al., 2021). The neural activity evoked by the 1D circular track exploration displayed a slightly lower intrinsic dimensionality than the one evoked by the 2D open field exploration (Figs. 5.6c,d; dataset dimensionality: 1D, $\mathbf{2.70 \pm 0.17}$; 2D, $\mathbf{3.30 \pm 0.04}$), suggesting that the greater complexity of the exploration trajectory and behaviour was recapitulated in higher-dimensional neural population dynamics. Additionally, I computed the reconstruction score using the highly nonlinear UMAP embedding of the neural population activity during the 1D and 2D explorations to assess the amount of neural activity variance that could be recovered from the low dimensional embedding using a nonlinear reverse mapping (see section 5.2.2). I found that only around 3 manifold dimensions were needed to obtain an optimal reconstruction, but this latter score was higher for the neural activity induced by the 1D than the 2D exploration, again suggesting that the neural activity was low dimensional in both datasets but yielded higher complexity during the 2D exploration (Fig 5.6e). Finally, I assessed the extent to which spatial information could be decoded from low-dimensional neural manifolds, by training an Optimal Linear Estimator (OLE) decoding algorithm on the angular position data. Angular position could be decoded with high accuracy from a very small number of components in the circular track case (Fig 5.6f); in comparison, decoding of angular position in the open-field task yielded lower fidelity estimates, and required more manifold dimensions.

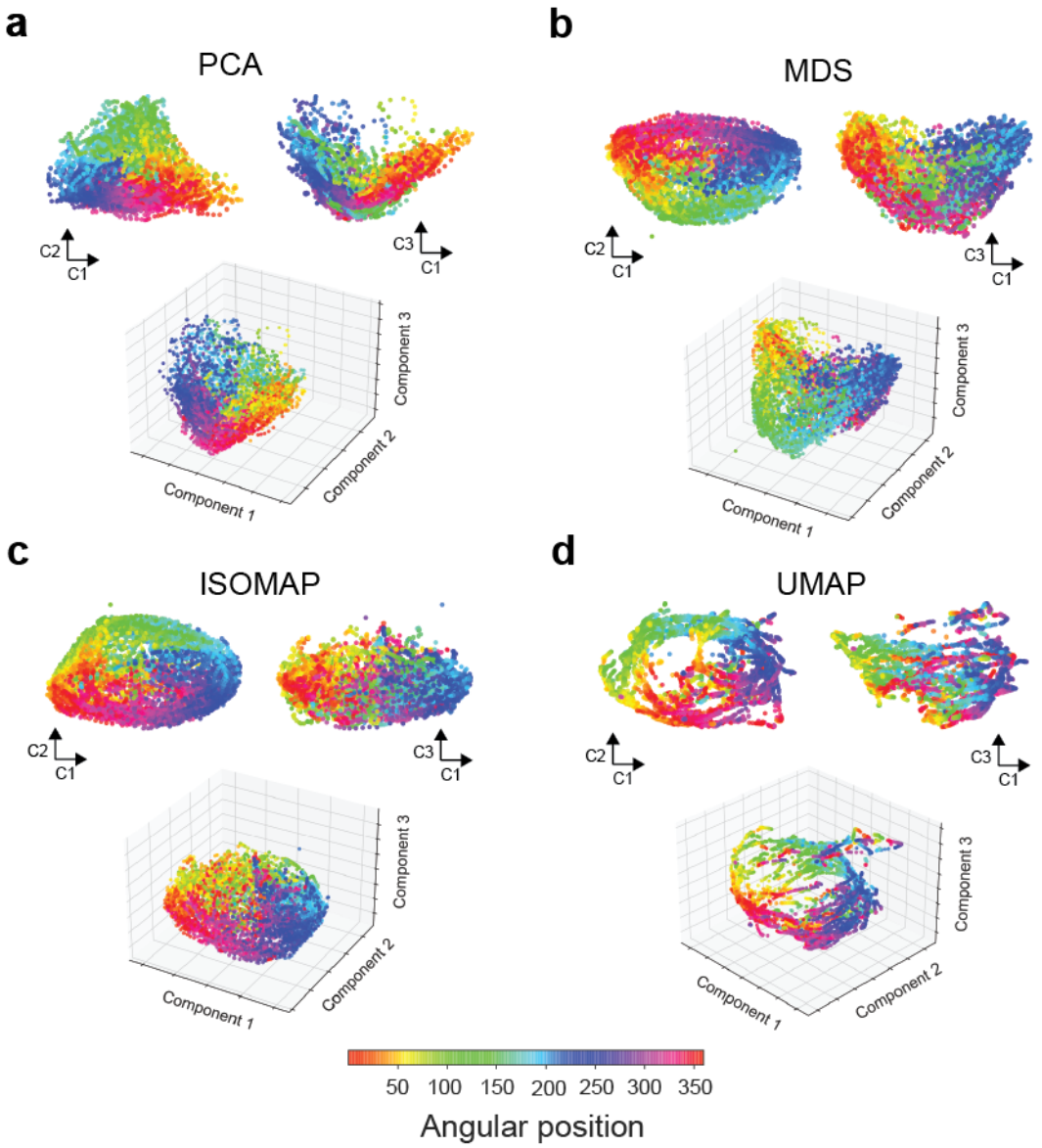

Figure 5.4: Manifold embedding of neural activity during circular track 1D exploration. **a**, An exemplar neural population activity embedding using the PCA algorithm. **b**, The same neural population activity is embedded using the MDS algorithm. **c**, The same neural population activity is embedded using the ISOMAP algorithm. **d**, The same neural population activity is embedded using the UMAP algorithm. These analyses show that the angular position of the mouse is encoded by the hippocampal neural activity.

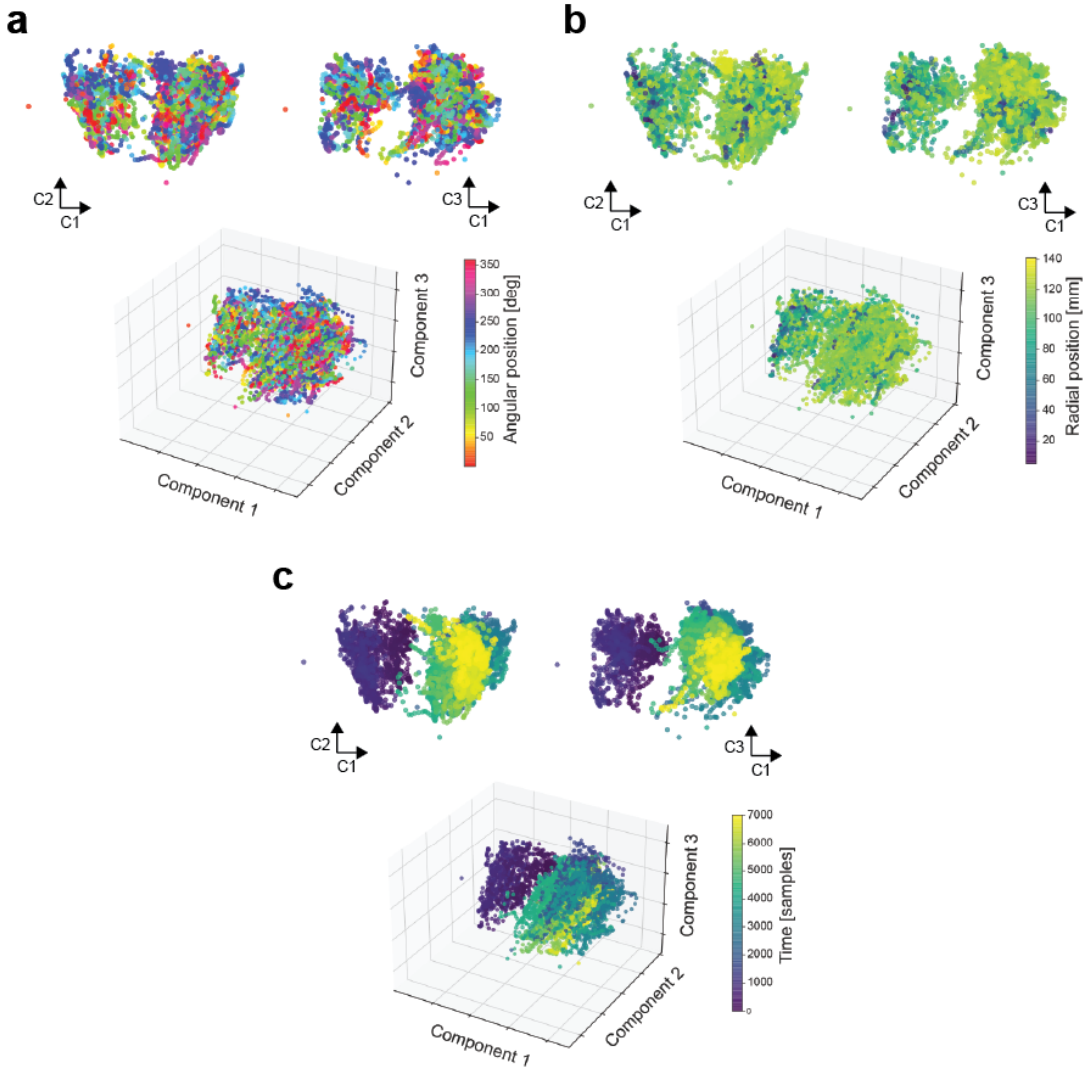

Figure 5.5: Manifold embedding of neural activity during open field 2D exploration. **a**, An exemplar neural population activity embedding using the MDS algorithm color-coded with respect to the angular position of thew mouse in the arena. **b**, The same manifold embedding is color-coded with respect to the radial position of the mouse in the arena. **c**, The same manifold embedding is color-coded with respect to the exploration time. These analyses show that the neural population activity is encoding multiple variables.

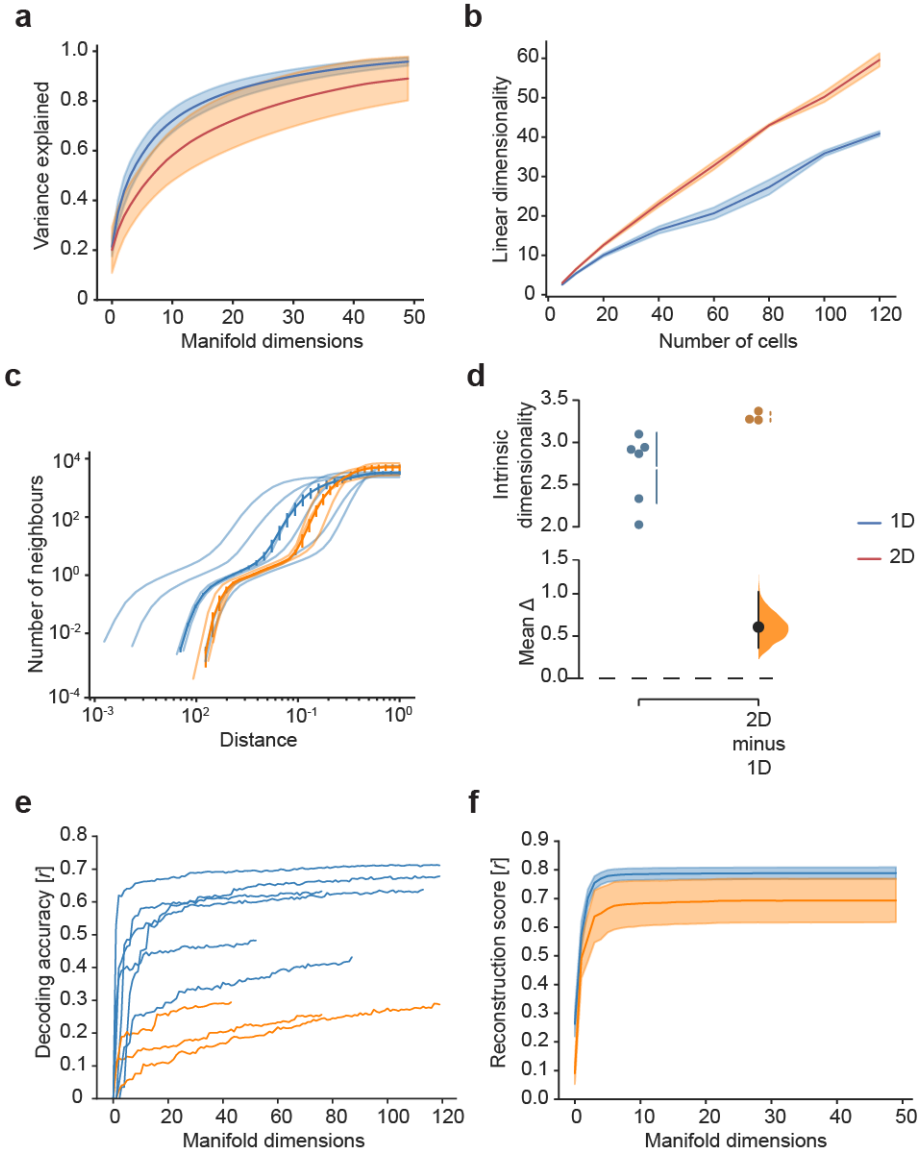

Figure 5.6: Open field exploration induces more complex dynamics in the neural population activity. **a**, The variance explained by inclusion of an increasing number of manifold dimensions for the 1D circular track and 2D open field environments. **b**, The growth of linear dimensionality, defined as the number of components needed to capture 90% of the variance, with the number of cells included in the manifold. **c**, The intrinsic dimensionality of the population activity is obtained from the high-dimensional neural representation for both the 1D circular track and the 2D open field datasets. **d**, The difference in dimensionality between the two datasets is presented using a Cumming estimation plot to visualize the effect size; top panel: vertical lines, SEM; bottom panels: black dot, median; black ticks, 95% confidence interval; filled curve: sampling error. **e**, Decoding performance of the animal's angular position, measured by Pearson correlation coefficient ($\boldsymbol{r}$), as a function of the number of MDS embedding dimensions, for circular track and open field environments. **f** The reconstruction score of the neural population activity with respect to the number of manifold dimensions used.

5.4 Discussion

I used manifold learning approaches to uncover the dynamics and the topology of neural population activity in the hippocampal CA1 region of mice exploring either a circular linear track or open-field arena. We tested four algorithms (PCA, MDS, Isomap, UMAP; see Fig. 5.4) and we found that UMAP seemed to qualitatively capture the best representation of the neural activity recorded during the circular linear track exploration, as the behavioural trajectory is clearly captured together with a mild neural drift (Fig. 5.4d). Any manifold learning algorithm, though, uncovers a similar topology, which suggest that a robust spatial tuning is present in the linear track exploration and is dominating the hippocampal network activity. The angular position of the mouse in the 1D task was visually apparent in the lowest dimensions of the neural manifold; while this was less immediately obvious in the 2D task (because of the non-cyclical nature of the exploratory trajectory, see Fig 5.5a), a decoding analysis indicated that for the open field task spatial location could still be decoded with some success from a relatively small number of manifold dimensions, although with much less fidelity (see Fig. 5.6e). On the other hand, within the 2D exploration evoked manifold more behavioural variable seemed, such as radial position and the passing of time (or perhaps neural drift?) seemed to be coded (see Fig. 5.6b,c). Furthermore, estimation of both linear and intrinsic dimensionality (see Fig. 5.6b-d), together with the amount of neural population activity variance captured (see Fig. 5.6a,e), revealed that the neural activity evoked by the 2D exploration displays a higher complexity and dimensionality than the one evoked by the 1D exploration, as might be expected given the more constrained nature of the task.

As shown in this chapter, population approaches to the study of the activity within neural circuits have the potential to intuitively represent its complex dynamics

and may reveal unseen or unexpected behavioural correlates. Quantifying the dimensionality of neural activity can give us insights into the type of computations employed by the underlying network: a higher dimensional representation allows a simple linear readout to generate a large number of potential responses, while a low dimensional representation grants consistency and generability over different contexts (Fusi et al., 2016). A varying neural activity dimensionality is supported by mixed selectivity neurons: cells that respond to different stimuli features together, depending on the contexts (this is particularly true for, but not limited to, prefrontal and parietal cortices neurons; see Raposo et al., 2014; Mante et al., 2013; McKenzie, A. J. Frank, et al., 2014; Basso et al., 1998). Compared to the hypothesis of highly specialised neurons as the core of brain processing (see section 2.3.1), mixed selectivity allows the brain to perform order of magnitudes more demanding computations needed to support cognition and complex behaviour (Rigotti et al., 2013). Such a perspective is fully embraced by the manifold learning approach: the single neuron attributes are lost to instead highlight the ensembles dynamics, which can share the inputs of individual units, that underlie neural representations (Vyas et al., 2020).

This is a complementary view to the one offered by network science methods (see chapter 3), which preserve the information about the single neurons identity to describe and model their interactions and their role in the network. Such circuit level analysis can yield important insights into the mechanisms that underlie neural computation but are difficult to relate directly to external behaviour (Humphries, 2018). Manifold learning approaches, instead, yield a potentially higher level interpretation of the neuronal network dynamics, which can be more closely related to behaviour (Barack and Krakauer, 2021).

Chapter 6

Conclusion and outlook

6.1 Summary and General Discussion

The main aim of this PhD thesis was to investigate the network-level mechanism that underpin the formation and continuous modification of memories. By combining network science methods and complex system analysis, I presented a framework for the analysis of the activity arising within neuronal networks, focusing on the hippocampal circuit. Using this framework, I was able to track and characterise the co-activity structure of the dCA1 principal cells network, arising from the precise temporal neuronal spiking within it, as mice performed an associative memory (CPP) task. This analysis revealed that the co-firing patterns representing an already familiar environment were modified by the encoding of novel place-reward association memories, suggesting the presence of hysterical dynamics in the network. Therefore this points to a potential mechanism underlying the retroactive modification of a previous representation in light of new information.

Moreover, I noticed that the encoding of mnemonic information onto neuronal co-firing patterns unraveled along distinct functional axes in the network co-firing activity space. These axes were found, firstly, to segregate novel from familiar environments, secondly to distinguish the individual behavioural events within

the novel environment, and finally to highlight the interaction between the new mnemonic information and the pre-existing familiar representation.

Finally, I observed that the heterogeneous population of dCA1 principal cells supported the co-firing mechanism just described. High activity units, biased towards the dCA1 deep pyramidal layer, quickly distinguished the familiar from the novel environment, giving rise to the core representation of each memory. Instead, low activity cells, biased towards the superficial pyramidal layer, joined co-firing motifs "on demand" throughout each task event, enabling cross-memory interactions. These findings shed light on an organizational principle of brain networks where high and low activity cells take part to the network coactivity motifs differently, forming the building blocks for flexible integration and interaction of memories.

As a final contribution, I used manifold learning and related approaches to uncover the populations dynamics within hippocampal CA1 as mice performed different types of exploration. Neuronal network population activity evoked by the 2D circular open field exploration resulted more complex than the one evoked by the 1D circular linear track, revealing a higher dimensionality and variance to explain via manifold learning methods. Such methods, then yield an intuitive representation of neuronal network activity, unveiling neural states that can provide direct insights into behaviour and neural computations.

6.1.1 Network science and neural population dynamics approaches to track neural population activity

As described in section 2.4 of this thesis, neuronal networks are composed by a diverse cellular population with wide, skewed activity distributions. The activity dynamics arising from these circuits are emergent properties of the wiring within them, both physical and functional. Using graph-theoretical tools, network science

can indeed be used to describe the former, obtaining insights into the mapping from wiring to dynamics (Lee et al., 2016; Schröter et al., 2017), as well as the latter, since the activity dynamics are constrained by the underlying physical connections but they can change much faster (e.g. neuromodulators (Nadim and Bucher, 2014)). Network science thus allows capturing the changes in the moment-to-moment activity structure of neuronal networks. By combining graph theory with complex system theory, in chapter 3 I have developed a network scientific framework for the analysis of co-activity patterns within neuronal networks.

Manifold learning approaches also offer an alternative view onto neuronal networks activity, by extracting the low dimensional population level dynamics that underpin behavioural correlates and cognitive computations (Vyas et al., 2020). Such low dimensional structures have been reported in the neural population dynamics of a variety of brain circuits and different behavioural tasks (see Figs 5.4 - 5.6; Mante et al., 2013; Chaudhuri et al., 2019; Rubin, Sheintuch, et al., 2019).

Both network science and manifold learning approaches offer powerful, complementary views of complex neural dynamics. The two approaches share the starting point of a pairwise interaction matrix representation of the data (being the covariance matrix in the case of PCA). Therefore, both methods assume that the relationships between neurons are stable over the interval of time analysed. Manifold learning approaches allow to qualitatively track and visualise the fine-grained trajectories of the population dynamics, but often they do not offer a clear mapping between the identified dimensions and the underlying neuronal population – it is especially the case for non-linear dimensionality reduction techniques (see section 5.2.2). This latter limitation can then become an advantage of manifold learning techniques because by extracting population level dynamics the unveil higher level neural representations that can be closely related to behaviour (see Figs 5.4 - 5.5). In fact, it is also pos-

sible to identify activity landscapes shared by different populations of neurons and individuals performing the same task (Gallego et al., 2020; Nieh et al., 2021), and how the geometry of such manifold constraints both learning and behaviour (Sohn et al., 2019; Feulner and Clopath, 2021). Furthermore, extracting low-dimensional structure from a high dimensional data can help in removing noise but can also remove useful information. On the other hand, network representations capture the structure of the interaction (co-firing) across all pairs of neurons, potentially including information discarded by dimensionality reduction methods. Moreover, network science enables the quantitative analysis of neural population activity, yielding simple variables describing its structure (Figures 3.1, 4.1.1 and 4.1.3). The presence of null models, such as small-world or random networks, allow us to make theory-driven hypothesis and compare them with experimental results (Fig. 3.2). The interpretation of some graph-theoretical variables, however, is not straightforward, as it is visualising population activity trajectories or drawing qualitative conclusions on neural states and their potential higher level correlates (Humphries, 2018; Barack and Krakauer, 2021). Therefore combining network science and manifold learning approaches could offer complementary insights into the activity of neural populations (Bruno et al., 2017). One such application of manifolds techniques could be the tracking neuronal motifs and trajectories induced by novelty encoding to investigate their effect on the pre-existing neuronal coactivity structure and its potential consequent retroactive modification, as discussed in section 4.4.

6.1.2 The role of co-activity within neuronal networks

The network science approach just discussed enabled me to investigate the co-firing topology of dCA1 principal cells network in mice performing different tasks. Even though there is evidence suggesting that the hippocampus is characterised by sequential activity (Buzsáki and Llinás, 2017), using the symmetric Pearson correlation coefficient measure to describe the co-firing interaction within the dCA1

circuitry yielded similar insights as employing a directional, biophysically inspired measure (Billeh et al., 2014). In fact, since both measures revealed the same results shown in Fig. 4.1.1 and Fig. 4.1.2, I decided to employ the simpler representation as it allowed for more interpretable results and the use of Riemmanian topological methods (see section 3.3). This result may imply that a directional representation is not needed to capture the learning-related network co-activity dynamics reported in section 4.3.1.

In the four datasets analysed in chapter 4 (*Novel context only*, *SPP*, *CPP* and *Familiar context with reward*; see section 4.2.1 and the caption of Fig. 4.1.3) we found that learning was accompanied by an increase in co-activity within the network. This is reflected in the increase in co-firing strength, geodesic path length and clustering coefficient observed in the weighted network representations (Fig. 4.1.1f and Fig. 4.1.3). This increase in co-activity could be the result of a general mechanism underpinning the encoding of new information. It is not simply explained by the passage of time (Fig. 4.1.3), even though there are experimental observations reporting that during waking the hippocampal neurons' log-normal distributions of firing rates widens, which could lead to an increase in the co-activity within the network (Watson et al., 2016; Buzsáki, 2019). Measures such as the neuron's population coupling (i.e., the tendency of a individual cell to follow the population activity; see Okun et al., 2015) and the sparseness of their neural representation (Rolls and Treves, 1990; Rolls and Tovee, 1995) could yield further insights towards the mechanism underpinning this phenomenon.

The co-firing "topological hysteresis" reported in the CPP task (Fig. 4.1.1f) is explained by the involvement of the low-activity cells in the network representation during the re-exposure session (Fig. 4.3.6). Their persistent co-firing perhaps returns to baseline with the successive sleep thanks to the homeostatic processes that

are active then (e.g. resetting the population log-normal distribution of firing rates; Watson et al., 2016; Levenstein et al., 2017; Peyrache et al., 2011). The heightened co-firing could, perhaps, be a network response to protect existing memories from catastrophic interference by adjusting the structure of learnt associations or forming redundant ones. This could also reflect the dynamic process of retroactively encode recent experience, juxtaposing the current spatial reference frame with those encountered before. Investigating the role of sleep and SWR re-activation in the re-modelling of pre-existing neuronal representation might be crucial, as discussed in section 4.4.

6.1.3 Different role of hippocampal principal cells within memory schemas

Although a substantial amount research has shown that "stable" engrams cells underpin memory retrieval (Tonegawa et al., 2015), it is agreed that some degree of plasticity is needed to ensure the integration of new information. The work in this thesis suggest that taking in novel mnemonic items can induce enduring changes on pre-existing memories (see Figures 4.1.1, 4.2.1, and 4.3.1), which is in agreement with previous studies showing that learning can modify the initial state of the network when retrieving familiar information (Dupret et al., 2010; McKenzie, Robinson, et al., 2013; Grewe et al., 2017). Moreover, the results in section 4.3.3 suggest that high activity cells readily form the neural backbone of memories, which can then be built upon and modified by the low activity cells to obtain finer representations (see Fig 4.3.6d). This mechanism could constitute the physiological basis for memory schemas within the hippocampal circuitry, which could enable the rapid formation of novel memories on top of a common mnemonic framework (see section 2.1.2; Tse et al., 2007; McKenzie, A. J. Frank, et al., 2014). Similar functional heterogeneity within the dCA1 has already been reported, on one hand highlighting the role of the plastic subset of principal cells

in encoding new information on top of networks dynamics mainly driven by the fast-firing subset (Grosmark and Buzsáki, 2016), and on the other describing the functional differences across the principal cells within the dCA1 superficial and deep pyramidal layer (see Fig. 4.3.2; Cembrowski and Spruston, 2019; Danielson et al., 2016; Soltesz and Losonczy, 2018). Such diversity could be key to the interleaved learning hypothesis which portrays the acquisition of new information as a lasting process impacting the future computations of mnemonic systems (Kumaran et al., 2016).

Such neuronal ensembles yielding dynamic representations would have the effect of deteriorating the "tuning" of neuronal populations relative to the external world, explaining many neural instability observations (Ziv et al., 2013; Rubin, Geva, et al., 2015; Mau, Sullivan, et al., 2018; Driscoll et al., 2017). That would imply that even though the neuronal motifs related to external stimuli are not long-lasting, the internal mappings across neurons persist through time, possibly due to compensatory adaptation mechanisms at the network level (e.g. neural drift; Kinsky, Sullivan, et al., 2018; Rule et al., 2020; Gonzalez et al., 2019). This hypothesis is consistent with the internal "reader" neurons (or assemblies, regions) view introduced in section 2.3.2, which highlights the importance of the temporally precise co-activity patterns for neural representations (Buzsáki, 2010). With this thesis I propose, in fact, that a possible mechanism for the integration of new information within a body of pre-existing memories is a coordinated change in the co-firing between the heterogeneous population of dCA1 principal cells.

6.2 Outlook

Neural computations and its emerging representations are composed by the temporally precise and coordinated firing patterns of thousands of neurons. While the

rapid advances in neural recording technology, now scaling to hundreds or thousands of simultaneously recorded neurons (Stevenson and Kording, 2011; Stringer et al., 2019), enable us to capture the computations underpinning complex processes such as memory formation and manipulation, we need to have the right analytical tools to describe them. In this thesis I have developed a network science framework to analyse the co-firing structure of principal cells within the hippocampal dCA1 network, which underpins memory representations. In this way I was able to describe the co-firing network mechanism that accompanies the integration of new information into pre-existing memories, highlighting the importance of the labor diversity of the hippocampal principal cell population that supports this process.

Future developments should attempt to integrate the network science framework, presented in chapter 3, with the manifold learning approach, presented in chapter 5. I believe the two analytical methods are strongly complementary; while network science allows to represent the structure and the neuron-wise patterns of the activity within neuronal networks, the manifold analysis aims to extract the dynamics generated within the network using a population representation. Therefore, network science can be used to find the cellular framework underlying the lower-dimensional activity patterns uncovered by manifold analysis, which may reveal higher order representations of the neural dynamics that are directly comparable to cognitive computations and behaviour (Vyas et al., 2020; Barack and Krakauer, 2021). This compound approach would facilitate the description of complex neuronal population dynamics and its association to behavioural and internal variables processed by the network, possibly uncovering previously overseen ones.

Regarding the hippocampal dCA1 network co-firing mechanisms that accompany the integration of novel information into a body of pre-existing memories, I believe an important next step would be to causally test the labour diversity of the hetero-

geneous population of principal cells. Both deep and superficial cells have distinct genetic profiles (Cembrowski and Spruston, 2019) that allow selective genetic tagging of the two subpopulations. Because of that, the two group of cells can be optogenetically targeted separately to investigate their respective roles in memory formation and consolidation. The former can be approached with a theta-oscillation-targeted silencing, while the latter with a SWR-targeted silencing in the sleep section subsequent to exploration (Ven et al., 2016). This next step can lead to deeper insights into the temporally precise circuit mechanism that underpins memory formation and integration within the hippocampal circuit.

Appendix

Throughout this thesis some figures are taken from published papers, all of which are cited in the captions. Specifically, the figures shown in chapter 4 are all taken from a scientific publication of which I am the first author, and some figures in chapter 5 are also taken from a publication of which I am an author.

SPRINGER NATURE LICENSE
TERMS AND CONDITIONS

Jul 13, 2021

This Agreement between Imperial College London -- Giuseppe Pietro Gava ("You") and Springer Nature ("Springer Nature") consists of your license details and the terms and conditions provided by Springer Nature and Copyright Clearance Center.

License Number	5107040059241
License date	Jul 13, 2021
Licensed Content Publisher	Springer Nature
Licensed Content Publication	Nature Reviews Neuroscience
Licensed Content Title	The log-dynamic brain: how skewed distributions affect network operations
Licensed Content Author	György Buzsáki et al
Licensed Content Date	Feb 26, 2014
Type of Use	Thesis/Dissertation
Requestor type	academic/university or research institute
Format	electronic
Portion	figures/tables/illustrations
Number of figures/tables/illustrations	2
High-res required	no
Will you be translating?	no

Circulation/distribution	1 - 29
Author of this Springer Nature content	no
Title	Network analysis of the cellular circuits of memory
Institution name	Imperial College London
Expected presentation date	Oct 2021
Portions	Figures 3 and 6
Requestor Location	Imperial College London Flat 4 224 Uxbridge road London, County W127JD United Kingdom Attn: Imperial College London
Total	0.00 USD

Terms and Conditions

Springer Nature Customer Service Centre GmbH
Terms and Conditions

This agreement sets out the terms and conditions of the licence (the **Licence**) between you and **Springer Nature Customer Service Centre GmbH** (the **Licensor**). By clicking 'accept' and completing the transaction for the material (**Licensed Material**), you also confirm your acceptance of these terms and conditions.

1. Grant of License

1. 1. The Licensor grants you a personal, non-exclusive, non-transferable, world-wide licence to reproduce the Licensed Material for the purpose specified in your order only. Licences are granted for the specific use requested in the order and for no other use, subject to the conditions below.

1. 2. The Licensor warrants that it has, to the best of its knowledge, the rights to license reuse of the Licensed Material. However, you should ensure that the material you are requesting is original to the Licensor and does not carry the copyright of another entity (as credited in the published version).

1. 3. If the credit line on any part of the material you have requested indicates that it was reprinted or adapted with permission from another source, then you should also

seek permission from that source to reuse the material.

2. Scope of Licence

2. 1. You may only use the Licensed Content in the manner and to the extent permitted by these Ts&Cs and any applicable laws.

2. 2. A separate licence may be required for any additional use of the Licensed Material, e.g. where a licence has been purchased for print only use, separate permission must be obtained for electronic re-use. Similarly, a licence is only valid in the language selected and does not apply for editions in other languages unless additional translation rights have been granted separately in the licence. Any content owned by third parties are expressly excluded from the licence.

2. 3. Similarly, rights for additional components such as custom editions and derivatives require additional permission and may be subject to an additional fee. Please apply to Journalpermissions@springernature.com/bookpermissions@springernature.com for these rights.

2. 4. Where permission has been granted **free of charge** for material in print, permission may also be granted for any electronic version of that work, provided that the material is incidental to your work as a whole and that the electronic version is essentially equivalent to, or substitutes for, the print version.

2. 5. An alternative scope of licence may apply to signatories of the STM Permissions Guidelines, as amended from time to time.

3. Duration of Licence

3. 1. A licence for is valid from the date of purchase ('Licence Date') at the end of the relevant period in the below table:

Scope of Licence	Duration of Licence
Post on a website	12 months
Presentations	12 months
Books and journals	Lifetime of the edition in the language purchased

4. Acknowledgement

4. 1. The Licensor's permission must be acknowledged next to the Licenced Material in print. In electronic form, this acknowledgement must be visible at the same time as the figures/tables/illustrations or abstract, and must be hyperlinked to the journal/book's homepage. Our required acknowledgement format is in the Appendix below.

5. Restrictions on use

5. 1. Use of the Licensed Material may be permitted for incidental promotional use and minor editing privileges e.g. minor adaptations of single figures, changes of format, colour and/or style where the adaptation is credited as set out in Appendix 1 below. Any other changes including but not limited to, cropping, adapting, omitting material that

affect the meaning, intention or moral rights of the author are strictly prohibited.

5. 2. You must not use any Licensed Material as part of any design or trademark.

5. 3. Licensed Material may be used in Open Access Publications (OAP) before publication by Springer Nature, but any Licensed Material must be removed from OAP sites prior to final publication.

6. Ownership of Rights

6. 1. Licensed Material remains the property of either Licensor or the relevant third party and any rights not explicitly granted herein are expressly reserved.

7. Warranty

IN NO EVENT SHALL LICENSOR BE LIABLE TO YOU OR ANY OTHER PARTY OR ANY OTHER PERSON OR FOR ANY SPECIAL, CONSEQUENTIAL, INCIDENTAL OR INDIRECT DAMAGES, HOWEVER CAUSED, ARISING OUT OF OR IN CONNECTION WITH THE DOWNLOADING, VIEWING OR USE OF THE MATERIALS REGARDLESS OF THE FORM OF ACTION, WHETHER FOR BREACH OF CONTRACT, BREACH OF WARRANTY, TORT, NEGLIGENCE, INFRINGEMENT OR OTHERWISE (INCLUDING, WITHOUT LIMITATION, DAMAGES BASED ON LOSS OF PROFITS, DATA, FILES, USE, BUSINESS OPPORTUNITY OR CLAIMS OF THIRD PARTIES), AND
WHETHER OR NOT THE PARTY HAS BEEN ADVISED OF THE POSSIBILITY OF SUCH DAMAGES. THIS LIMITATION SHALL APPLY NOTWITHSTANDING ANY FAILURE OF ESSENTIAL PURPOSE OF ANY LIMITED REMEDY PROVIDED HEREIN.

8. Limitations

8. 1. ***BOOKS ONLY:***Where **'reuse in a dissertation/thesis'** has been selected the following terms apply: Print rights of the final author's accepted manuscript (for clarity, NOT the published version) for up to 100 copies, electronic rights for use only on a personal website or institutional repository as defined by the Sherpa guideline (www.sherpa.ac.uk/romeo/).

8. 2. For content reuse requests that qualify for permission under the STM Permissions Guidelines, which may be updated from time to time, the STM Permissions Guidelines supersede the terms and conditions contained in this licence.

9. Termination and Cancellation

9. 1. Licences will expire after the period shown in Clause 3 (above).

9. 2. Licensee reserves the right to terminate the Licence in the event that payment is not received in full or if there has been a breach of this agreement by you.

Appendix 1 — Acknowledgements:

For Journal Content:
Reprinted by permission from [**the Licensor**]: [**Journal Publisher** (e.g. Nature/Springer/Palgrave)] [**JOURNAL NAME**] [**REFERENCE CITATION** (Article name, Author(s) Name), [**COPYRIGHT**] (year of publication)

For **Advance Online Publication papers:**
Reprinted by permission from [**the Licensor**]: [**Journal Publisher** (e.g. Nature/Springer/Palgrave)] [**JOURNAL NAME**] [**REFERENCE CITATION** (Article name, Author(s) Name), [**COPYRIGHT**] (year of publication), advance online publication, day month year (doi: 10.1038/sj.[JOURNAL ACRONYM].)

For Adaptations/Translations:
Adapted/Translated by permission from [**the Licensor**]: [**Journal Publisher** (e.g. Nature/Springer/Palgrave)] [**JOURNAL NAME**] [**REFERENCE CITATION** (Article name, Author(s) Name), [**COPYRIGHT**] (year of publication)

Note: For any republication from the British Journal of Cancer, the following credit line style applies:

Reprinted/adapted/translated by permission from [**the Licensor**]: on behalf of Cancer Research UK: : [**Journal Publisher** (e.g. Nature/Springer/Palgrave)] [**JOURNAL NAME**] [**REFERENCE CITATION** (Article name, Author(s) Name), [**COPYRIGHT]** (year of publication)

For **Advance Online Publication** papers:
Reprinted by permission from The [**the Licensor**]: on behalf of Cancer Research UK: [**Journal Publisher** (e.g. Nature/Springer/Palgrave)] [**JOURNAL NAME**] [**REFERENCE CITATION** (Article name, Author(s) Name), [**COPYRIGHT**] (year of publication), advance online publication, day month year (doi: 10.1038/sj.[JOURNAL ACRONYM])

For Book content:
Reprinted/adapted by permission from [**the Licensor**]: [**Book Publisher** (e.g. Palgrave Macmillan, Springer etc) [**Book Title**] by [**Book author**(s)] [**COPYRIGHT**] (year of publication)

Other Conditions:

Version 1.3

Questions? customercare@copyright.com or +1-855-239-3415 (toll free in the US) or +1-978-646-2777.

Figure A1: Permission to reproduce figures from Buzsáki and Mizuseki, 2014

SPRINGER NATURE LICENSE
TERMS AND CONDITIONS

Jul 14, 2021

This Agreement between Imperial College London -- Giuseppe Pietro Gava ("You") and Springer Nature ("Springer Nature") consists of your license details and the terms and conditions provided by Springer Nature and Copyright Clearance Center.

License Number	5107610469052
License date	Jul 14, 2021
Licensed Content Publisher	Springer Nature
Licensed Content Publication	Nature Neuroscience
Licensed Content Title	CA1 pyramidal cell diversity enabling parallel information processing in the hippocampus
Licensed Content Author	Ivan Soltesz et al
Licensed Content Date	Mar 28, 2018
Type of Use	Thesis/Dissertation
Requestor type	academic/university or research institute
Format	electronic
Portion	figures/tables/illustrations
Number of figures/tables/illustrations	1
High-res required	no

Will you be translating?	no
Circulation/distribution	1 - 29
Author of this Springer Nature content	no
Title	Network analysis of the cellular circuits of memory
Institution name	Imperial College London
Expected presentation date	Oct 2021
Portions	Figure 2
Requestor Location	Imperial College London Flat 4 224 Uxbridge road London, County W127JD United Kingdom Attn: Imperial College London
Total	0.00 USD

Terms and Conditions

Springer Nature Customer Service Centre GmbH
Terms and Conditions

This agreement sets out the terms and conditions of the licence (the **Licence**) between you and **Springer Nature Customer Service Centre GmbH** (the **Licensor**). By clicking 'accept' and completing the transaction for the material (**Licensed Material**), you also confirm your acceptance of these terms and conditions.

1. Grant of License

1. 1. The Licensor grants you a personal, non-exclusive, non-transferable, world-wide licence to reproduce the Licensed Material for the purpose specified in your order only. Licences are granted for the specific use requested in the order and for no other use, subject to the conditions below.

1. 2. The Licensor warrants that it has, to the best of its knowledge, the rights to license reuse of the Licensed Material. However, you should ensure that the material you are requesting is original to the Licensor and does not carry the copyright of another entity (as credited in the published version).

1. 3. If the credit line on any part of the material you have requested indicates that it was reprinted or adapted with permission from another source, then you should also seek permission from that source to reuse the material.

2. Scope of Licence

2. 1. You may only use the Licensed Content in the manner and to the extent permitted by these Ts&Cs and any applicable laws.

2. 2. A separate licence may be required for any additional use of the Licensed Material, e.g. where a licence has been purchased for print only use, separate permission must be obtained for electronic re-use. Similarly, a licence is only valid in the language selected and does not apply for editions in other languages unless additional translation rights have been granted separately in the licence. Any content owned by third parties are expressly excluded from the licence.

2. 3. Similarly, rights for additional components such as custom editions and derivatives require additional permission and may be subject to an additional fee. Please apply to Journalpermissions@springernature.com/bookpermissions@springernature.com for these rights.

2. 4. Where permission has been granted **free of charge** for material in print, permission may also be granted for any electronic version of that work, provided that the material is incidental to your work as a whole and that the electronic version is essentially equivalent to, or substitutes for, the print version.

2. 5. An alternative scope of licence may apply to signatories of the STM Permissions Guidelines, as amended from time to time.

3. Duration of Licence

3. 1. A licence for is valid from the date of purchase ('Licence Date') at the end of the relevant period in the below table:

Scope of Licence	Duration of Licence
Post on a website	12 months
Presentations	12 months
Books and journals	Lifetime of the edition in the language purchased

4. Acknowledgement

4. 1. The Licensor's permission must be acknowledged next to the Licenced Material in print. In electronic form, this acknowledgement must be visible at the same time as the figures/tables/illustrations or abstract, and must be hyperlinked to the journal/book's homepage. Our required acknowledgement format is in the Appendix below.

5. Restrictions on use

5. 1. Use of the Licensed Material may be permitted for incidental promotional use and minor editing privileges e.g. minor adaptations of single figures, changes of format, colour and/or style where the adaptation is credited as set out in Appendix 1 below. Any

other changes including but not limited to, cropping, adapting, omitting material that affect the meaning, intention or moral rights of the author are strictly prohibited.

5. 2. You must not use any Licensed Material as part of any design or trademark.

5. 3. Licensed Material may be used in Open Access Publications (OAP) before publication by Springer Nature, but any Licensed Material must be removed from OAP sites prior to final publication.

6. Ownership of Rights

6. 1. Licensed Material remains the property of either Licensor or the relevant third party and any rights not explicitly granted herein are expressly reserved.

7. Warranty

IN NO EVENT SHALL LICENSOR BE LIABLE TO YOU OR ANY OTHER PARTY OR ANY OTHER PERSON OR FOR ANY SPECIAL, CONSEQUENTIAL, INCIDENTAL OR INDIRECT DAMAGES, HOWEVER CAUSED, ARISING OUT OF OR IN CONNECTION WITH THE DOWNLOADING, VIEWING OR USE OF THE MATERIALS REGARDLESS OF THE FORM OF ACTION, WHETHER FOR BREACH OF CONTRACT, BREACH OF WARRANTY, TORT, NEGLIGENCE, INFRINGEMENT OR OTHERWISE (INCLUDING, WITHOUT LIMITATION, DAMAGES BASED ON LOSS OF PROFITS, DATA, FILES, USE, BUSINESS OPPORTUNITY OR CLAIMS OF THIRD PARTIES), AND
WHETHER OR NOT THE PARTY HAS BEEN ADVISED OF THE POSSIBILITY OF SUCH DAMAGES. THIS LIMITATION SHALL APPLY NOTWITHSTANDING ANY FAILURE OF ESSENTIAL PURPOSE OF ANY LIMITED REMEDY PROVIDED HEREIN.

8. Limitations

8. 1. ***BOOKS ONLY:***Where **'reuse in a dissertation/thesis'** has been selected the following terms apply: Print rights of the final author's accepted manuscript (for clarity, NOT the published version) for up to 100 copies, electronic rights for use only on a personal website or institutional repository as defined by the Sherpa guideline (www.sherpa.ac.uk/romeo/).

8. 2. For content reuse requests that qualify for permission under the STM Permissions Guidelines, which may be updated from time to time, the STM Permissions Guidelines supersede the terms and conditions contained in this licence.

9. Termination and Cancellation

9. 1. Licences will expire after the period shown in Clause 3 (above).

9. 2. Licensee reserves the right to terminate the Licence in the event that payment is not received in full or if there has been a breach of this agreement by you.

Appendix 1 — Acknowledgements:

For Journal Content:
Reprinted by permission from [**the Licensor**]: [**Journal Publisher** (e.g. Nature/Springer/Palgrave)] [**JOURNAL NAME**] [**REFERENCE CITATION** (Article name, Author(s) Name), [**COPYRIGHT**] (year of publication)

For **Advance Online Publication papers:**
Reprinted by permission from [**the Licensor**]: [**Journal Publisher** (e.g. Nature/Springer/Palgrave)] [**JOURNAL NAME**] [**REFERENCE CITATION** (Article name, Author(s) Name), [**COPYRIGHT**] (year of publication), advance online publication, day month year (doi: 10.1038/sj.[JOURNAL ACRONYM].)

For Adaptations/Translations:
Adapted/Translated by permission from [**the Licensor**]: [**Journal Publisher** (e.g. Nature/Springer/Palgrave)] [**JOURNAL NAME**] [**REFERENCE CITATION** (Article name, Author(s) Name), [**COPYRIGHT**] (year of publication)

Note: For any republication from the British Journal of Cancer, the following credit line style applies:

Reprinted/adapted/translated by permission from [**the Licensor**]: on behalf of Cancer Research UK: : [**Journal Publisher** (e.g. Nature/Springer/Palgrave)] [**JOURNAL NAME**] [**REFERENCE CITATION** (Article name, Author(s) Name), [**COPYRIGHT]** (year of publication)

For **Advance Online Publication** papers:
Reprinted by permission from The [**the Licensor**]: on behalf of Cancer Research UK: [**Journal Publisher** (e.g. Nature/Springer/Palgrave)] [**JOURNAL NAME**] [**REFERENCE CITATION** (Article name, Author(s) Name), [**COPYRIGHT**] (year of publication), advance online publication, day month year (doi: 10.1038/sj.[JOURNAL ACRONYM])

For Book content:
Reprinted/adapted by permission from [**the Licensor**]: [**Book Publisher** (e.g. Palgrave Macmillan, Springer etc) [**Book Title**] by [**Book author**(s)] [**COPYRIGHT**] (year of publication)

Other Conditions:

Version 1.3

Questions? customercare@copyright.com or +1-855-239-3415 (toll free in the US) or +1-978-646-2777.

Figure A2: Permission to reproduce figures from Soltesz and Losonczy, 2018

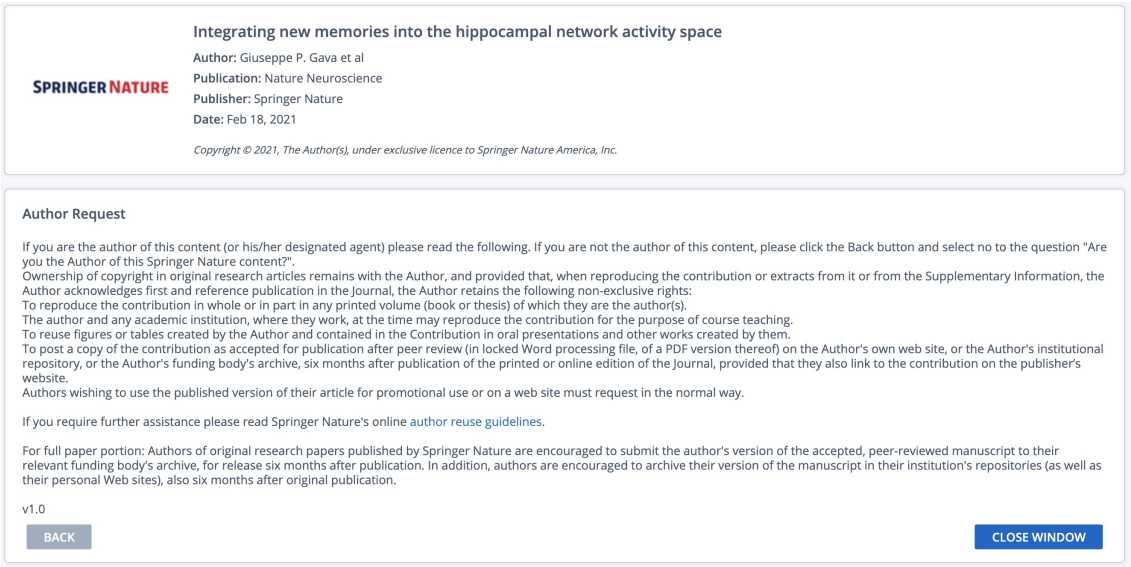

Integrating new memories into the hippocampal network activity space

Author: Giuseppe P. Gava et al
Publication: Nature Neuroscience
Publisher: Springer Nature
Date: Feb 18, 2021

Author Request

Figure A3: Permission to reproduce figures from Gava et al., 2021

Bibliography

Acimovic, J., Makki-Marttunen, T., and Linne, M.-L. (2015), 'The effects of neuron morphology on graph theoretic measures of network connectivity: the analysis of a two-level statistical model', *Frontiers in Neuroanatomy*, **9**, p. 76.

Allen, E. A., Damaraju, E., Plis, S. M., Erhardt, E. B., Eichele, T., and Calhoun, V. D. (2014), 'Tracking Whole-Brain Connectivity Dynamics in the Resting State', *Cerebral Cortex*, **24**(3), pp. 663–676.

Alme, C. B., Miao, C., Jezek, K., Treves, A., Moser, E. I., and Moser, M.-B. (2014), 'Place cells in the hippocampus: eleven maps for eleven rooms.' *Proceedings of the National Academy of Sciences of the United States of America*, **111**(52), pp. 18428–35.

Amico, E. and Goñi, J. (2018), 'The quest for identifiability in human functional connectomes', *Scientific Reports*, **8**(1), p. 8254.

Anderson, P. W. (1972), 'More Is Different', *Science*, **177**(4047), pp. 393–396.

Archer, E., Park, I. M., and Pillow, J. W. (2013), 'Bayesian entropy estimation for binary spike train data using parametric prior knowledge', *Adv. Neural. Inf. Process. Syst.*, **26**, pp. 1700–1708.

Arsigny, V., Fillard, P., Pennec, X., and Ayache, N. (2006), 'Log-Euclidean metrics for fast and simple calculus on diffusion tensors', *Magnetic Resonance in Medicine*, **56**(2), pp. 411–421.

Barack, D. L. and Krakauer, J. W. (2021), 'Two views on the cognitive brain', *Nature Reviews Neuroscience*, **22**(6), pp. 359–371.

Barlett, R. (1932), *Remembering: A Study in Experimental and Social Psychology*, Cambridge University Press.

Barlow, H. B. (1972), 'Single units and sensation: a neuron doctrine for perceptual psychology?', *Perception*, **1**(4), pp. 371–94.

Barnes, C. A., McNaughton, B. L., Mizumori, S. J., Leonard, B. W., and Lin, L.-H. (1990), 'Chapter 21 Chapter Comparison of spatial and temporal characteristics of neuronal activity in sequential stages of hippocampal processing', *Progress in Brain Research*, **83**, pp. 287–300.

Bassett, D. S. and Sporns, O. (2017), 'Network neuroscience', *Nature Neuroscience*, **20**(3), pp. 353–364.

Basso, M. A., Wurtz, R. H., and Huk, A. C. (1998), 'Modulation of neuronal activity in superior colliculus by changes in target probability.' *The Journal of neuroscience*, **18**(18), pp. 7519–34.

Belkin, M. and Niyogi, P. (2003), 'Laplacian Eigenmaps for Dimensionality Reduction and Data Representation', *Neural Computation*, **15**, pp. 1373–1396.

Bettencourt, L. M. A., Stephens, G. J., Ham, M. I., and Gross, G. W. (2007), 'Functional structure of cortical neuronal networks grown in vitro', *Physical Review E*, **75**(2), p. 021915.

Bialek, W., Ruyter van Stevenick, R. de, Rieke, F., and Warland, D. (1999), *Spikes : exploring the neural code*, MIT, p. 416.

Billeh, Y. N., Schaub, M. T., Anastassiou, C. A., Barahona, M., and Koch, C. (2014), 'Revealing cell assemblies at multiple levels of granularity', *Journal of Neuroscience Methods*, **236**, pp. 92–106.

Bliss, T. V. and Lomo, T. (1973), 'Long-lasting potentiation of synaptic transmission in the dentate area of the anaesthetized rabbit following stimulation of the perforant path.' *The Journal of physiology*, **232**(2), pp. 331–56.

Boccaletti, S., Latora, V., Moreno, Y., Chavez, M., and Hwang, D.-U. (2006), 'Complex networks: Structure and dynamics', *Physics Reports*, **424**, pp. 175–308.

Boyd, S. P. and Vandenberghe, L. (2004), *Convex optimization*, Cambridge University Press, p. 716.

Brecht, M., Schneider, M., Sakmann, B., and Margrie, T. W. (2004), 'Whisker movements evoked by stimulation of single pyramidal cells in rat motor cortex', *Nature*, **427**(6976), pp. 704–710.

Brun, V. H., Leutgeb, S., Wu, H.-Q., Schwarcz, R., Witter, M. P., Moser, E. I., and Moser, M.-B. (2008), 'Impaired spatial representation in CA1 after lesion of direct input from entorhinal cortex.' *Neuron*, **57**(2), pp. 290–302.

Bruno, A. M., Frost, W. N., and Humphries, M. D. (2017), 'A spiral attractor network drives rhythmic locomotion', *eLife*, **6**.

Bullmore, E. and Sporns, O. (2009), 'Complex brain networks: graph theoretical analysis of structural and functional systems', *Nature Reviews Neuroscience*, **10**(3), pp. 186–198.

Bunsey, M. and Eichenbaum, H. (1996), 'Conservation of hippocampal memory function in rats and humans.' *Nature*, **379**(6562), pp. 255–7.

Butts, D. (2003), 'How much information is associated with a particular stimulus?', *Network: Computation in Neural Systems*, **14**(2), pp. 177–187.

Buzsáki, G. (2019), *The brain from inside out*, Oxford University Press.

Buzsáki, G. (2004), 'Large-scale recording of neuronal ensembles', *Nature Neuroscience*, **7**(5), pp. 446–451.

– (2010), 'Neural syntax: cell assemblies, synapsembles, and readers.' *Neuron*, **68**(3), pp. 362–85.

– (2015), 'Hippocampal sharp wave-ripple: A cognitive biomarker for episodic memory and planning', *Hippocampus*, **25**(10), pp. 1073–1188.

Buzsáki, G. (2009), *Rhythms of the Brain*, Oxford University Press.

Buzsáki, G., Adey, W., et al. (2002), 'Theta oscillations in the hippocampus.' *Neuron*, **33**(3), pp. 325–40.

Buzsáki, G., Geisler, C., Henze, D. A., and Wang, X.-J. (2004), 'Interneuron Diversity series: Circuit complexity and axon wiring economy of cortical interneurons', *Trends in Neurosciences*, **27**(4), pp. 186–193.

Buzsáki, G. and Llinás, R. (2017), 'Space and time in the brain.' *Science (New York, N.Y.)*, **358**(6362), pp. 482–485.

Buzsáki, G. and Mizuseki, K. (2014), 'The log-dynamic brain: how skewed distributions affect network operations.' *Nature reviews. Neuroscience*, **15**(4), pp. 264–78.

Cavalieri, D., Angelova, A., Islah, A., Lopez, C., Baude, A., and Cossart, R. (2021), 'CA1 pyramidal cell diversity is rooted in the time of neurogenesis', *bioRxiv*, p. 2021.03.07.433031.

Cembrowski, M. S. and Spruston, N. (2019), 'Heterogeneity within classical cell types is the rule: lessons from hippocampal pyramidal neurons', *Nature Reviews Neuroscience*, **20**(4), pp. 193–204.

Chari, T., Banerjee, J., and Pachter, L. (2021), 'The Specious Art of Single-Cell Genomics', *bioRxiv*.

Chaudhuri, R., Gerçek, B., Pandey, B., Peyrache, A., and Fiete, I. (2019), 'The intrinsic attractor manifold and population dynamics of a canonical cognitive circuit across waking and sleep', *Nature Neuroscience*, **22**(9), pp. 1512–1520.

Churchland, M. M., Cunningham, J. P., Kaufman, M. T., Foster, J. D., Nuyujukian, P., Ryu, S. I., and Shenoy, K. V. (2012), 'Neural population dynamics during reaching', *Nature*, **487**(7405), pp. 51–56.

Churchland, P. S. and Sejnowski, T. J. (1992), *The computational brain*, MIT Press, p. 544.

Colgin, L. L., Moser, E. I., and Moser, M.-B. (2008), 'Understanding memory through hippocampal remapping.' *Trends in neurosciences*, **31**(9), pp. 469–77.

Colon-Perez, L. M., Couret, M., Triplett, W., Price, C. C., and Mareci, T. H. (2016), 'Small Worldness in Dense and Weighted Connectomes', *Frontiers in Physics*, **4**, p. 14.

Costantini, G. and Perugini, M. (2014), 'Generalization of Clustering Coefficients to Signed Correlation Networks', *PLoS ONE*, **9**(2), ed. by A. de la Fuente, e88669.

Cover, T. M. and Thomas, J. A. (2006), *Elements of Information Theory*, 2nd, John Wiley & Sons, Inc., Hoboken, New Jersey.

Csicsvari, J., Hirase, H., Czurkó, A., Mamiya, A., and Buzsáki, G. (1999), 'Fast network oscillations in the hippocampal CA1 region of the behaving rat.' *The Journal of neuroscience : the official journal of the Society for Neuroscience*, **19**(16), RC20.

Csicsvari, J., Hirase, H., Czurko, A., and Buzsáki, G. (1998), 'Reliability and State Dependence of Pyramidal Cell–Interneuron Synapses in the Hippocampus', *Neuron*, **21**(1), pp. 179–189.

Csicsvari, J., Hirase, H., Czurkó, A. S., Mamiya, A., and Buzsáki, G. (1999), 'Oscillatory Coupling of Hippocampal Pyramidal Cells and Interneurons in the Behaving Rat', *The Journal of Neuroscience*.

Cunningham, J. P. and Yu, B. M. (2014), 'Dimensionality reduction for large-scale neural recordings', *Nature Neuroscience*, **17**(11), pp. 1500–1509.

Danielson, N. B., Zaremba, J. D., Kaifosh, P., Bowler, J., Ladow, M., and Losonczy, A. (2016), 'Sublayer-Specific Coding Dynamics during Spatial Navigation and Learning in Hippocampal Area CA1.' *Neuron*, **91**(3), pp. 652–65.

Das, A. and Fiete, I. R. (2020), 'Systematic errors in connectivity inferred from activity in strongly recurrent networks', *Nature Neuroscience*, **23**(10), pp. 1286–1296.

Dayan, P., Hinton, G. E., Neal, R. M., and Zemel, R. S. (1995), 'The Helmholtz machine.' *Neural computation*, **7**(5), pp. 889–904.

Deco, G. and Rolls, E. T. (2006), 'Decision-making and Weber's law: a neurophysiological model', *European Journal of Neuroscience*, **24**(3), pp. 901–916.

DeFelipe, J. (2006), 'Brain plasticity and mental processes: Cajal again', *Nature Reviews Neuroscience*, **7**(10), pp. 811–817.

Denny, C. A., Kheirbek, M. A., Alba, E. L., Tanaka, K. F., Brachman, R. A., Laughman, K. B., Tomm, N. K., Turi, G. F., Losonczy, A., and Hen, R. (2014), 'Hippocampal Memory Traces Are Differentially Modulated by Experience, Time, and Adult Neurogenesis', *Neuron*, **83**(1), pp. 189–201.

Desimone, R., Albright, T. D., Gross, C. G., and Bruce, C. (1984), 'Stimulus-selective properties of inferior temporal neurons in the macaque.' *The Journal of neuroscience : the official journal of the Society for Neuroscience*, **4**(8), pp. 2051–62.

Diesmann, M., Gewaltig, M.-O., and Aertsen, A. (1999), 'Stable propagation of synchronous spiking in cortical neural networks', *Nature*, **402**(6761), pp. 529–533.

Djikstra, E. W. (1959), 'A Note on Two Problems in Connexion with Graphs', *Numerische Mathematlk*, **1**, pp. 269–271.

Dombeck, D. A., Harvey, C. D., Tian, L., Looger, L. L., and Tank, D. W. (2010), 'Functional imaging of hippocampal place cells at cellular resolution during virtual navigation', *Nature Neuroscience*, **13**(11), pp. 1433–1440.

Douglas, R. M. and Goddard, G. V. (1975), 'Long-term potentiation of the perforant path-granule cell synapse in the rat hippocampus.' *Brain research*, **86**(2), pp. 205–15.

Dragoi, G., Harris, K. D., and Buzsáki, G. (2003), 'Place representation within hippocampal networks is modified by long-term potentiation.' *Neuron*, **39**(5), pp. 843–53.

Driscoll, L. N., Pettit, N. L., Minderer, M., Chettih, S. N., and Harvey, C. D. (2017), 'Dynamic Reorganization of Neuronal Activity Patterns in Parietal Cortex', *Cell*, **170**(5), pp. 986–999.

Dudai, Y. (2004), 'The neurobiology of consolidations, or, how stable is the engram?', *Annual review of psychology*, **55**, pp. 51–86.

– (2012), 'The Restless Engram: Consolidations Never End', *Annual Review of Neuroscience*, **35**(1), pp. 227–247.

Dudai, Y. and Morris, R. G. M. (2013), 'Memorable trends.' *Neuron*, **80**(3), pp. 742–50.

Dupret, D., O'Neill, J., Pleydell-Bouverie, B., and Csicsvari, J. (2010), 'The reorganization and reactivation of hippocampal maps predict spatial memory performance', *Nature Neuroscience*, **13**(8), pp. 995–1002.

Eichenbaum, H., Dudchenko, P., Wood, E., Shapiro, M., and Tanila, H. (1999), 'The hippocampus, memory, and place cells: is it spatial memory or a memory space?', *Neuron*, **23**(2), pp. 209–26.

English, D. F., Mckenzie, S., Evans, T., Kim, K., Yoon, E., and Buzsáki, G. (2017), 'Pyramidal Cell-Interneuron Circuit Architecture and Dynamics in Hippocampal Networks', *Neuron*, **96**, pp. 505–520.

Ercsey-Ravasz, M., Markov, N. T., Lamy, C., Van Essen, D. C., Knoblauch, K., Toroczkai, Z., and Kennedy, H. (2013), 'A predictive network model of cerebral cortical connectivity based on a distance rule.' *Neuron*, **80**(1), pp. 184–97.

Fairhall, A. (2014), 'The receptive field is dead. Long live the receptive field?', *Current Opinion in Neurobiology*, **25**, pp. ix–xii.

Fanselow, M. S. and Dong, H.-W. (2010), 'Are the dorsal and ventral hippocampus functionally distinct structures?', *Neuron*, **65**(1), pp. 7–19.

Fernández-Ruiz, A., Oliva, A., Nagy, G. A., Maurer, A. P., Berényi, A., and Buzsáki, G. (2017), 'Entorhinal-CA3 Dual-Input Control of Spike Timing in the Hippocampus by Theta-Gamma Coupling.' *Neuron*, **93**(5), pp. 1213–1226.

Feulner, B. and Clopath, C. (2021), 'Neural manifold under plasticity in a goal driven learning behaviour', *PLOS Computational Biology*, **17**(2), ed. by A. Morrison, e1008621.

Finn, E. S., Shen, X., Scheinost, D., Rosenberg, M. D., Huang, J., Chun, M. M., Papademetris, X., and Constable, R. T. (2015), 'Functional connectome finger-

printing: identifying individuals using patterns of brain connectivity', *Nature Neuroscience*, **18**(11), pp. 1664–1671.

Floyd, R. W. (1962), 'Algorithm 97: shortest path. 5, 345 (1962).' *Communications of the ACM*, **5**, pp. 345–345.

Frank, L. M., Brown, E. N., and Wilson, M. (2000), 'Trajectory Encoding in the Hippocampus and Entorhinal Cortex', *Neuron*, **27**(1), pp. 169–178.

Freeman, W. J., Rogers, L. J., Holmes, M. D., and Silbergeld, D. L. (2000), 'Spatial spectral analysis of human electrocorticograms including the alpha and gamma bands.' *Journal of neuroscience methods*, **95**(2), pp. 111–21.

Friston, K. and Buzsáki, G. (2016), 'The Functional Anatomy of Time: What and When in the Brain.' *Trends in cognitive sciences*, **20**(7), pp. 500–511.

Friston, K., Stephan, K., Li, B., and Daunizeau, J. (2010), 'Generalised Filtering', *Mathematical Problems in Engineering*, **2010**, pp. 1–34.

Fujii, T., Moscovitch, M., and Nadel, L. (2000), *Handbook of Neuropsychology*, ed. by Elsevier.

Fusi, S., Miller, E. K., and Rigotti, M. (2016), 'Why neurons mix: high dimensionality for higher cognition', *Current Opinion in Neurobiology*, **37**, pp. 66–74.

Gallego, J. A., Perich, M. G., Chowdhury, R. H., Solla, S. A., and Miller, L. E. (2020), 'Long-term stability of cortical population dynamics underlying consistent behavior', *Nature Neuroscience*, **23**(2), pp. 260–270.

Gauthier, J. L. and Tank, D. W. (2018), 'A Dedicated Population for Reward Coding in the Hippocampus', *Neuron*, **99**(1), pp. 179–193.

Gava, G. P., McHugh, S. B., Lefèvre, L., Lopes-dos-Santos, V., Trouche, S., El-Gaby, M., Schultz, S. R., and Dupret, D. (2021), 'Integrating new memories into the hippocampal network activity space', *Nature Neuroscience*, **24**(3), pp. 326–330.

Gibbon, J., Church, R. M., and Meck, W. H. (1984), 'Scalar timing in memory.' *Annals of the New York Academy of Sciences*, **423**, pp. 52–77.

Gibbon, J. (1977), 'Scalar expectancy theory and Weber's law in animal timing.' *Psychological Review*, **84**(3), pp. 279–325.

Gilboa, A., Winocur, G., Grady, C. L., Hevenor, S. J., and Moscovitch, M. (2004), 'Remembering our past: functional neuroanatomy of recollection of recent and very remote personal events.' *Cerebral cortex*, **14**(11), pp. 1214–25.

Giovannucci, A., Friedrich, J., Gunn, P., Kalfon, J., Brown, B. L., Koay, S. A., Taxidis, J., Najafi, F., Gauthier, J. L., Zhou, P., Khakh, B. S., Tank, D. W., Chklovskii, D. B., and Pnevmatikakis, E. A. (2019), 'CaImAn an open source tool for scalable calcium imaging data analysis', *eLife*, **8**.

Girardeau, G., Benchenane, K., Wiener, S. I., Buzsáki, G., and Zugaro, M. B. (2009), 'Selective suppression of hippocampal ripples impairs spatial memory.' *Nature neuroscience*, **12**(10), pp. 1222–3.

Glickman, S. E. (1961), 'Perseverative neural processes and consolidation of the memory trace.' *Psychological bulletin*, **58**, pp. 218–33.

Go, M. A., Rogers, J., Gava, G. P., Davey, C. E., Prado, S., Liu, Y., and Schultz, S. R. (2021), 'Place Cells in Head-Fixed Mice Navigating a Floating Real-World Environment', *Frontiers in Cellular Neuroscience*, **15**, p. 19.

Gold, J. I. and Shadlen, M. N. (2000), 'Representation of a perceptual decision in developing oculomotor commands', *Nature*, **404**(6776), pp. 390–394.

Golgi, C. (1885), *Sulla fina anatomia degli organi centrali del sistema nervoso*, Reggio Emilia: Tip. S. Calderini e Figlio.

Gonzalez, W. G., Zhang, H., Harutyunyan, A., and Lois, C. (2019), 'Persistence of neuronal representations through time and damage in the hippocampus.' *Science (New York, N.Y.)*, **365**(6455), pp. 821–825.

Grassberger, P. and Procaccia, I. (1983), 'Measuring the strangeness of strange attractors', *Physica D: Nonlinear Phenomena*, **9**(1-2), pp. 189–208.

Grewe, B. F., Gründemann, J., Kitch, L. J., Lecoq, J. A., Parker, J. G., Marshall, J. D., Larkin, M. C., Jercog, P. E., Grenier, F., Li, J. Z., Lüthi, A., and Schnitzer,

M. J. (2017), 'Neural ensemble dynamics underlying a long-term associative memory', *Nature*, **543**(7647), pp. 670–675.

Grosmark, A. D. and Buzsáki, G. (2016), 'Diversity in neural firing dynamics supports both rigid and learned hippocampal sequences', *Science*, **351**(6280).

Hagberg, A. A., Schult, D. A., and Swart, P. J. (2008), 'Exploring Network Structure, Dynamics, and Function using NetworkX', *Proceedings of the 7th Python in Science Conference (SciPy 2008)*, pp. 11–15.

Harris, K. D., Henze, D. A., Csicsvari, J., Hirase, H., and Buzsáki, G. (2000), 'Accuracy of tetrode spike separation as determined by simultaneous intracellular and extracellular measurements.' *Journal of neurophysiology*, **84**(1), pp. 401–14.

Harris, K. D., Hirase, H., Leinekugel, X., Henze, D. A., and Buzsáki, G. (2001), 'Temporal Interaction between Single Spikes and Complex Spike Bursts in Hippocampal Pyramidal Cells', *Neuron*, **32**(1), pp. 141–149.

Harris, K. D., Csicsvari, J., Hirase, H., Dragoi, G., and Buzsáki, G. (2003), 'Organization of cell assemblies in the hippocampus', *Nature*, **424**(6948), pp. 552–556.

Harvey, C. D., Coen, P., and Tank, D. W. (2012), 'Choice-specific sequences in parietal cortex during a virtual-navigation decision task', *Nature*, **484**(7392), pp. 62–68.

Hasselmo, M. E., Schnell, E., and Barkai, E. (1995), 'Dynamics of learning and recall at excitatory recurrent synapses and cholinergic modulation in rat hippocampal region CA3.' *The Journal of neuroscience*, **15**(7 Pt 2), pp. 5249–62.

Hawkins, D. M. (2004), 'The Problem of Overfitting', *Journal of Chemical Information and Computer Sciences*, **44**(1), pp. 1–12.

Hebb, D. O. (1949), *The Organization of Behavior: A Neuropsychological Theory*, New York: Wiley.

Ho, J., Tumkaya, T., Aryal, S., Choi, H., and Claridge-Chang, A. (2019), 'Moving beyond P values: data analysis with estimation graphics', *Nature Methods*, **16**(7), pp. 565–566.

Hochberg, L. R., Serruya, M. D., Friehs, G. M., Mukand, J. A., Saleh, M., Caplan, A. H., Branner, A., Chen, D., Penn, R. D., and Donoghue, J. P. (2006), 'Neuronal ensemble control of prosthetic devices by a human with tetraplegia.' *Nature*, **442**(7099), pp. 164–71.

Houweling, A. R. and Brecht, M. (2008), 'Behavioural report of single neuron stimulation in somatosensory cortex', *Nature*, **451**(7174), pp. 65–68.

Hubel, D. H. and Wiesel, T. N. (1962), 'Receptive fields, binocular interaction and functional architecture in the cat's visual cortex.' *The Journal of physiology*, **160**(1), pp. 106–54.

Hubel, D. H. (1957), 'Tungsten Microelectrode for Recording from Single Units', *Science*, **125**(3247).

Humphries, M. D. (2011), 'Spike-train communities: finding groups of similar spike trains.' *Journal of neuroscience*, **31**(6), pp. 2321–36.

– (2018), 'Dynamical networks: Finding, measuring, and tracking neural population activity using network science.' *Network neuroscience*, **1**(4), pp. 324–338.

Humphries, M. D. and Gurney, K. (2008), 'Network 'Small-World-Ness': A Quantitative Method for Determining Canonical Network Equivalence', *PLoS ONE*, **3**(4), ed. by O. Sporns, e0002051.

Ikegaya, Y., Sasaki, T., Ishikawa, D., Honma, N., Tao, K., Takahashi, N., Minamisawa, G., Ujita, S., and Matsuki, N. (2013), 'Interpyramid Spike Transmission Stabilizes the Sparseness of Recurrent Network Activity', *Cerebral Cortex*, **23**(2), pp. 293–304.

Ince, R. A. A., Petersen, R. S., Swan, D. C., and Panzeri, S. (2009), 'Python for information theoretic analysis of neural data', *Frontiers in Neuroinformatics*, **3**, p. 4.

James, W. (1890), *The principles of psychology*, Henry Holt and Company.

Johnson, W. B. and Lindenstrauss, J. (1984), 'Extensions of Lipschitz mappings into a Hilbert space', in: pp. 189–206.

Kadir, S. N., Goodman, D. F. M., and Harris, K. D. (2014), 'High-dimensional cluster analysis with the masked EM algorithm.' *Neural computation*, **26**(11), pp. 2379–94.

Kay, K. and Frank, L. M. (2018), 'Three brain states in the hippocampus and cortex'.

Kebschull, J. M., Garcia da Silva, P., Reid, A. P., Peikon, I. D., Albeanu, D. F., and Zador, A. M. (2016), 'High-Throughput Mapping of Single-Neuron Projections by Sequencing of Barcoded RNA.' *Neuron*, **91**(5), pp. 975–987.

Kenet, T., Bibitchkov, D., Tsodyks, M., Grinvald, A., and Arieli, A. (2003), 'Spontaneously emerging cortical representations of visual attributes', *Nature*, **425**(6961), pp. 954–956.

Kentros, C., Hargreaves, E., Hawkins, R. D., Kandel, E. R., Shapiro, M., and Muller, R. V. (1998), 'Abolition of long-term stability of new hippocampal place cell maps by NMDA receptor blockade.' *Science*, **280**(5372), pp. 2121–6.

Kentros, C. G., Agnihotri, N. T., Streater, S., Hawkins, R. D., and Kandel, E. R. (2004), 'Increased attention to spatial context increases both place field stability and spatial memory.' *Neuron*, **42**(2), pp. 283–95.

Khambhati, A. N., Davis, K. A., Oommen, B. S., Chen, S. H., Lucas, T. H., Litt, B., and Bassett, D. S. (2015), 'Dynamic Network Drivers of Seizure Generation, Propagation and Termination in Human Neocortical Epilepsy', *PLOS Computational Biology*, **11**(12), ed. by M. Kramer, e1004608.

Kinsky, N. R., Sullivan, D. W., Mau, W., Hasselmo, M. E., and Eichenbaum, H. B. (2018), 'Hippocampal Place Fields Maintain a Coherent and Flexible Map across Long Timescales.' *Current biology : CB*, **28**(22), pp. 3578–3588.

Kinsky, N. R., Mau, W., Sullivan, D. W., Levy, S. J., Ruesch, E. A., and Hasselmo, M. E. (2020), 'Trajectory-modulated hippocampal neurons persist throughout memory-guided navigation', *Nature Communications*, **11**(1), p. 2443.

Ko, H., Hofer, S. B., Pichler, B., Buchanan, K. A., Sjöström, P. J., and Mrsic-Flogel, T. D. (2011), 'Functional specificity of local synaptic connections in neocortical networks', *Nature*, **473**(7345), pp. 87–91.

Kreiman, G., Koch, C., and Fried, I. (2000), 'Category-specific visual responses of single neurons in the human medial temporal lobe', *Nature Neuroscience*, **3**(9), pp. 946–953.

Kruskal, J. B. and Wish, M. (1978), *Multidimensional scaling*, Sage Publications, p. 93.

Kruskal, P. B., Stanis, J. J., McNaughton, B. L., and Thomas, P. J. (2007), 'A binless correlation measure reduces the variability of memory reactivation estimates', *Statistics in Medicine*, **26**(21), pp. 3997–4008.

Kubie, J. L., Levy, E. R. J., and Fenton, A. A. (2019), 'Is hippocampal remapping the physiological basis for context?', *Hippocampus*, hipo.23160.

– (2020), 'Is hippocampal remapping the physiological basis for context?', *Hippocampus*, **30**(8), pp. 851–864.

Kumaran, D., Hassabis, D., and McClelland, J. L. (2016), 'What Learning Systems do Intelligent Agents Need? Complementary Learning Systems Theory Updated.' *Trends in cognitive sciences*, **20**(7), pp. 512–534.

Lee, W.-C. A., Bonin, V., Reed, M., Graham, B. J., Hood, G., Glattfelder, K., and Reid, R. C. (2016), 'Anatomy and function of an excitatory network in the visual cortex', *Nature*, **532**(7599), pp. 370–374.

Lemon, W. C., Pulver, S. R., Höckendorf, B., McDole, K., Branson, K., Freeman, J., and Keller, P. J. (2015), 'Whole-central nervous system functional imaging in larval Drosophila', *Nature Communications*, **6**(1), p. 7924.

Leutgeb, J. K., Leutgeb, S., Moser, M.-B., and Moser, E. I. (2007), 'Pattern separation in the dentate gyrus and CA3 of the hippocampus.' *Science*, **315**(5814), pp. 961–6.

Leutgeb, S., Leutgeb, J. K., Treves, A., Moser, M.-B., and Moser, E. I. (2004), 'Distinct ensemble codes in hippocampal areas CA3 and CA1.' *Science (New York, N.Y.)*, **305**(5688), pp. 1295–8.

Levenstein, D., Watson, B. O., Rinzel, J., and Buzsáki, G. (2017), 'Sleep regulation of the distribution of cortical firing rates', *Current Opinion in Neurobiology*, **44**, pp. 34–42.

Liu, X., Ramirez, S., Pang, P. T., Puryear, C. B., Govindarajan, A., Deisseroth, K., and Tonegawa, S. (2012), 'Optogenetic stimulation of a hippocampal engram activates fear memory recall', *Nature*, **484**(7394), pp. 381–385.

Loewenstein, Y., Kuras, A., and Rumpel, S. (2011), 'Multiplicative dynamics underlie the emergence of the log-normal distribution of spine sizes in the neocortex in vivo.' *The Journal of Neuroscience*, **31**(26), pp. 9481–8.

Lopes-dos-Santos, V., Ven, G. M. van de, Morley, A., Trouche, S., Campo-Urriza, N., and Dupret, D. (2018), 'Parsing Hippocampal Theta Oscillations by Nested Spectral Components during Spatial Exploration and Memory-Guided Behavior', *Neuron*, **100**(4), pp. 940–952.

Lorente De Nó, R. (1934), 'Studies on the structure of the cerebral cortex. II. Continuation of the study of the ammonic system.' *Journal für Psychologie und Neurologie*, (46), pp. 113–117.

Lorente de Nò, R. (1933), 'Studies on the structure of the cerebral cortex,. I: the area entorhinalis', *J Psychol Neurol*, **45**, pp. 381–438.

Low, R. J., Lewallen, S., Aronov, D., Nevers, R., and Tank, D. W. (2018), 'Probing variability in a cognitive map using manifold inference from neural dynamics', *bioRxiv*, p. 418939.

Lu, J., Yu, X., Chen, G., and Cheng, D. (2004), 'Characterizing the Synchronizability of Small-World Dynamical Networks', *IEEE Transactions on Circuits and Systems I*, **51**(4), pp. 787–796.

Luria, A. R. (1968), *The Mind of a Mnemonist: A Little Book about a Vast Memory*, Cape.

Lyttle, D. and Fellous, J.-M. (2011), 'A new similarity measure for spike trains: sensitivity to bursts and periods of inhibition.' *Journal of neuroscience methods*, **199**(2), pp. 296–309.

Mackay, D. J. C. (2003), *Information Theory, Inference, and Learning Algorithms*, Cambridge University Press.

Magland, J., Jun, J. J., Lovero, E., Morley, A. J., Hurwitz, C. L., Buccino, A. P., Garcia, S., and Barnett, A. H. (2020), 'SpikeForest, reproducible web-facing ground-truth validation of automated neural spike sorters', *eLife*, **9**.

Mante, V., Sussillo, D., Shenoy, K. V., and Newsome, W. T. (2013), 'Context-dependent computation by recurrent dynamics in prefrontal cortex', *Nature*, **503**(7474), pp. 78–84.

Markov, N. T., Misery, P., Falchier, A., Lamy, C., Vezoli, J., Quilodran, R., Gariel, M. A., Giroud, P., Ercsey-Ravasz, M., Pilaz, L. J., Huissoud, C., Barone, P., Dehay, C., Toroczkai, Z., Van Essen, D. C., Kennedy, H., and Knoblauch, K. (2011), 'Weight consistency specifies regularities of macaque cortical networks.' *Cerebral cortex (New York, N.Y. : 1991)*, **21**(6), pp. 1254–72.

Marr, D. (1970), 'A theory for cerebral neocortex', *Proceedings of the Royal Society of London.*, **176**(1043), pp. 161–234.

– (1971), 'Simple memory: a theory for archicortex', *Philosophical Transactions of the Royal Society of London. B, Biological Sciences*, **262**(841), pp. 23–81.

Mau, W., Hasselmo, M. E., and Cai, D. J. (2020), 'The brain in motion: How ensemble fluidity drives memory-updating and flexibility', *eLife*, **9**.

Mau, W., Sullivan, D. W., Kinsky, N. R., Hasselmo, M. E., and Howard, M. W. (2018), 'The Same Hippocampal CA1 Population Simultaneously Codes Temporal Information over Multiple Timescales', *Current Biology*, **28**.

Mayer, C., Bandler, R. C., and Fishell, G. (2016), 'Lineage Is a Poor Predictor of Interneuron Positioning within the Forebrain.' *Neuron*, **92**(1), pp. 45–51.

McClelland, J. L., McNaughton, B. L., and O'Reilly, R. C. (1995), 'Why there are complementary learning systems in the hippocampus and neocortex: Insights from the successes and failures of connectionist models of learning and memory.' *Psychological Review*, **102**(3), pp. 419–457.

Mcinnes, L., Healy, J., Saul, N., and Großberger, L. (2018), 'UMAP: Uniform Manifold Approximation and Projection Software • Review • Repository • Archive', *The Journal of Open Source Software*, **3**(29), p. 861.

McKenzie, S. and Eichenbaum, H. (2011), 'Consolidation and reconsolidation: two lives of memories?', *Neuron*, **71**(2), pp. 224–33.

McKenzie, S., Frank, A. J., Kinsky, N. R., Porter, B., Rivière, P. D., and Eichenbaum, H. (2014), 'Hippocampal Representation of Related and Opposing Memories Develop within Distinct, Hierarchically Organized Neural Schemas', *Neuron*, **83**(1), pp. 202–215.

McKenzie, S., Robinson, N. T. M., Herrera, L., Churchill, J. C., and Eichenbaum, H. (2013), 'Learning causes reorganization of neuronal firing patterns to represent related experiences within a hippocampal schema.' *The Journal of neuroscience : the official journal of the Society for Neuroscience*, **33**(25), pp. 10243–56.

McNamara, C. G., Tejero-Cantero, Á., Trouche, S., Campo-Urriza, N., and Dupret, D. (2014), 'Dopaminergic neurons promote hippocampal reactivation and spatial memory persistence', *Nature Neuroscience*, **17**(12), pp. 1658–1660.

Migues, P. V., Liu, L., Archbold, G. E. B., Einarsson, E. Ö., Wong, J., Bonasia, K., Ko, S. H., Wang, Y. T., and Hardt, O. (2016), 'Blocking Synaptic Removal

of GluA2-Containing AMPA Receptors Prevents the Natural Forgetting of Long-Term Memories.' *The Journal of neuroscience*, **36**(12), pp. 3481–94.

Milner, B., Squire, L. R., and Kandel, E. R. (1998), 'Cognitive neuroscience and the study of memory.' *Neuron*, **20**(3), pp. 445–68.

Milstein, A. D., Bloss, E. B., Apostolides, P. F., Vaidya, S. P., Dilly, G. A., Zemelman, B. V., and Magee, J. C. (2015), 'Inhibitory Gating of Input Comparison in the CA1 Microcircuit.' *Neuron*, **87**(6), pp. 1274–1289.

Mizuseki, K. and Buzsáki, G. (2013), 'Preconfigured, skewed distribution of firing rates in the hippocampus and entorhinal cortex.' *Cell reports*, **4**(5), pp. 1010–21.

Mizuseki, K., Diba, K., Pastalkova, E., and Buzsáki, G. (2011), 'Hippocampal CA1 pyramidal cells form functionally distinct sublayers', *Nature Neuroscience*, **14**(9), pp. 1174–1181.

Moakher, M. (2005), 'A Differential Geometric Approach to the Geometric Mean of Symmetric Positive-Definite Matrices', *SIAM Journal on Matrix Analysis and Applications*, **26**(3), pp. 735–747.

Morris, R. G. M. (2006), 'Elements of a neurobiological theory of hippocampal function: the role of synaptic plasticity, synaptic tagging and schemas.' *The European journal of neuroscience*, **23**(11), pp. 2829–46.

Moscovitch, M., Nadel, L., Winocur, G., Gilboa, A., and Rosenbaum, R. S. (2006), 'The cognitive neuroscience of remote episodic, semantic and spatial memory.' *Current opinion in neurobiology*, **16**(2), pp. 179–90.

Moser, E. I., Moser, M.-B., and McNaughton, B. L. (2017), 'Spatial representation in the hippocampal formation: a history', *Nature Neuroscience*, **20**(11), pp. 1448–1464.

Moser, E. I., Kropff, E., and Moser, M.-B. (2008), 'Place Cells, Grid Cells, and the Brain's Spatial Representation System', *Annual Review of Neuroscience*, **31**(1), pp. 69–89.

Muldoon, S. F., Bridgeford, E. W., and Bassett, D. S. (2016), 'Small-World Propensity and Weighted Brain Networks', *Scientific Reports*, **6**(1), p. 22057.

Muller, R. U., Kubie, J. L., and Ranck, J. B. (1987), 'Spatial firing patterns of hippocampal complex-spike cells in a fixed environment.' *Journal of neuroscience*, **7**(7), pp. 1935–50.

Nadel, L., Hupbach, A., Gomez, R., and Newman-Smith, K. (2012), 'Memory formation, consolidation and transformation.' *Neuroscience and biobehavioral reviews*, **36**(7), pp. 1640–5.

Nader, K., Schafe, G. E., and Le Doux, J. E. (2000), 'Fear memories require protein synthesis in the amygdala for reconsolidation after retrieval', *Nature*, **406**(6797), pp. 722–726.

Nadim, F. and Bucher, D. (2014), 'Neuromodulation of neurons and synapses.' *Current opinion in neurobiology*, **29**, pp. 48–56.

Navarro-Sune, X., Hudson, A. L., Fallani, F. D. V., Martinerie, J., Witon, A., Pouget, P., Raux, M., Similowski, T., and Chavez, M. (2017), 'Riemannian Geometry Applied to Detection of Respiratory States From EEG Signals: The Basis for a Brain–Ventilator Interface', *IEEE Transactions on Biomedical Engineering*, **64**(5), pp. 1138–1148.

Navas-Olive, A., Valero, M., Jurado-Parras, T., Salas-Quiroga, A. de, Averkin, R. G., Gambino, G., Cid, E., and Prida, L. M. de la (2020), 'Multimodal determinants of phase-locked dynamics across deep-superficial hippocampal sublayers during theta oscillations', *Nature Communications*, **11**(1), p. 2217.

Nemenman, I., Shafee, F., and Bialek, W. (2001), 'Entropy and Inference, Revisited', *Adv. Neural. Inf. Process.*, (14), pp. 95–100.

Newman, M. E. J. (2003), *The Structure and Function of Complex Networks **, tech. rep. 2, pp. 167–256.

Nieh, E. H., Schottdorf, M., Freeman, N. W., Low, R. J., Lewallen, S., Koay, S. A., Pinto, L., Gauthier, J. L., Brody, C. D., and Tank, D. W. (2021), 'Geometry of abstract learned knowledge in the hippocampus.' *Nature*, **595**(7865), pp. 80–84.

Nishikawa, T., Motter, A. E., Lai, Y.-C., and Hoppensteadt, F. C. (2003), 'Heterogeneity in Oscillator Networks: Are Smaller Worlds Easier to Synchronize?', *Physical Review Letters*, **91**(1), p. 014101.

O'Keefe, J. and Dostrovsky, J. (1971), 'The hippocampus as a spatial map. Preliminary evidence from unit activity in the freely-moving rat'.

O'Keefe, J. and Nadel, L. (1978), *The Hippocampus as a Cognitive Map*, Oxford University Press.

O'Keefe, J. and Recce, M. L. (1993), 'Phase relationship between hippocampal place units and the EEG theta rhythm', *Hippocampus*, **3**(3), pp. 317–330.

O'Neill, J., Senior, T. J., Allen, K., Huxter, J. R., and Csicsvari, J. (2008), 'Reactivation of experience-dependent cell assembly patterns in the hippocampus', *Nature Neuroscience*, **11**(2), pp. 209–215.

Okun, M., Steinmetz, N. A., Cossell, L., Florencia Iacaruso, M., Ko, H., Barthó, P., Moore, T., Hofer, S. B., Mrsic-Flogel, T. D., Carandini, M., and Harris, K. D. (2015), 'Diverse coupling of neurons to populations in sensory cortex', *Nature*.

Oliva, A., Fernández-Ruiz, A., Buzsáki, G., and Berényi, A. (2016), 'Spatial coding and physiological properties of hippocampal neurons in the Cornu Ammonis subregions.' *Hippocampus*, **26**(12), pp. 1593–1607.

Oliveira, C. L. N., Morais, P. A., Moreira, A. A., and Andrade, J. S. (2014), 'Enhanced Flow in Small-World Networks', *Physical Review Letters*, **112**(14), p. 148701.

Onnela, J.-P., Saramäki, J., Kertész, J., and Kaski, K. (2005), 'Intensity and coherence of motifs in weighted complex networks', *Physical Review E*, **71**(6), p. 065103.

Pachitariu, M., Steinmetz, N. A., Kadir, S. N., Carandini, M., and Harris, K. (2016), 'Fast and accurate spike sorting of high-channel count probes with KiloSort', *Advances of Neural Information Processing Systems*, **30**, pp. 4455–4463.

Panas, D., Amin, H., Maccione, A., Muthmann, O., Rossum, M. van, Berdondini, L., and Hennig, M. H. (2015), 'Sloppiness in Spontaneously Active Neuronal Networks', *Journal of Neuroscience*, **35**(22).

Panzeri, S. and Schultz, S. R. (2001), 'A unified approach to the study of temporal, correlational, and rate coding.' *Neural computation*, **13**(6), pp. 1311–49.

Panzeri, S., Senatore, R., Montemurro, M. A., and Petersen, R. S. (2007), 'Correcting for the Sampling Bias Problem in Spike Train Information Measures', *Journal of Neurophysiology*, **98**(3), pp. 1064–1072.

Panzeri, S., Schultz, S. R., Treves, A., and Rolls, E. T. (1999), 'Correlations and the encoding of information in the nervous system', *Proc. R. Soc. Lond. B*, **266**, pp. 1001–1012.

Panzeri, S. and Treves, A. (1996), 'Analytical estimates of limited sampling biases in different information measures.' *Network*, **7**(1), pp. 87–107.

Pedregosa, F., Michel, V., Grisel, O., Blondel, M., Prettenhofer, P., Weiss, R., Vanderplas, J., Cournapeau, D., Varoquaux, G., Gramfort, A., Thirion, B., Grisel, O., Dubourg, V., Passos, A., Brucher, M., Perrot, M., and Duchesnay, É. (2011), *Scikit-learn: Machine Learning in Python*, tech. rep., pp. 2825–2830.

Pennec, X., Fillard, P., and Ayache, N. (2006), 'A Riemannian Framework for Tensor Computing', *International Journal of Computer Vision*, **66**(1), pp. 41–66.

Penttonen, M. and Buzsáki, G. (2003), 'Natural logarithmic relationship between brain oscillators', *Thalamus and Related Systems*, **2**(02), p. 145.

Peyrache, A., Battaglia, F. P., and Destexhe, A. (2011), 'Inhibition recruitment in prefrontal cortex during sleep spindles and gating of hippocampal inputs.' *Proceedings of the National Academy of Sciences of the United States of America*, **108**(41), pp. 17207–12.

Pillow, J. W., Shlens, J., Paninski, L., Sher, A., Litke, A. M., Chichilnisky, E. J., and Simoncelli, E. P. (2008), 'Spatio-temporal correlations and visual signalling in a complete neuronal population', *Nature*, **454**(7207), pp. 995–999.

Pilz, G.-A., Carta, S., Stäuble, A., Ayaz, A., Jessberger, S., and Helmchen, F. (2016), 'Functional Imaging of Dentate Granule Cells in the Adult Mouse Hippocampus.' *The Journal of neuroscience*, **36**(28), pp. 7407–14.

Ponsoda, V., Martínez, K., Pineda-Pardo, J. A., Abad, F. J., Olea, J., Román, F. J., Barbey, A. K., and Colom, R. (2017), 'Structural brain connectivity and cognitive ability differences: A multivariate distance matrix regression analysis', *Human Brain Mapping*, **38**(2), pp. 803–816.

Pouget, A., Beck, J. M., Ma, W. J., and Latham, P. E. (2013), 'Probabilistic brains: knowns and unknowns', *Nature Neuroscience*, **16**(9), pp. 1170–1178.

Pritchard, W. S., Laurienti, P. J., Burdette, J. H., and Hayasaka, S. (2014), 'Functional Brain Networks Formed Using Cross-Sample Entropy Are Scale Free', *Brain Connectivity*, **4**(6), pp. 454–464.

Quian Quiroga, R. and Panzeri, S. (2009), 'Extracting information from neuronal populations: information theory and decoding approaches', *Nature Reviews Neuroscience*, **10**(3), pp. 173–185.

Quiroga, R. Q., Reddy, L., Kreiman, G., Koch, C., and Fried, I. (2005), 'Invariant visual representation by single neurons in the human brain', *Nature*, **435**(7045), pp. 1102–1107.

Ramadan, W., Eschenko, O., and Sara, S. J. (2009), 'Hippocampal sharp wave/ripples during sleep for consolidation of associative memory.' *PloS one*, **4**(8), e6697.

Ramón y Cajal (1888), 'Estructura de los centros nerviosos de las aves', *Rev. Trim. Histol. Norm. Pat.*, (10), pp. 1–10.

Ranck, J. B. (1973), 'Studies on Single Neurons in Dorsal Hippocampal Formation and Septum in Unrestrained Rats Part I. Behavioral Correlates and Firing Repertoires'.

Raposo, D., Kaufman, M. T., and Churchland, A. K. (2014), 'A category-free neural population supports evolving demands during decision-making', *Nature Neuroscience*, **17**(12), pp. 1784–1792.

Reijmers, L. G., Perkins, B. L., Matsuo, N., and Mayford, M. (2007), 'Localization of a stable neural correlate of associative memory.' *Science*, **317**(5842), pp. 1230–3.

Renart, A., Rocha, J. de la, Bartho, P., Hollender, L., Parga, N., Reyes, A., and Harris, K. D. (2010), 'The asynchronous state in cortical circuits.' *Science*, **327**(5965), pp. 587–90.

Ribot, T. (1882), *Diseases of Memory*, Washington, DC: Univ. Publ. Am.

Rich, P. D., Liaw, H.-P., and Lee, A. K. (2014), 'Place cells. Large environments reveal the statistical structure governing hippocampal representations.' *Science (New York, N.Y.)*, **345**(6198), pp. 814–7.

Richards, B. A. and Frankland, P. W. (2017), 'The Persistence and Transience of Memory.' *Neuron*, **94**(6), pp. 1071–1084.

Richards, B. A., Xia, F., Santoro, A., Husse, J., Woodin, M. A., Josselyn, S. A., and Frankland, P. W. (2014), 'Patterns across multiple memories are identified over time.' *Nature neuroscience*, **17**(7), pp. 981–6.

Rigotti, M., Barak, O., Warden, M. R., Wang, X.-J., Daw, N. D., Miller, E. K., and Fusi, S. (2013), 'The importance of mixed selectivity in complex cognitive tasks', *Nature*, **497**(7451), pp. 585–590.

Rolls, E. T. and Tovee, M. J. (1995), 'Sparseness of the neuronal representation of stimuli in the primate temporal visual cortex.' *Journal of neurophysiology*, **73**(2), pp. 713–26.

Rolls, E. T. and Treves, A. (1990), 'The relative advantages of sparse versus distributed encoding for associative neuronal networks in the brain', *Network*, **1**, pp. 407–421.

Rossum, M. C. van (2001), 'A novel spike distance.' *Neural computation*, **13**(4), pp. 751–63.

Roweis, S. T. and Saul, L. K. (2000), 'Nonlinear dimensionality reduction by locally linear embedding.' *Science*, **290**(5500), pp. 2323–6.

Roy, B. (1959), 'Transitivité et connexité', *Comptes rendus de l'Académie des Sciences*, **249**, pp. 216–218.

Rubin, A., Geva, N., Sheintuch, L., and Ziv, Y. (2015), 'Hippocampal ensemble dynamics timestamp events in long-term memory', *eLife*, **4**.

Rubin, A., Sheintuch, L., Brande-Eilat, N., Pinchasof, O., Rechavi, Y., Geva, N., and Ziv, Y. (2019), 'Revealing neural correlates of behavior without behavioral measurements', *Nature Communications*, **10**(1), p. 4745.

Rule, M. E., Loback, A. R., Raman, D. V., Driscoll, L. N., Harvey, C. D., and O'Leary, T. (2020), 'Stable task information from an unstable neural population', *eLife*, **9**.

Sadovsky, A. J. and MacLean, J. N. (2013), 'Scaling of topologically similar functional modules defines mouse primary auditory and somatosensory microcircuitry.' *Journal of neuroscience*, **33**(35), pp. 14048–60.

Salinas, E. and Sejnowski, T. J. (2001), 'Correlated neuronal activity and the flow of neural information', *Nature Reviews Neuroscience*, **2**(8), pp. 539–550.

Saramäki, J., Kivelä, M., Onnela, J.-P., Kaski, K., and Kertész, J. (2007), 'Generalizations of the clustering coefficient to weighted complex networks', *Physical Review E*, **75**(2), p. 027105.

Schacter, D. (2001), *The Seven Sins of Memory: How the Mind Forgets and Remembers*, Houghton Mifflin.

Schacter, D. L., Addis, D. R., and Buckner, R. L. (2007), 'Remembering the past to imagine the future: the prospective brain', *Nature Reviews Neuroscience*, **8**(9), pp. 657–661.

Schreiber, T. (2000), 'Measuring Information Transfer', *Physical Review Letters*, **85**(2), pp. 461–464.

Schröter, M., Paulsen, O., and Bullmore, E. T. (2017), 'Micro-connectomics: probing the organization of neuronal networks at the cellular scale', *Nature Reviews Neuroscience*, **18**(3), pp. 131–146.

Schultz, D. H. and Cole, M. W. (2016), 'Higher Intelligence Is Associated with Less Task-Related Brain Network Reconfiguration.' *The Journal of neuroscience : the official journal of the Society for Neuroscience*, **36**(33), pp. 8551–61.

Scoville, W. B. and Milner, B. (1957), 'Loss of recent memory after bilateral hippocampal lesions.' *Journal of neurology, neurosurgery, and psychiatry*, **20**(1), pp. 11–21.

Sekeres, M. J., Bonasia, K., St-Laurent, M., Pishdadian, S., Winocur, G., Grady, C., and Moscovitch, M. (2016), 'Recovering and preventing loss of detailed memory: differential rates of forgetting for detail types in episodic memory.' *Learning & memory*, **23**(2), pp. 72–82.

Shannon, C. and Weaver, W. (1949), *The Mathematical Theory of Communication*, University of Illinois.

Sherrington, C. S. (1892), 'Notes on the Arrangement of some Motor Fibres in the Lumbo-Sacral Plexus', *The Journal of Physiology*, **13**(6), pp. 621–772.

Singh, A. and Lesica, N. A. (2010), 'Incremental Mutual Information: A New Method for Characterizing the Strength and Dynamics of Connections in Neuronal Circuits', *PLoS Computational Biology*, **6**(12), ed. by P. E. Latham, e1001035.

Skaggs, W. E., Mcnaughton, B. L., Gothard, K. M., and Markus, E. J. (1993), 'An Information-Theoretic Approach to Deciphering the Hippocampal Code', *Advances in Neural Information Processing Systems*.

Slomianka, L., Amrein, I., Knuesel, I., Sørensen, J. C., and Wolfer, D. P. (2011), 'Hippocampal pyramidal cells: the reemergence of cortical lamination.' *Brain structure & function*, **216**(4), pp. 301–17.

Sohn, H., Narain, D., Meirhaeghe, N., and Jazayeri, M. (2019), 'Bayesian Computation through Cortical Latent Dynamics', *Neuron*, **103**(5), pp. 934–947.

Soltesz, I. and Losonczy, A. (2018), 'CA1 pyramidal cell diversity enabling parallel information processing in the hippocampus', *Nature Neuroscience*, **21**(4), pp. 484–493.

Somogyi, P. and Klausberger, T. (2005), 'Defined types of cortical interneurone structure space and spike timing in the hippocampus', *The Journal of Physiology*, **562**(1), pp. 9–26.

Souza, B. C., Pavão, R., Belchior, H., and Tort, A. B. (2018), 'On Information Metrics for Spatial Coding', *Neuroscience*, **375**, pp. 62–73.

Squire, L. R. and Alvarez, P. (1995), 'Retrograde amnesia and memory consolidation: a neurobiological perspective.' *Current opinion in neurobiology*, **5**(2), pp. 169–77.

Squire, L. R. and Zola-Morgan, S. (1991), 'The medial temporal lobe memory system.' *Science*, **253**(5026), pp. 1380–6.

Squire, L. R. (2004), 'Memory systems of the brain: A brief history and current perspective', *Neurobiology of Learning and Memory*, **82**, pp. 171–177.

Squire, L. R., Clark, R. E., and Knowlton, B. J. (2001), 'Retrograde amnesia', *Hippocampus*, **11**(1), pp. 50–55.

Stark, E., Roux, L., Eichler, R., and Buzsáki, G. (2015), 'Local generation of multineuronal spike sequences in the hippocampal CA1 region.' *Proceedings of the National Academy of Sciences of the United States of America*, **112**(33), pp. 10521–6.

Stark, E., Roux, L., Eichler, R., Senzai, Y., Royer, S., and Buzsáki, G. (2014), 'Pyramidal cell-interneuron interactions underlie hippocampal ripple oscillations.' *Neuron*, **83**(2), pp. 467–480.

Stevenson, I. H. and Kording, K. P. (2011), 'How advances in neural recording affect data analysis', *Nature Neuroscience*, **14**(2), pp. 139–142.

Stone, H. and Bosley, J. J. (1965), 'Olfactory discrimination and Weber's law', *Perceptual and motor skills*, **20**(2), pp. 657–65.

Strien, N. M. van, Cappaert, N. L. M., and Witter, M. P. (2009), 'The anatomy of memory: an interactive overview of the parahippocampal–hippocampal network', *Nature Reviews Neuroscience*, **10**(4), pp. 272–282.

Stringer, C., Pachitariu, M., Steinmetz, N., Carandini, M., and Harris, K. D. (2019), 'High-dimensional geometry of population responses in visual cortex', *Nature*, **571**(7765), pp. 361–365.

Strong, S. P., Koberle, R., Ruyter van Steveninck, R. R. de, and Bialek, W. (1998), 'Entropy and Information in Neural Spike Trains', *Physical Review Letters*, **80**(1), pp. 197–200.

Suszkiw, J. B. (2012), 'Synaptic Transmission', *Cell Physiology Source Book*, pp. 563–578.

Tanaka, K. Z., He, H., Tomar, A., Niisato, K., Huang, A. J. Y., and McHugh, T. J. (2018), 'The hippocampal engram maps experience but not place.' *Science (New York, N.Y.)*, **361**(6400), pp. 392–397.

Tanaka, K. Z., Pevzner, A., Hamidi, A. B., Nakazawa, Y., Graham, J., and Wiltgen, B. J. (2014), 'Cortical representations are reinstated by the hippocampus during memory retrieval.' *Neuron*, **84**(2), pp. 347–54.

Tao, S., Wang, Y., Peng, J., Zhao, Y., He, X., Yu, X., Liu, Q., Jin, S., and Xu, F. (2021), 'Whole-Brain Mapping the Direct Inputs of Dorsal and Ventral CA1 Projection Neurons', *Frontiers in Neural Circuits*, **15**, p. 20.

Tayler, K. K., Tanaka, K. Z., Reijmers, L. G., and Wiltgen, B. J. (2013), 'Reactivation of neural ensembles during the retrieval of recent and remote memory.' *Current biology : CB*, **23**(2), pp. 99–106.

Telesford, Q. K., Joyce, K. E., Hayasaka, S., Burdette, J. H., and Laurienti, P. J. (2011), 'The Ubiquity of Small-World Networks', *Brain Connectivity*, **1**(5), pp. 367–375.

Tenenbaum, J. B., Silva, V. de, and Langford, J. C. (2000), 'A global geometric framework for nonlinear dimensionality reduction.' *Science*, **290**(5500), pp. 2319–23.

Thivierge, J.-P. (2014), 'Scale-free and economical features of functional connectivity in neuronal networks.' *Physical review. E, Statistical, nonlinear, and soft matter physics*, **90**(2), p. 022721.

Tonegawa, S., Liu, X., Ramirez, S., and Redondo, R. (2015), 'Memory Engram Cells Have Come of Age', *Neuron*, **87**(5), pp. 918–931.

Treves, A. and Rolls, E. T. (1994), 'Computational Analysis of the Role of the Hippocampus in Memory', *Hippocampus*, **4**(3), pp. 374–391.

Trouche, S., Koren, V., Doig, N. M., Ellender, T. J., El-Gaby, M., Lopes-Dos-Santos, V., Reeve, H. M., Perestenko, P. V., Garas, F. N., Magill, P. J., Sharott, A., and Dupret, D. (2019), 'A Hippocampus-Accumbens Tripartite Neuronal Motif Guides Appetitive Memory in Space.' *Cell*, **176**(6), pp. 1393–1406.

Trouche, S., Perestenko, P. V., Ven, G. M. van de, Bratley, C. T., McNamara, C. G., Campo-Urriza, N., Black, S. L., Reijmers, L. G., and Dupret, D. (2016), 'Recoding a cocaine-place memory engram to a neutral engram in the hippocampus', *Nature Neuroscience*, **19**(4), pp. 564–567.

Tse, D., Langston, R. F., Kakeyama, M., Bethus, I., Spooner, P. A., Wood, E. R., Witter, M. P., and Morris, R. G. M. (2007), 'Schemas and memory consolidation.' *Science (New York, N.Y.)*, **316**(5821), pp. 76–82.

Valente, M., Pica, G., Bondanelli, G., Moroni, M., Runyan, C. A., Morcos, A. S., Harvey, C. D., and Panzeri, S. (2021), 'Correlations enhance the behavioral readout of neural population activity in association cortex', *Nature Neuroscience*, **24**(7), pp. 975–986.

Valero, M., Cid, E., Averkin, R. G., Aguilar, J., Sanchez-Aguilera, A., Viney, T. J., Gomez-Dominguez, D., Bellistri, E., and Prida, L. M. de la (2015), 'Determinants of different deep and superficial CA1 pyramidal cell dynamics during sharp-wave ripples', *Nature Neuroscience*, **18**(9), pp. 1281–1290.

Van Der Maaten, L. and Hinton, G. (2008), 'Visualizing Data using t-SNE', *Journal of Machine Learning Research*, **9**, pp. 2579–2605.

Ven, G. M. van de, Trouche, S., McNamara, C. G., Allen, K., and Dupret, D. (2016), 'Hippocampal Offline Reactivation Consolidates Recently Formed Cell Assembly Patterns during Sharp Wave-Ripples', *Neuron*, **92**(5), pp. 968–974.

Venkatesh, M., Jaja, J., and Pessoa, L. (2020), 'Comparing functional connectivity matrices: A geometry-aware approach applied to participant identification', *NeuroImage*, **207**, p. 116398.

Victor, J. D. and Purpura, K. P. (1996), 'Nature and precision of temporal coding in visual cortex: a metric-space analysis.' *Journal of neurophysiology*, **76**(2), pp. 1310–26.

Vyas, S., Golub, M. D., Sussillo, D., and Shenoy, K. V. (2020), 'Computation Through Neural Population Dynamics', *Annual Review of Neuroscience*, **43**(1), pp. 249–275.

Wang, S. S.-H., Shultz, J. R., Burish, M. J., Harrison, K. H., Hof, P. R., Towns, L. C., Wagers, M. W., and Wyatt, K. D. (2008), 'Functional Trade-Offs in White Matter Axonal Scaling', *Journal of Neuroscience*, **28**(15).

Warland, D. K., Reinagel, P., and Meister, M. (1997), 'Decoding visual information from a population of retinal ganglion cells.' *Journal of neurophysiology*, **78**(5), pp. 2336–50.

Warshall, S. (1962), 'A theorem on Boolean matrices', *Journal of the ACM*, **9**, pp. 11–12.

Watson, B. O., Levenstein, D., Greene, J. P., Gelinas, J. N., and Buzsáki, G. (2016), 'Network Homeostasis and State Dynamics of Neocortical Sleep.' *Neuron*, **90**(4), pp. 839–52.

Watts, D. J. and Strogatz, S. H. (1998), 'Collective dynamics of 'small-world' networks', *Nature*, **393**(6684), pp. 440–442.

Wills, T. J., Lever, C., Cacucci, F., Burgess, N., and O'Keefe, J. (2005), 'Attractor dynamics in the hippocampal representation of the local environment.' *Science*, **308**(5723), pp. 873–6.

Wilson, M. A. and McNaughton, B. L. (1993), 'Dynamics of the hippocampal ensemble code for space', *Science*, **261**(5124), pp. 1055–1058.

– (1994), 'Reactivation of hippocampal ensemble memories during sleep.' *Science*, **265**(5172), pp. 676–9.

Winocur, G. and Moscovitch, M. (2011), 'Memory transformation and systems consolidation.' *Journal of the International Neuropsychological Society : JINS*, **17**(5), pp. 766–80.

Yuste, R. (2015), 'From the neuron doctrine to neural networks', *Nature Reviews Neuroscience*, **16**(8), pp. 487–497.

Zandvakili, A. and Kohn, A. (2015), 'Coordinated Neuronal Activity Enhances Corticocortical Communication', *Neuron*, **87**(4), pp. 827–839.

Zanin, M., Sousa, P., Papo, D., Bajo, R., García-Prieto, J., Pozo, F. d., Menasalvas, E., and Boccaletti, S. (2012), 'Optimizing Functional Network Representation of Multivariate Time Series', *Scientific Reports*, **2**(1), p. 630.

Zhang, S., Schönfeld, F., Wiskott, L., and Manahan-Vaughan, D. (2014), 'Spatial representations of place cells in darkness are supported by path integration and border information.' *Frontiers in behavioral neuroscience*, **8**, p. 222.

Zippo, A. G., Storchi, R., Nencini, S., Caramenti, G. C., Valente, M., and Biella, G. E. M. (2013), 'Neuronal Functional Connection Graphs among Multiple Areas

of the Rat Somatosensory System during Spontaneous and Evoked Activities', *PLoS Computational Biology*, **9**(6), ed. by O. Sporns, e1003104.

Ziv, Y., Burns, L. D., Cocker, E. D., Hamel, E. O., Ghosh, K. K., Kitch, L. J., Gamal, A. E., and Schnitzer, M. J. (2013), 'Long-term dynamics of CA1 hippocampal place codes', *Nature Neuroscience*, **16**(3), pp. 264–266.

Zylberberg, J., Pouget, A., Latham, P. E., and Shea-Brown, E. (2017), 'Robust information propagation through noisy neural circuits', *PLOS Computational Biology*, **13**(4), ed. by N. Brunel, e1005497.